Universidad
Carlos III de Madrid
www.uc3m.es

TESIS DOCTORAL

Application of novel technologies for the development of next generation MR compatible PET inserts

Autor:

Georgios Konstantinou

Director:

Juan José Vaquero López

DEPARTAMENTO

Departamento de Bioingeniería e Ingeniería Aeroespacial, Universidad Carlos III de Madrid y Hospital General Universitario Gregorio Marañon

Leganés, 22 de Junio 2017

(a entregar en la Oficina de Posgrado, una vez nombrado el Tribunal evaluador , para preparar el documento para la defensa de la tesis)

TESIS DOCTORAL

Application of novel technologies for the development of next generation MR compatible PET inserts

Autor: *Georgios Konstantinou*

Director: Juan José Vaquero López

Firma del Tribunal Calificador:

		Firma
Presidente:	Andrés Santos	
Vocal:	Giancarlo Sportelli	
Secretario:	Luis Hernández Corporales	

Calificación:

Leganés 22 de Junio 2017

Abstract

Multimodal imaging integrating Positron Emission Tomography and Magnetic Resonance Imaging (PET/MRI) has professed advantages as compared to other available combinations, allowing both functional and structural information to be acquired with very high precision and repeatability. However, it has yet to be adopted as the standard for experimental and clinical applications, due to a variety of reasons mainly related to system cost and flexibility. A hopeful existing approach of silicon photodetector-based MR compatible PET inserts comprised by very thin PET devices that can be inserted in the MRI bore, has been pioneered, without disrupting the market as expected. Technological solutions that exist and can make this type of inserts lighter, cost-effective and more adaptable to the application need to be researched further.

In this context, we expand the study of sub-surface laser engraving (SSLE) for scintillators used for PET. Through acquiring, measuring and calibrating the use of a SSLE setting we study the effect of different engraving configurations on detection characteristics of the scintillation light by the photosensors. We demonstrate that apart from cost-effectiveness and ease of application, SSLE treated scintillators have similar spatial resolution and superior sensitivity and packing fraction as compared to standard pixelated arrays, allowing for shorter crystals to be used. Flexibility of design is benchmarked and adoption of honeycomb architecture due to geometrical advantages is proposed. Furthermore, a variety of depth-of-interaction (DoI) designs are engraved and studied, greatly enhancing applicability in small field-of-view tomographs, such as the intended inserts. To adapt to this need, a novel approach for multi-layer DoI characterization has been developed and is demonstrated.

Apart from crystal treatment, considerations on signal transmission and processing are addressed. A double time-over-threshold (ToT) method is proposed, using the statistics of noise in order to enhance precision. This method is tested and linearity results demonstrate applicability for multiplexed readout designs. A study on analog optical wireless communication (aOWC) techniques is also performed and proof of concept results presented. Finally, a ToT readout firmware architecture, intended for low-cost FPGAs, has been developed and is described.

By addressing the potential development, applicability and merits of a range of transdisciplinary solutions, we demonstrate that with these techniques it is possible to construct lighter, smaller, lower consumption, cost-effective MRI compatible PET inserts. Those designs can make PET/MRI multimodality the dominant clinical and experimental imaging approach, enhancing researcher and physician insight to the mysteries of life.

Resumen

La combinación multimodal de Tomografía por Emisión de Positrones con la Imagen de Resonancia Magnética (PET/MRI, de sus siglas en inglés) tiene clara ventajas en comparación con otras técnicas multimodales actualmente disponibles, dada su capacidad para registrar información funcional e información estructural con mucha precisión y repetibilidad. Sin embargo, esta técnica no acaba de penetrar en la práctica clínica debido en gran parte a alto coste. Las investigaciones que persiguen mejorar el desarrollo de insertos de PET basados en fotodetectores de silicio y compatibles con MRI, aunque han sido intensas y han generado soluciones ingeniosas, todavía no han conseguido encontrar las soluciones que necesita la industria. Sin embargo, existen opciones todavía sin explorar que podrían ayudar a evolucionar este tipo de insertos consiguiendo dispositivos más ligeros, baratos y con mejores prestaciones.

Esta tesis profundiza en el estudio de grabación sub-superficie con láser (SSLE) para el diseño de los cristales centelladores usados en los sistemas PET. Para ello hemos caracterizado, medido y calibrado un procedimiento SSLE, y a continuación hemos estudiado el efecto que tienen sobre las especificaciones del detector las diferentes configuraciones del grabado. Demostramos que además de la rentabilidad y facilidad de uso de esta técnica, los centelladores SSLE tienen resolución espacial equivalente y sensibilidad y fracción de empaquetamiento superiores a las matrices de centelleo convencionales, lo que posibilita utilizar cristales más cortos para conseguir la misma sensibilidad. Estos diseños también permiten medir la profundidad de la interacción (DoI), lo que facilita el uso de estos diseños en tomógrafos de radio pequeño, como pueden ser los sistemas preclínicos, los dedicados (cabeza o mama) o los insertos para MRI.

Además de trabajar en el tratamiento de cristal de centelleo, hemos considerado nuevas aproximaciones al procesamiento y transmisión de la señal. Proponemos un método innovador de doble medida de tiempo sobre el umbral (ToT) que integra una evaluación de la estadística del ruido con el propósito de mejorar la precisión. El método se ha validado y los resultados demuestran su viabilidad de uso incluso en conjuntos de señales multiplexadas. Un estudio de las técnicas de comunicación óptica analógica e inalámbrica (aOWC) ha permitido el desarrollo de una nueva propuesta para comunicar las señales del detector PET insertado en el *gantry* a un el procesador de señal externo, técnica que se ha validado en un demostrador. Finalmente, se ha propuesto y demostrado una nueva arquitectura de análisis de señal ToT implementada en *firmware* en FPGAs de bajo coste.

La concepción y desarrollo de estas ideas, así como la evaluación de los méritos de las diferentes soluciones propuestas, demuestran que con estas técnicas es posible construir insertos de PET compatibles con sistemas MRI, que serán más ligeros y compactos, con un reducido consumo y menor coste. De esta forma se contribuye a que la técnica multimodal PET/MRI pueda penetrar en la clínica, mejorando la comprensión que médicos e investigadores puedan alcanzar en su estudio de los misterios de la vida.

Περίληψη

Η πολυτροπική απεικόνιση, ως συνδιασμός τομογραφίας ποσιτρονικής εκπομπής και απεικόνισης μαγνητικού συντονισμού (PET/MRI, από τα αρχικά στα αγγλικά) έχει διαπιστωμένα πλεονεκτίματα σε σύγκριση με άλλες τεχνικές, καθώς επιτρέπει την ταυτόχρονη λήψη λειτουργικών και δομικών χαρακτηριστικών, με μέγιστη επαναληψιμότητα και ακρίβεια. Παρ’ όλα αυτά, η τεχνική δεν έχει αποκτήσει ακόμα την αναμενόμενη χρηστικότητα, για διάφορους λόγους που συχνά (ή κυρίως) σχετίζονται με το υψηλό κόστος και την περιορισμένη λειτουργικότητα Μια ελπιδοφόρα προσέγγιση βασίζεται σε πολύ λεπτούς ποζιτρονικούς τομογράφους, που παρεντίθενται εντός του θαλάμου ενός προϋπάρχοντος μαγνητικού τομογράφου και βασίζονται σε φωτοανιχνευτές πυριτίου. Ούτε αυτή η προσέγγιση έχει καταφέρει να γίνει η κεντρική τάση, όμως προς την κατεύθυνση αυτή υπάρχουν και χρήζουν περεταίρω διερεύνησης τεχνολογικές λύσεις, που θα μπορούσαν να δημιουργήσουν ελαφρύτερους, μικρότερους και φτηνότερους παρεντιθέμενους ανιχνευτές.

Σε αυτό το πλαίσιο διευρύνουμε την έρευνα για εφαρμογή της υπο-επιφανειακής χάραξης με λέισερ (SSLE) σε κρυστάλλους σπινθιρισμού. Έχοντας προμηθευτεί, μετρήσει και βαθμονομίσει ένα σύστημα SSLE μελετούμε το αποτέλεσμα διαφορετικών χαρακτηριστικών χάραξης στην ανίχνευση. Αποδείχνουμε ότι εκτός μειωμένου κόστους και ευελιξίας εφαρμογής, οι ανιχνευτές SSLE έχουν αντίστοιχη ανάλυση αλλά μεγαλύτερη ευαισθησία και κλάσμα πλήρωσης σε σχέση με τους συμβατικούς, επιτρέποντας την χρήση βραχύτερων κρυστάλλων. Η ευελιξία σχεδίασης επιδεικνύεται μέσω της χρήσης εξαγωνικών στοιχείων, που έχουν πλεονεκτημα ανάλυσης λόγω της ισοκατανομής. Επιπλέον, ποικίλα σχέδια ανίχνευσης βάθους αλληλεπίδρασης (DoI) χαράσονται και μελετώνται, ενισχύοντας την εφαρμοσιμότητα σε παρεντιθεμενους τομογράφους μικρής διατομής. Για περεταίρω προσαρμογή σε αυτή τη χρήση, αναπτύχθηκε και παρουσιάζεται μια καινοφανής προσέγγιση για πολυεπίπεδικη ανίχνευση DoI.

Πέρα από την χάραξη των κρυστάλλων, επεξεργαζόμαστε και απευθυνόμαστε σε ζητήματα μετάδοσης και ανάλυσης σήματος. Προτείνουμε μια μέθοδο δύο επιπέδων χρόνου πάνω από κατώφλι (ToT) με διόρθωση βάσει στατιστικών στοιχείων θορύβου. Αποδείξαμε ότι η μέθοδος μπορεί να εφαρμοστεί σε σε πολυπλεγμένα συστήματα. Επιπλέον, παρουσιάζουμε την δυνατότητα χρήσης αναλογικής ασύρματης οπτικής μετάδοσης (aOWC) σε επίπεδο πρωτοτύπου. Τέλος, αναπτύξαμε και παρουσιάζουμε μια αρχιτεκτονική ToT για FPGE χαμηλού κόστους.

Αποσκοπόντας στην δυνατότητα ανάπτυξης, εφαρμογή και πλεονεκτήματα εύρους διαθεματικών λύσεων, αποδεικνύουμε ότι με αυτές τις τεχνικές είναι δυνατόν να κατασκευαστούν ελαφρύτεροι, μικρότεροι, οικονομικότεροι, χαμηλότερης κατανάλωσης και συμβατοί με MRI περεντιθέμενοι ποζιτρονικοί τομογράφοι. Τέτοιες διατάξεις μπορούν να αναδείξουν την πολυτροπική απεικόνιση PET/MRI ως κυρίαρχη κλινική και πειραματική προσέγγιση ενισχύοντας τη διορατικότητα ερευνητών και γιατρών στα μυστήρια της ζωής.

"The luxury to anticipate good weather is not one we can afford;
instead, we should learn to navigate the storm"
Greek saying

Acknowledgements

Writing a PhD thesis has been the most diversely challenging task I ever undertook. However, as long as this task has been possible to complete, I can't but honestly express my gratitude to the people that accompanied me in this journey, from those that provided the direct help and work collaboration, to those that were able to support me and relieve the corresponding feelings and anxiety.

First, I would like to thank my supervisor, Juan José Vaquero Lopez, for giving me the opportunity to join his team and mentoring me not only in how to build nuclear medicine detectors, but also in fighting for my ideas and believing in myself; furthermore, for the great experience of living in the wonderful city of Madrid, the best city in the world.

Along with him, I would like to thank the group of the laboratorio de imagen médica (LIM), from the Hospital General Universitario Gregorio Marañón. I hope that they, under the strain and transformation the current economic and social situation has added, will manage to continue creating great science and develop great scientists. Particularly the people that were there when I joined, I would like to thank for helping me land in their city in such a graceful manner. I would also like to thank the people of the Departamento de Bioingeniería e Ingeniería Aeroespacial of Universidad Carlos III de Madrid, especially Miguel, Guillermo, Angélica, Carlos, Santi, Ana, Asier, Sara and Tom, for their support and endless energy, so necessary when mine was running out (quite often). Along with them, the whole group of Friday beers at el Puerto, for giving me the much cherished insight in Spanish cuisine and culture.

Of course, I also would like to voice my appreciation to the international colleagues from the INFIERI collaboration who, apart from securing the funding that I used for the PhD, shared the experience of the numerous workshops, visits and secondments; in particular, the groups of Pisa, both in INFN (Giancarlo, Fabrizio) and SSSA (Ernesto, Giulio) that supported the secondments undertaken. Moreover, our coordinator Aurore, for the impossible job of organizing such a diverse and broad collection of individuals; and more than everything the other ESRs, especially Stamatis, Eleytheria, Wajahat, Michele and Mateo, for making me feel that I am not alone in this madness.

On a personal level, I would like to thank my great and greatly supportive family, my parents Dionisis and Filia and my sister Thalia. In a broader scope aunts and uncles Kaiti, Tonia, Gerasimos, Nitsa and cousins Mitsos, Maria and Katerina who have been on my side all this time. Most importantly, my companion in life Masha Reva, who taught me how it is really worth trying and becoming better every single day and has been there to share the biggest and strongest happiness and most difficult melancholies.

Furthermore, all the people who were there when I needed some solace from the toils of life. From Madrid Hara and Stathis, Tania, Laura and Giannis and from around the world Foivos, Vaggelis, Vasilis, Panos and Elena, Nikos, Lefteris and Eliza, Matias and Naz, Valerio, Samir, Maya, Spyros, Thanos and Eirini, Fotis, Manolis, Ilias... countless kilometers will keep separating us from each other, but the feelings are strong and true and when we meet, it is as if we never stopped living in the unchangeable refuge of our common past.

Finally, I would like to thank all the innumerable great people that I have had the luck to meet, discuss, learn from and look up to; the only reason that allows me to not relinquish the hope that one day, this world will be a better place. This thesis is the contribution I was able to make for that goal, during the last three years.

Table of contents

Chapter 1: Introduction and Hypothesis

Chapter 2: PET basics

Chapter 3: A feasibility study of Sub-Surface Laser Engraving for scintillators

Chapter 4: Verification of Sub-Surface Laser Engraving for scintillators

Chapter 5: Non-square designs and depth of interaction by Sub-Surface Laser Engraving for scintillators

Chapter 6: A time-over-threshold technique for multiplexed read-out for MR compatible PET inserts

Chapter 7: Demonstration of optical wireless applicability for a PET/SPECT insert front-end

Chapter 1: Introduction and Hypothesis

A. *Medical imaging*

The motivation of the present thesis is to advance the use of medical imaging, which is an indispensable tool for medical research and application, through instrumentation development of nuclear medicine detectors. The basic concepts and motivation for the research direction followed will be described in the next paragraphs.

Medicine is the science and practice of the diagnosis, treatment, and prevention of disease [1]. As such, it can't be conceived without the aspect of inspection of the patient and understanding of the physiology and anatomy of the organism, elements already noted by the first physicians [2]. In many cases, direct in-vivo access to functional systems of the organism is not possible. Thus, taking advantage of the crest of available techno-economic and ethical development of civilization, methods, techniques and appliances that can be applied to produce a perceivable representation of the structure or functionality of part or the total of human body are being developed.

Figure 1.1 First medical X-ray by Wilhelm Röntgen of his wife Anna Bertha Ludwig's hand

In the circumstance of availability of visual reconstruction in modern times, such representations are termed under the umbrella of the general expression "medical imaging". Serving for clinical diagnosis, monitoring of disease, drug development, functional evaluation, among other, medical imaging expresses a significant part of the revolution the application of technological advances has brought to medicine [3]. Different imagers, taking advantage of different physical and biological processes and properties, have been developed and specialized into different aspects of the medical notion. From the first bidimensional approaches (figure 1.1) to modern tetradimensional imaging [4], technology and concept evolution provide novel possibilities and revolutionary techniques that optimize the medical process and fulfill the Hippocratic command: "Διαιτήμασί τε χϱήσομαι ἐπ᾽ ὠφελείῃ καμνόντων κατὰ δύναμιν καὶ κϱίσιν ἐμήν", to use treatment to help the sick according to best ability and judgment [5].

B. Imaging approaches

It is not an easy task to classify the multitude of modern day imagers (figure 1.2). However, an occurring categorization is based on the tendency of each approach to better represent and demonstrate either structural or functional characteristics of the subject under study, even though non exclusively. More precisely, appliances such as x-ray computed tomography (CT) [6][7], magnetic resonance imaging (MRI) [8] and ultrasound imaging [9] are mainly used for anatomical representation of parts or the total body of the patient, while positron emission tomography (PET) [10] and single photon emission computed tomography (SPECT) [11] focus on the depiction of physiological functions. Optical imaging, including tomographic approaches, could belong to either, or both of these categories, depending on the detailed function and information retrieved [12]. Better representation constitutes of superb sensitivity, higher resolution and straightforward data processing. This doesn't prevent the cross-over application of an appliance, exemplified in the development of functional MRI [13] and its broad application especially for neurological studies [14], in the lack or unavailability of PET, even though it demonstrates several orders of magnitude lower sensitivity [15].

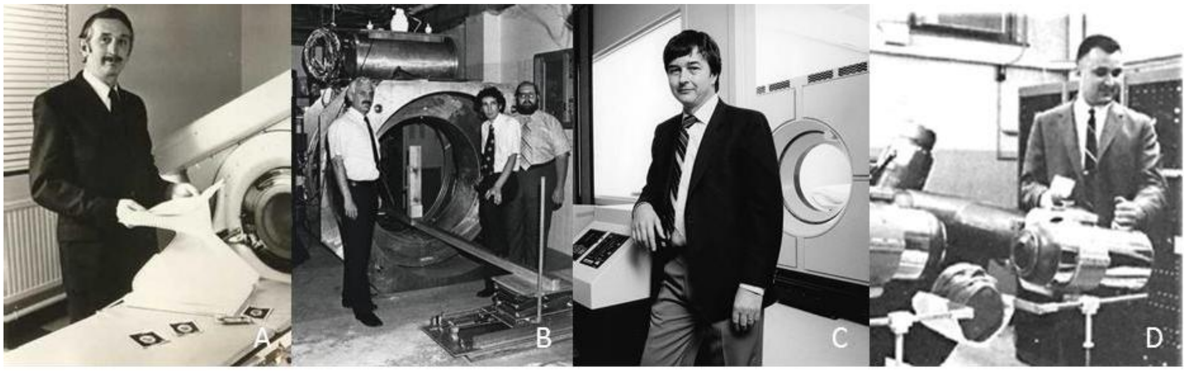

Figure 1. 2 The forefathers of tomographic imaging appliances: (A) G. Hounsfield with first CT (1972), (B) R. Damadian, L. Minkoff and M. Goldsmith with "Indomitable", the first MRI machine (1977), (C) M. Phelps with the UCLA PET (1978), (D) D. Kuhl with Mark II tomograph (1974 [16]

The main factor behind this differentiation occurs due to the nature of imaging for the different approaches. The aforementioned structural techniques roughly relate to a field, radiative, acoustic or magnetic, being shed on the subject and the shadow, reflection or reaction being recorded. The functional techniques mostly exploit an agent, carrying both a factor that is included in the biological process and a detectable tracer, along with the corresponding agent detection infrastructure.

As an example of the functionality of a structural technique, MRI will be used [17]. Using a strong magnetic field, the spin vectors of the particles of the tissue are parallelized. By the application of magnetic gradients, the distinct nuclear magnetic resonance of different element concentration produces distinguishable electromagnetic echoes, which is then captured by receptor coils and reconstructed. Thus a tridimensional anatomical map of the tissues is provided. Functional MRI is based on the same principle. If this physical reaction can be repeated fast enough, situational anatomy can be recorded, roughly corresponding to functional tracking of processes. Even if this approach is being broadly exploited, real functional tracking with higher resolution and sensitivity requires a different principle.

As a representative of functional imaging appliances, PET scanners use radiotracers, comprising of a biological molecule and a $\beta+$ decay isotope (for instance, ^{18}F) [18]. Each ensuing positron quickly meets an electron and both get annihilated, while a pair of γ rays with energy equivalent to the mass of the two particles is emitted from the annihilation point with almost opposite directions. Detectors are positioned around the subject under study, and commonly use scintillation, a property of certain materials that absorb these γ and transform their energy into visible light. This light is transformed into electric signal by photomultipliers and coincidence detection of γ scintillation events reconstructs the tridimensional distribution of positron emission and consequently also of the biological tracer.

C. Multimodal imaging

It can be thus deduced that optimal inspection capability of the clinical or experimental case, should include complementary imaging approaches. To decrease patient discomfort, examination time and processing, it should be made possible to combine and record simultaneously. Most favorable case, moreover, would be when such recording should refer and be applied to the most effective and least invasive approach of each category briefly described above (figure 1.3). This course of thought is also the course of action in modern medical technology, as the current development trend refers to what is called "multimodal imaging techniques". By such approach, the physiological process is depicted within the anatomical frame of the tissues included, providing sublime understanding of the clinical situation. In this context, therefore, multimodality can be considered a new revolution for imaging. Furthermore, the occurring technical and engineering questions and problems not only take advantage of, but also put forth the crest of scientific research.

The eventual combination of PET and MRI can be thus accepted as the optimal, currently, combination for multimodal imaging, as observed consequently in the direction the medical instrumentation community has adopted. PET, for more than fifteen years [19] has already been extensively used in pair with CT to the extent that referring to PET scanning irrevocably infers PET/CT. While this combination provides numerous advantages, the radiation dose of CT limits the number of repetitions possible, thus also the extent of application of such setting. MRI, on the other side, has been developed as a functional tool as well, being the standard especially in neurological studies [14], [15]. For the vast majority of most common, costly, or fatal diseases worldwide, one of the two or both modalities are the standard in use, either for research, diagnosis, prevention or cure monitoring. It is equally straightforward to estimate, thus, that combining them would create a disruptive approach on multimodality and by function on imaging and medical science itself, creating the most potent medical tool to date.

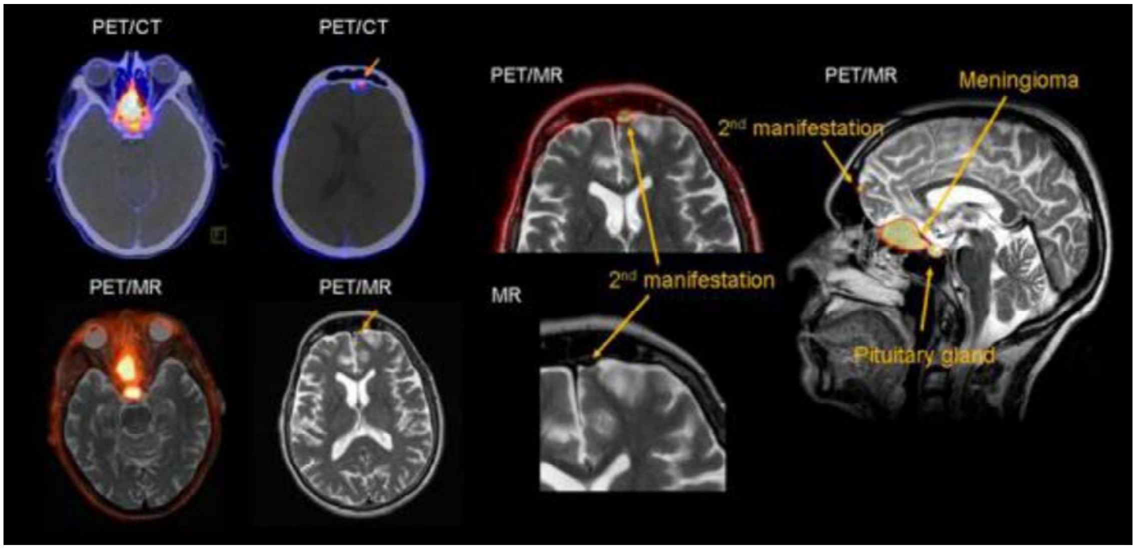

Figure 1.3 Demonstration of the imaging quality of multimodal PET/MR, as compared to PET/CT and only MRI [20].

D. *The chase for PET/MR*

Unfortunately, there are several factors that challenge the fusion of these two modalities. Main hindrance occurs due to the large, both in value and gradient, magnetic field that the MRI requires. This field greatly affects the standard detectors, photomultiplier tubes (PMT), used for PET (figure 1.4). Even though alternative devices, silicon photomultipliers (SiPM) [22], have been in use over the last years, the metallic interconnection and electronics required are prone to permanent or functional fault, once exposed to magnetic fields of such extend. On the other hand, the introduction of any object inside the MRI obscures the received image, in cases, to total disruption. Under these circumstances, the more straightforward issues concerning device volume, proximity to subject under study, electronic multiplexing and image corregistration, though also noteworthy, will not be further referred to.

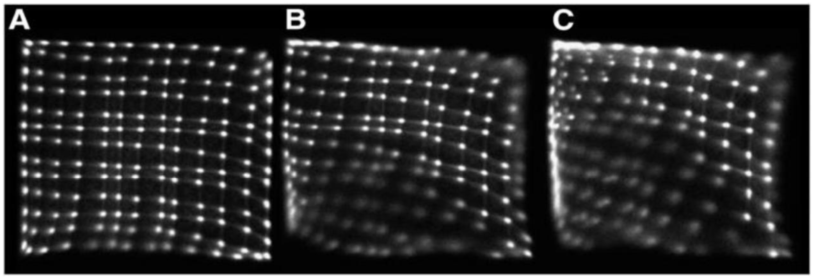

Figure 1.4 Effect of rising magnetic field on PMTs, from left to right [21]

Luckily, over the last years, several smart engineering solutions have been proposed, allowing for this deed to be materialized. Semi-simultaneous imaging and separation of the imagers (figure 1.5A) are the first approaches that regardless of the cost of function, size and difficult use, have seen action during the last decade. Other machines merge the imagers in one gantry (figure 1.5B, C) and through design twitches acquire images at a satisfactory rate and quality. A more innovative attitude concerns rethinking in total the design of PET detector, in order to create a thin shell that is then being inserted in the MRI bore (figure 1.5D, E).

Applicable mostly for experimental small animal MRI systems or as a dedicated brain PET appliance, this concept has been gaining momentum. With inserts receptor coils can be placed within the insert allowing for minimum interference to the MR reconstructed image. An insert can be adaptable to different MRI appliances, as it can be adjustable in size and shape, lowering greatly the cost of multimodal imaging, as a small fraction compared to procuring, developing and building a new PET/MR appliance.

While it demonstrates important advantages, this approach also has particular limitations that can be crippling to its broader adoption as a medical and experimental tool. The space inside the MRI bore is by definition limited and referenced as “claustrophobic” [23]. An insert that further limits it, could make examination so odious that it would either obscure the experimental result, for instance in the case of neurological studies, and be discarded in clinical practice. Apart from the size limitations, transmission of the PET information to a processing unit, currently through extensive cabling, copper or optical, creates a net of wires that make rapid intervention, in the case of emergency, impossible and protract preparation time, while occupying precious space around the MRI and altering the magnetic field.

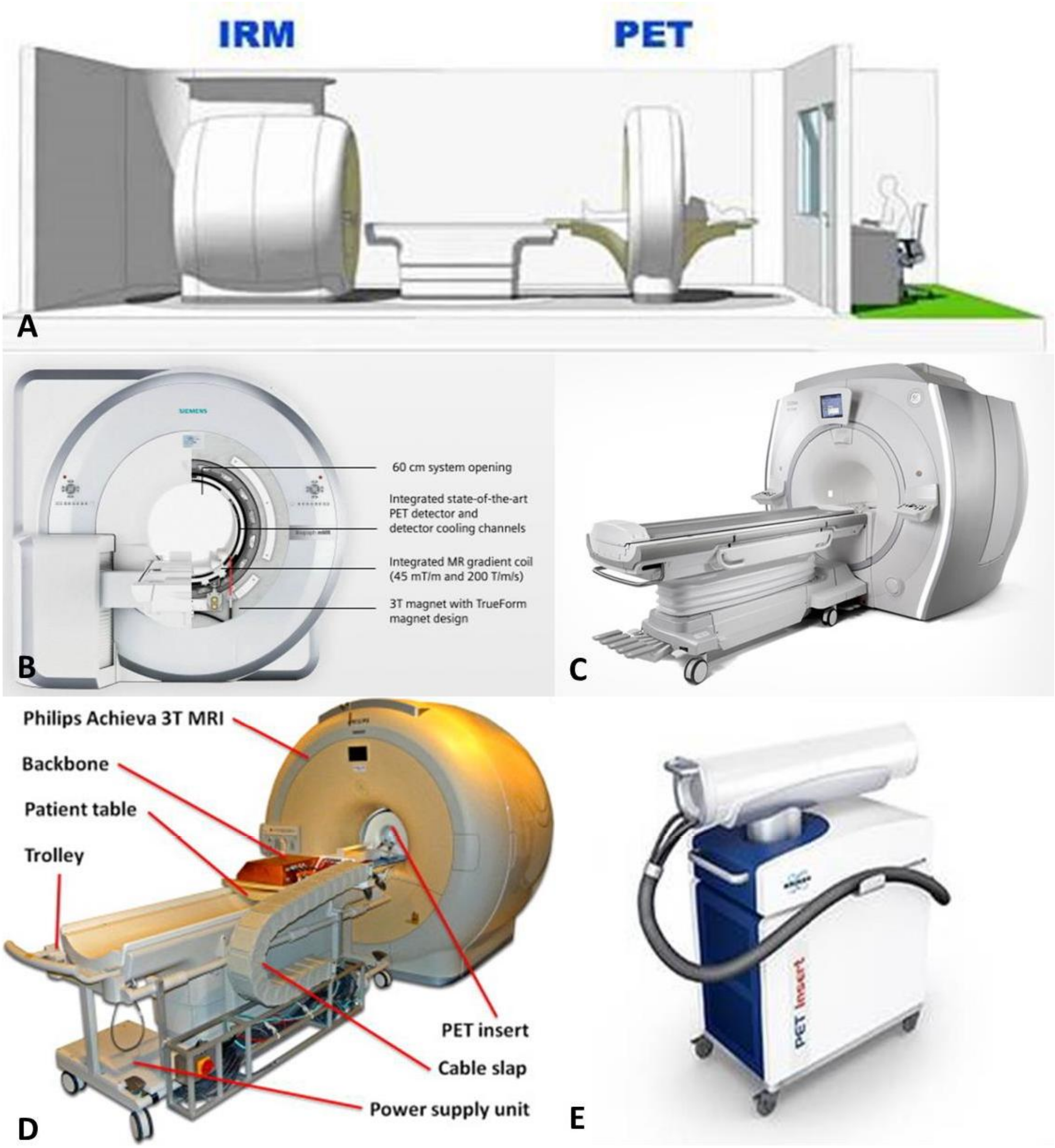

Figure 1.5 (A) Philips Ingenuity TF PET/MR, (B) Siemens Biograph mMR, (C) General Electric SIGNA PET/MR, (D) ExMI RWTH Aachen Hyperion PET insert, (E) Bruker PET insert

E. Objective: What could make PET/MR the standard multimodal approach?

Despite the engineering solutions under development and the profound superiority in resolution and contrast, compared to other multimodality combinations, PET/MR in any form has yet to reach a broader market (table 1.1).

Table 1.1 Survey form the 5th PET/MRI workshop (Tübingen-February 2016) on the reasons for the delay of clinical adoption of PET/MR

Rank	Barrier to clinical adoption
1	Capital cost including building work and installation
2	Lack of clinical trials demonstrating advantage over PET/CT
3	Lack of a compelling argument to acquire PET/MR
4	Operational costs including service contracts
5	Lack of suitably qualified, trained or experienced stuff
6	Current PET/MR hardware needs to be improved
7	Lack of suitable software to effectively analyze the PET/MR data
8	Lack of commitment or uncertainty about on-going vendor support

By scrutinizing the results of this survey, some insight on the direction that should be followed can be acquired. The cost of existing designs is perhaps the most important, appearing twice on the list. By developing cost effective solutions, the demonstrated merits and experimental repeatability of PET/MR will be convincing enough an argument for acquisition of such systems. A lightweight and easy-to-use device would allow experience to be gained rapidly, as it would require minimum training for physicians or MR technicians. Finally, hardware and software issues should be addressed. Thus, in order to break the barrier withholding the immense possibilities of widespread promotion of PET/MR, cost-effective, innovative on the hardware, data transmission and acquisition devices that would be easy to use should be designed and evaluated.

F. Hypothesis

In engineering, the concept of trade-off, or equilibrium, signifies the balance between the characteristics of system solutions. For instance, in electrical engineering, negative feedback is used in amplifiers to trade gain for other desirable properties, such as improved bandwidth or noise immunity. Successful engineering research is the one that breaks this equilibrium through innovative application of techniques, models and concepts. In this context, we believe that the technology necessary for next generation MR compatible PET inserts exists and only need to be further researched. Through study, simulation and demonstration of proof of concept designs we will redeem the vices and enquire into the virtues of existing designs, along the aforementioned lines. In order to create a higher balance of trade-off we will resort to the novel application on scintillator detectors, of techniques from other fields, such as laser manufacturing and visible light photonics and communication.

Available, yet undeveloped is the approach of applying sub-surface laser engraving (SSLE) to the scintillators used for PET [24]. Those crystals constitute the most voluminous part of the detector front-end and their characteristics are fundamental for the resolution and sensitivity of the appliance. We will demonstrate that it is possible to greatly profit from this application on all aspects, furthermore providing unprecedented flexibility on the design of the detector and including necessary traits, while reducing size and cost.

Another technique that could provide great advantages on the design of MR compatible PET insert is that of optical wireless communication (OWC) [25]. Studying the existing insert designs, it can be argued that a device without necessity of wires could provide the element necessary for physicians and MRI technicians to approach the PET/MR idea more favorably. If such a design is cost effective, miniaturized in size, flexible in form and easy to use, it could allow this technology to create a new market and value network and eventually disrupt the existing one, on multimodal medical imaging [26].

Along these lines, our study will also include data acquisition considerations, which could facilitate the integration of modular detectors with MR coils and is a solution which will allow case-specific MR compatible PET or SPECT topologies. Those future designs will be adaptable to the size of the MRI bore and the characteristics of desired acquisition, with applications in neuroscience, cardiology, oncology or other field, in clinical or experimental scenarios.

To sum up the hypothesis, I believe that better MRI compatible PET inserts can be conceived by implementing high sensitivity, high spatial resolution scintillation crystal matrices by means of SSLE techniques, and by introducing smart front-end processing and wireless communications technologies (OWC) that substantially reduce the electronic load of those inserts. These ideas are detailed in the following list of the specific objectives defined for this thesis (table 1.2).

Table 1.2 List of objectives in corresponding technologies and advantage added

Technique	Objective	Advantage
SSLE	Development of a precise and low cost engraving suite	Cost effectiveness
SSLE	Depth of interaction	Acquisition quality
SSLE	Non-conventional pixel shapes	Design flexibility
SSLE	Packing fraction, sensitivity	Miniaturization
Smart processing	Development of a precise time-over-threshold (ToT) approach	Miniaturization
Smart processing	Demonstration of compatibility between ToT and multiplexing schemes	Miniaturization
Smart processing	Development of FPGA based pre-processing algorithms	Cost effectiveness
OWC	Proof of concept of analog transmission	Design flexibility
OWC	Development of analog multiplexing techniques	Miniaturization

G. Thesis outline

The aforementioned objectives will be addressed throughout this thesis, by demonstrating the results and experience we acquired through our experimental settings and simulating techniques. The next chapter will be dedicated to providing the necessary knowledge of PET function, requirements, limitations and potential. An experienced reader need not bother with this chapter.

Next, our study on SSLE for scintillators will be presented in three chapters. The initial considerations, simulations and photometric experiments, necessary for deeper understanding of the process will be first exhibited. In the following chapter, experimental results will be demonstrated and quantification resulting from the comparison of SSLE designs with standard ones will be made. Next, the real potential of this technique, referring to the adoption of non-classical pixel architectures and depth-of-interaction designs will be investigated. Mathematization of this process along with novel methods for characterization of said designs will be presented.

The next concept will be introduced through demonstration of the considerations necessary for scaling up from a single detector to a whole machine. A chapter will be dedicated on adopting a novel data treatment approach on highly multiplexed designs.

Afterwards, the motivation for the application of OWC for PET will be exhibited and the dilemmas we faced when building the first experimental results debated. Results from the proof of concept design will be discussed and further considerations on how this approach can be better exploited will be shown.

The next chapter will concern data acquisition concepts, with the intention to demonstrate that a front-end design like the one intended can not only be conceptualized, but also read out in a scalable, cost effective manner, with the application of FPGAs.

The final chapter will conclude this work. In it, we will intend to demonstrate how, by the application of the techniques developed and described, the goals set on the hypothesis have been reached. The innovations and advantages of our approach will be numerated and we hope that the thesis of this text will be sufficiently supported.

REFERENCES

[1] Augarde, A. J. (1981). Medicine. The Oxford Dictionary. Oxford, Oxford University Press.
[2] Codellas, P. S. (1932). Alcmaeon of Croton: His life, work, and fragments. Proceedings of the Royal Society of Medicine, 25(7), 1041.
[3] Lomas, D. J., & Dixon, A. K. (1995). 100 years and running: the medical imaging revolution. The Lancet, 346, S20.

[4] Vedam, S. S., Keall, P. J., Kini, V. R., Mostafavi, H., Shukla, H. P., & Mohan, R. (2002). Acquiring a four-dimensional computed tomography dataset using an external respiratory signal. Physics in medicine and biology, 48(1), 45.

[5] Edelstein, L. (1943). The Hippocratic oath, text, translation and interpretation, Baltimore, the Johns Hopkins Press

[6] Vallebona, A. (1930). Una modalità di tecnica per la dissociazione radiografica delle ombre applicata allo studio del cranio. *Radiol Med*, *77*, 1090-7.

[7] Hounsfield G.N. (1973). Computerized transverse axial scanning (tomography). *Br. J. Radiol.* **46**:1016-1022

[8] Lauterbur, P. C. (1973). Image formation by induced local interactions: examples employing nuclear magnetic resonance.

[9] Cieszynski, T. (1960). Intracardiac method for the investigation of structure of the heart with the aid of ultrasonics. Archivum immunologiae et therapiae experimentalis, 8, 551.

[10] Alavi, A., Lakhani, P., Mavi, A., Kung, J. W., & Zhuang, H. (2004). PET: a revolution in medical imaging. Radiologic Clinics of North America, 42(6), 983-1001.

[11] Kuhl, D. E., & Edwards, R. Q. (1963). Image Separation Radioisotope Scanning 1. *Radiology*, *80*(4), 653-662.

[12] Arridge, S. R. (1999). Optical tomography in medical imaging. *Inverse problems*, *15*(2), R41.

[13] Kwong, K. K., Belliveau, J. W., Chesler, D. A., Goldberg, I. E., Weisskoff, R. M., Poncelet, B. P., ... & Turner, R. (1992). Dynamic magnetic resonance imaging of human brain activity during primary sensory stimulation. Proceedings of the National Academy of Sciences, 89(12), 5675-5679.

[14] Cabeza, R., & Nyberg, L. (2000). Imaging cognition II: An empirical review of 275 PET and fMRI studies. Journal of cognitive neuroscience, 12(1), 1-47.

[15] Disselhorst, J. A., Bezrukov, I., Kolb, A., Parl, C., & Pichler, B. J. (2014). Principles of PET/MR imaging. Journal of Nuclear Medicine, 55(Supplement 2), 2S-10S.

[16] http://www.edubilla.com/inventor/godfrey-hounsfield/
http://www.two-views.com/mri-imaging/history.html#sthash.k9opKMMJ.dpuf
http://www.ucla.edu/optimists/stories/ucla-health,
Silver S 1996 'Father of emission tomography' receives 1996 Cassen Prize [news] J. Nucl. Med. 37 23N–24N, retrieved 12.12.2016

[17] Hornak, J. P. (1996). The basics of MRI.

[18] Knoll, G. F. (2010). *Radiation detection and measurement*. John Wiley & Sons.

[19] Townsend, D. W. (2008, August). Combined positron emission tomography–computed tomography: the historical perspective. In Seminars in Ultrasound, CT and MRI (Vol. 29, No. 4, pp. 232-235).

[20] WB Saunders.Pichler, B. J., Judenhofer, M. S., & Pfannenberg, C. (2008). Multimodal Imaging Approaches: PET/CT and PET/MRI. In *Molecular Imaging I* (pp. 109-132). Springer Berlin Heidelberg.

[21] Vaquero, J. J., Sánchez, J. J., Udías, J. M., Cal-González, J., & Desco, M. (2013). MRI compatibility of position-sensitive photomultiplier depth-of-interaction PET detectors modules for in-line multimodality preclinical studies. *Nuclear Instruments and Methods in Physics Research Section A: Accelerators, Spectrometers, Detectors and Associated Equipment*, *702*, 83-87.

[22] McElroy, D. P., Saveliev, V., Reznik, A., & Rowlands, J. A. (2007). Evaluation of silicon photomultipliers: a promising new detector for MR compatible PET. *Nuclear Instruments and Methods in Physics Research Section A: Accelerators, Spectrometers, Detectors and Associated Equipment*, *571*(1), 106-109

[23] Eshed, I., Althoff, C. E., Hamm, B., & Hermann, K. G. A. (2007). Claustrophobia and premature termination of magnetic resonance imaging examinations. *Journal of Magnetic Resonance Imaging*, *26*(2), 401-404.

[24] Moriya, T., Fukumitsu, K., Sakai, T., Ohsuka, S., Okamoto, T., Takahashi, H., ... & Yamashita, T. (2010). Development of PET detectors using monolithic scintillation crystals processed with sub-surface laser engraving technique. *IEEE Transactions on Nuclear Science*, *57*(5), 2455-2459.

[25] Arnon, S., Barry, J., & Karagiannidis, G. (Eds.). (2012). *Advanced optical wireless communication systems*. Cambridge university press.

[26] Bower, J. L., & Christensen, C. M. (1995). *Disruptive technologies: catching the wave* (pp. 506-20). Harvard Business Review Video.

Chapter 2: PET basics

A. A Historical perspective

It is always a matter of debate when exactly should the beginning of a technological advance be placed [1]. In the case of PET, the scientific breakthroughs that made the technique available can be traced back to different fields such as physics, chemistry or medicine and different moments of the previous century [2].

In 1951 William Sweet presented the first preliminary idea of PET at the dedication of the Research Building of the Massachusetts General Hospital [3]. One year later, the very first prototype of a PET brain scanner [4] was built, applying two opposite NaI:Tl scintillator crystals coupled to two photomultipliers for detection and an ink plotter for imaging (figure 2.1). In the early ’70s James Robertson at Brookhaven, Chris Thompson and collaborators at Montreal Neurological Institute [5] as well as Ed Hoffman and Michael Phelps at UCLA, built the first tomographs, demonstrating the potential of PET in Neurological studies and in Functional brain imaging (fig. 4). The UCLA group furthermore created the literature basis on the quantitation of PET images [6].

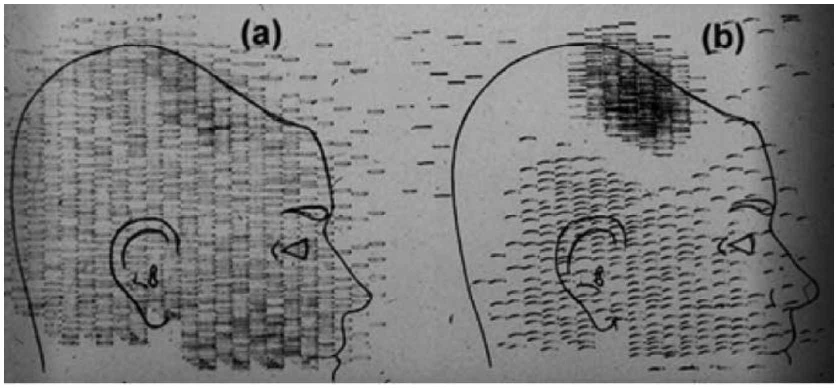

Figure 2. 1 Coincidence scans of patient with recurring brain tumor, obtained with the first PET scanner [4]

By now, the detection technique has been consolidated. Scintillators are used to capture γ-radiation and the ensuing light is transformed into electric signal by visible/near ultraviolet light photodetectors. With the theoretical backbone and technological standardization of this emerging imaging approach in place, developments in detection materials lead to improving performance allowing the pivot from bidimensional to tridimensional imaging and the expansion of field of view (FOV). Evolution of electronics, composition of novel scintillator crystals, such as bismouth germinate (BGO) and lutetium or lutetium-ytrium orthosilicate (LSO-LYSO) allowed enhanced detector resolution, sensitivity, cost-effectiveness and miniaturization.

Molecular imaging, the visual representation, characterization and quantification of biological processes that take place in a living being at the cellular and sub-cellular level [7] requires high sensitivity and spatial resolution. This goal takes advantage of PET especially through the development of multimodal designs. For instance, PET/CT [8], which facilitated greatly the diagnosis, staging and prognosis of cancer, is an indispensable tool in modern medicine. In this context, the rest of the chapter will be dedicated on the description of the building blocks that comprise PET, but will also focus on the applications in molecular imaging and outlook of the technique.

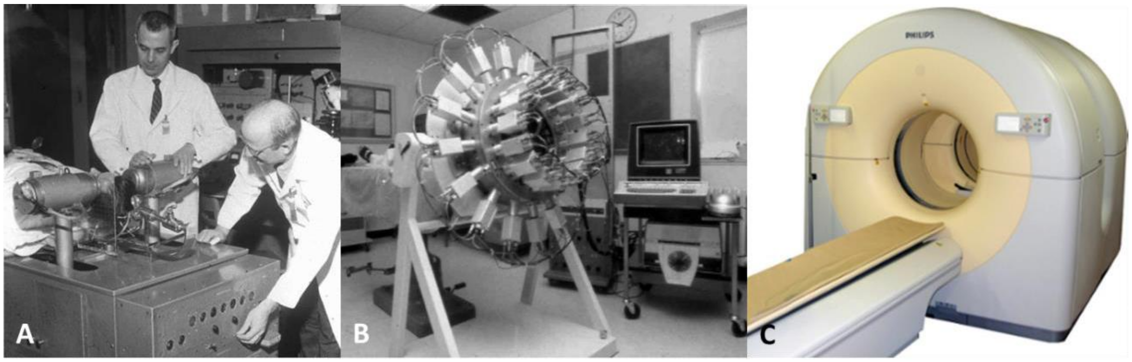

Figure 2. 2 A. Dr. G.L. Brownell (left) and Dr. Aronow with the first PET scanner (1950s), B. Positome (Montreal Neurological Institute- 1970s) [2] C. Philips GEMINI LX whole body PET/CT (2000s)

B. β+ Radiotracers: Physics and application

As mentioned in the previous chapter, radiotracers are the biological molecules which, while taking part in a physiological procedure, also carry isotopes that can be traced by imaging appliances. For PET, those isotopes are the ones that have less neutrons with respect to the number of protons and decay to a stable configuration through β+ decay. The discovery of the positron by C. D. Anderson (1936 Nobel Laureate in Physics “for his discovery of the positron”) along with the fundamental theory of radioactive β decay, forms the theoretical particle physics basis of the PET technique. Positrons are emitted having kinetic energy within a known range, which varies for different emitters [9]. They gradually lose this energy through Coulomb interactions with the biological tissue or bremsstrahlung [10], until reaching thermal equilibrium. The positron is the anti-particle of electron thus, upon reaching thermal equilibrium, it annihilates along with a random electron of the tissue, producing two gamma rays of exactly 511 KeV, due to energy conservation principles. This annihilation takes place within a certain range from the positron emission point, termed positron range [11], while the two rays are almost antiparallel due to momentum conservation of the electron-proton system, the small amount of noncollinearity being attributed to the small excess momentum that the positron still has.

The production of big quantities of such isotopes in a controlled and reproducible manner, allowing industrial application, is made through particle accelerators, mostly cyclotrons. The most used β+ emitters are "physiological radioisotopes" such as ^{11}C, ^{13}N, ^{15}O and ^{18}F [2]. Those nuclei have half-lives of several minutes to few hours, while being common in biological molecules. Through the groundbreaking research of György Hevesy (1943 Nobel prize in Chemistry), it was demonstrated that changing of an atom in a molecule with its radioisotope will not change its chemical and biological behavior significantly. In this context, changing one of the atoms of a biological molecule or an analogous by its β+ isotope allows the distribution of β+ emitters inside a living subject, tracing the metabolic function the original molecule would have.

Several different radiotracing molecules are used in PET [12]. To explain in more detail the production and application process, we will analyze the case study of the most common one, Fludeoxyglucose (figure 2.3, ^{18}F-FDG). This molecule was first described in 1968 [13]. Since its development in 1976 it was demonstrated that it is ideal for tracing neurological functions [14], facilitating neuroscience research, while in 1980 it was observed that ^{18}F-FDG also accumulates in tumors [15]. Based on ^{18}F that has almost 2 hour half-life, it can be transported from production point to examination facility for significantly more distance than other radiotracers, making its market broader.

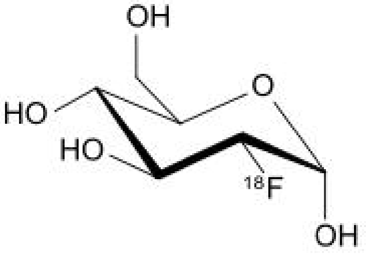

Figure 2. 3 ^{18}F-FDG

FDG is an analog of glucose. Lacking the 2-hydroxyl group (-OH), required for further glycolysis, it is trapped inside the cell. In this manner, once administered, it will not only be favorably received by high-glucose cells, such as the activated brain cells or cancer cells, but also remain there until decay. Tracing the β+ decay reveals either brain activity or tumors inside the body providing unprecedented insight in oncology and neuroscience (figure 2.5.D) [16].

Reconstruction of the origins of a multitude of events and their respective lines-of-response (LoR) reveal the tridimensional distribution of the radiotracer. This is a very broad field that combines various aspects, but a general description can be seen at figure 2.5 [17]. The LoRs (A,B,C,D in 2.5.A) resulting from coincidence events are plotted (2.5.B) as a function of their angular orientation versus their displacement from the center (X in 2.5.A). In the same manner all possible LoRs passing by a given point are plotted, forming a sinusoidal. For complex objects, all overlapping sine waves create the sinogram (figure 2.5.C), which can then be reconstructed (figure 2.5.D) through matrix transformations, to depict the subject under study.

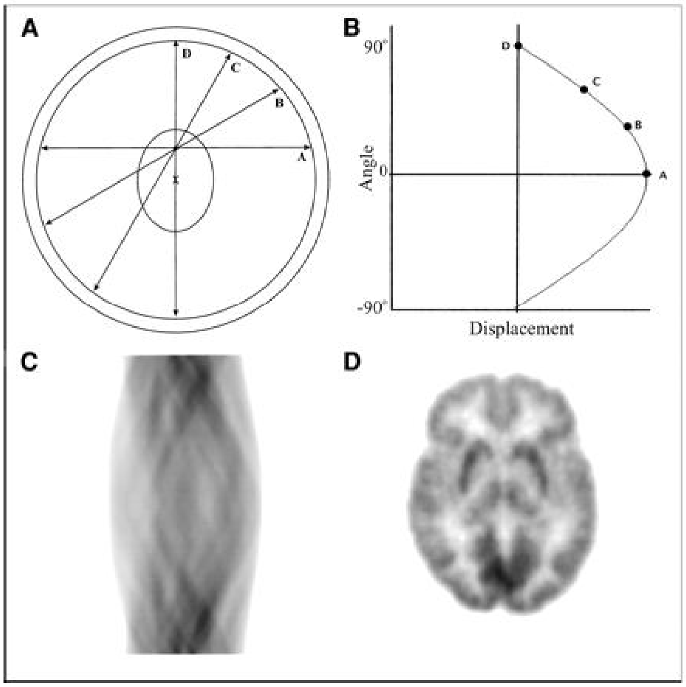

Figure 2. 4. Demonstration of reconstruction of the tridimensional image by projections resulting from the combination of LoRs [17]

After ^{18}F-FDG decays radioactively, the ^{18}F is converted to $^{18}O^{-}$. This atom then picks up a H^{+} from the aqueous environment of the cell, and the FDG molecule becomes glucose-6-phosphate with a non-radioactive "heavy oxygen" and a 2-hydrtheoxyl. In this new configuration the molecule is metabolized normally as ordinary glucose, producing non-radioactive end-products. Within 24 hours most of the fluorine has decayed and rejected from the organism in a safe and clean manner.

Production of radioisotopes to trace different functions and allow multi-isotope simultaneous acquisition of various processes is a standing goal of radio-biology [18]. Moreover, building novel appliances that could make isotope production [19] more accessible could revolutionize the outreach and broaden the application not only of PET, but also PET/CT and PET/MR.

C. *γ detection using scintillators*

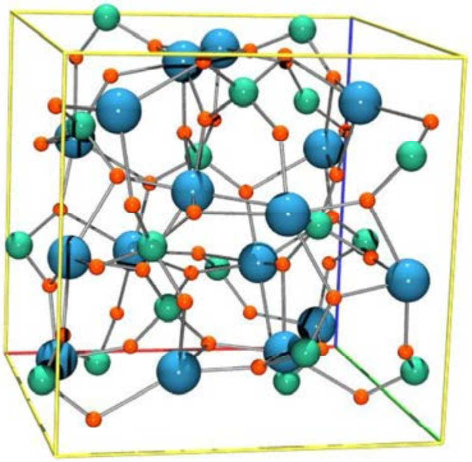

Figure 2. 5 Non-doped Bismouth germanate (BGO) crystal lattice unit cell. [20]

Since the beginning of development of PET instrumentation, existing particle detection techniques from fundamental and particle physics research were applied for the detection of annihilation produced γ pairs. The setting outline, which has not been rendered obsolete yet today, includes a scintillating material that produces visible or near ultraviolet light. An optically coupled battery of light to electric transformers, commonly named "photodetectors" captures the light and produces electric signals. Two important physical processes are taken advantage of and will be described in detail in the following paragraphs.

The first device which used a scintillator was built in 1903 by Sir William Crookes and used a ZnS screen. The scintillations produced by the screen were visible to the human eye if viewed by a microscope in a darkened room [21]. Even though visual scintillation counting was a very tedious experimental process, very significant results for the physical understanding of α particles were acquired [22].

A scintillator (figure 2.6) is a material that exhibits visible light when excited by ionizing radiation [19]. The three basic ways that a γ ray interacts with matter are the photoelectric effect, Compton scattering and pair production. A high atomic number inorganic crystal therefore, favors the former two processes and is predominantly used in PET, enabling the detection of the full energy of the γ and discrimination against different energy rays. If the γ rays are at higher than 5 MeV energies, pair production dominates.

In the materials of interest, the crystal lattice has impurities and functions in the following manner (figure 2.6): An incoming particle can excite an electron from the valence band. That electron jumps to either the conduction band or the exciton band leaving an associated hole behind, in the valence band. Impurities create electronic levels in the forbidden gap that are occupied by the excitons, loosely bound electron-hole pairs which wander through the crystal lattice until they are captured as a whole by impurity centers. On that event, a photon is emitted. The energy distance of the bands is in the order of few eV, thus the emitted photon falls within the visible/near ultraviolet band.

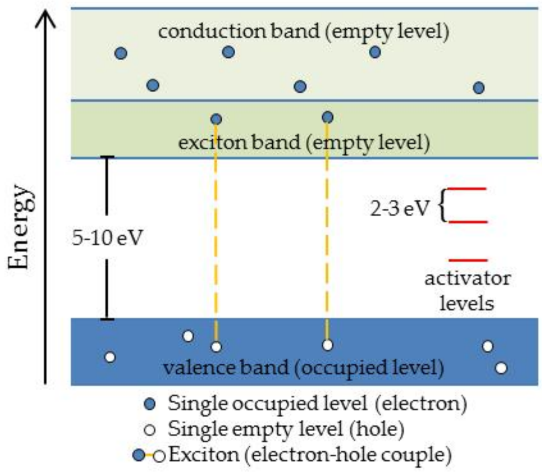

Figure 2. 6 Graphical description of the scintillation process energy levels

Having acquired a broad market and intense technological interest, novel scintillator crystals have been developed over the years and remain active as a research course for materials science. Physical properties, such as density, γ stopping power, hydroscopicity and doping; optical characteristics such as refractive index; and luminescence traits such as wavelength of emission, light yield and scintillation decay constant (how fast the energy of detected γ radiation has been released in the form of visible photons) vary greatly and are paramount for the design of a scintillation detector. Since the 1970s, bismouth germinate (BGO) has been broadly accepted as having the optimal tradeoff of characteristics for γ detection. Lutetium based scintillators later occupied a dominant position in radiation instrumentation, permitting better characterization of scintillation events, while newer, faster crystals are becoming gradually available. In table 2.1 an overview of different materials and their characteristics are shown.

Table 2. 1 Common scintillators and their properties [23-27]

Trait/crystal	NaI	BGO	LSO	LYSO	LuAG	LuAG	LaBr$_3$	GAGG	YAG
Light yield (photons/MeV)	45000	8500	33000	32000	11000	22000	63000	57000	22000
Decay constant (ns)	230	300	40	42	70	20	16	88	70
Max. wavelength (nm)	415	550	420	420	535	310	360	520	550
Refractive index	1.85	2.15	1.84	1.86	1.84	1.82	1.8	2.03	1.82
Hydroscopic	Yes	No	No	No	No	No	Yes	No	No
Density (g/cm^3)	3.67	7.13	7.4	7.2	6.73	6.7	5.8	6.63	4.57
Dopant	Tl	----	Ce	Ce	Ce	Pr	Ce	Ce	Ce

Doping element and concentration greatly affects the scintillating behavior of the crystal [26]. Furthermore, the intrinsic activity of certain isotopes present, especially the very common Lutetium, affects γ detection [28]. Nevertheless, the merits of lutetium based scintillator crystals are such, in sensitivity and pulse duration, that they are still considered the optimal choice for a big number of designs of future scintillation based detectors.

D. Detection of scintillation light

To develop a repeatable and less odious experimental process than visual scintillation counting, scientists in the 1940s already started developing and applying electronic circuits. In this manner the human boundary was lifted and higher rates, as well as radiation of smaller energy than α particles was made detectable, initially through the application of Geiger-Müller photosensitive counters [29]. Very soon, a new photodetection module was made available and put in operation in scintillator light detection, paving the way for the broad spectrum of applications currently available. This was the photomultiplier tube (PMT) [30]. Its principle of operation will be described based on figure 2.7 [21].

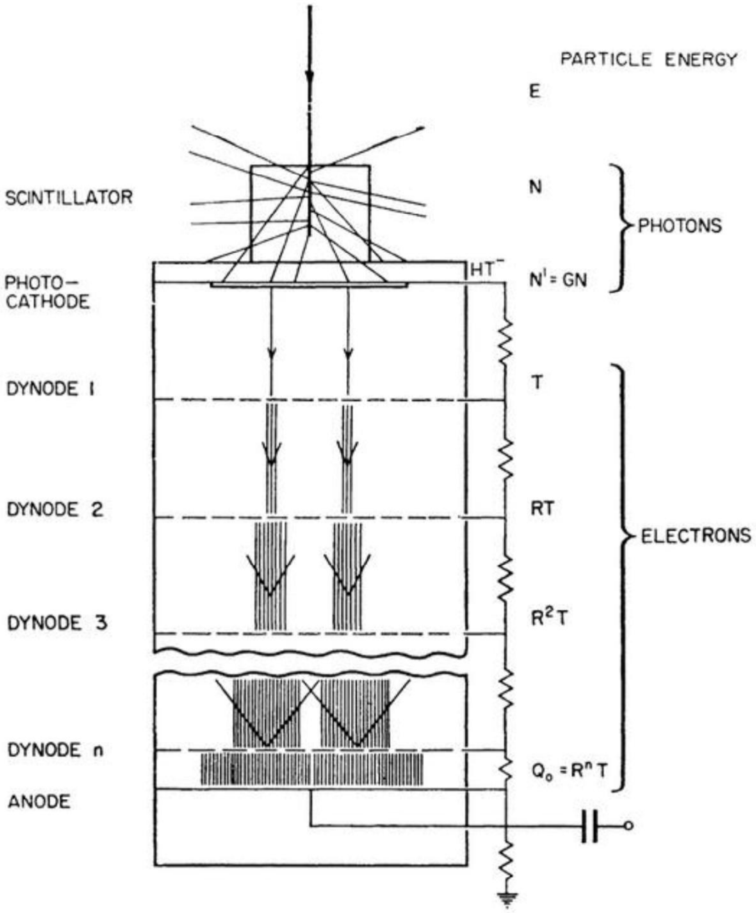

Figure 2. 7 Photomultiplier scintillation counter: Schematic diagram showing the sequence of physical processes.

From the N number of visible photons occurring due to the scintillating process, a percentage G is directed towards the photo-cathode. Some of these photons produce the emission of photoelectrons, which are attracted by the high potential of the first dynode, from which R times more photoelectrons are produced. The procedure is repeated n times, until finally the photoelectric signal, amplified by several orders of magnitude, is extracted at the anode. For high enough sensitivity, a high voltage in the order of hundreds to thousands V is necessary.

Along with technological evolution of PMTs (figure 2.8.A), alternative methods of photodetection where soon developed, taking advantage of solid state semiconductor design. Avalanche photodiodes (APD-figure 2.8.B), highly sensitive semiconductor electronic devices exploiting the photoelectric effect to convert light to electricity are the semiconductor analog to PMTs. Immense multiplication or amplification of the initial photoelectric signal is achieved through the avalanche breakdown phenomenon caused by a very high voltage [31]. APDs demonstrate high sensitivity and if operated with a reverse voltage above the APD's breakdown voltage, what is called Geiger mode, single photon detection is possible. With this principle single-photon avalanche diode (SPAD-figure 2.8.C) chips are also produced [32], comprising of numerous micrometer size diodes that detect single photons from scintillation, providing a quasi-digital signal at the output, further facilitating event characterization, especially on timing.

Another application design also sprouting from the APD principle is what is called silicon-photomultiplier (SiPM-figure 2.8.D). Those devices comprise of a similarly big number of micrometer size APDs in Geiger mode, albeit read in parallel in bigger groupings, while sharing the same silicon substrate. In this manner, a pseudo-analog signal is produced, allowing detection of a range of scintillator light, from single to thousand photons [33]. Bias voltage, due to refined silicon design, is reduced to the order of few tens of volts, rendering this architecture optimal for small and detached detector front-ends, while achieving far lower energy consumption than its quasi-digital counterpart.

With this detector design, the linear conversion of the energy of incurring γ, first to visible light through the scintillator and then to electric signal, was achieved, allowing for the precise and automatic measurement. Annihilation γ arriving at different pairs of detector elements are thus characterized by the location of detection, while the delay of conversion remains within known boundaries. In this way, a ring of such detectors could detect and discriminate by temporal coincidence and energy the pair of γ and locate the line of response (LoR) within which the positron annihilation occurred, inside the subject.

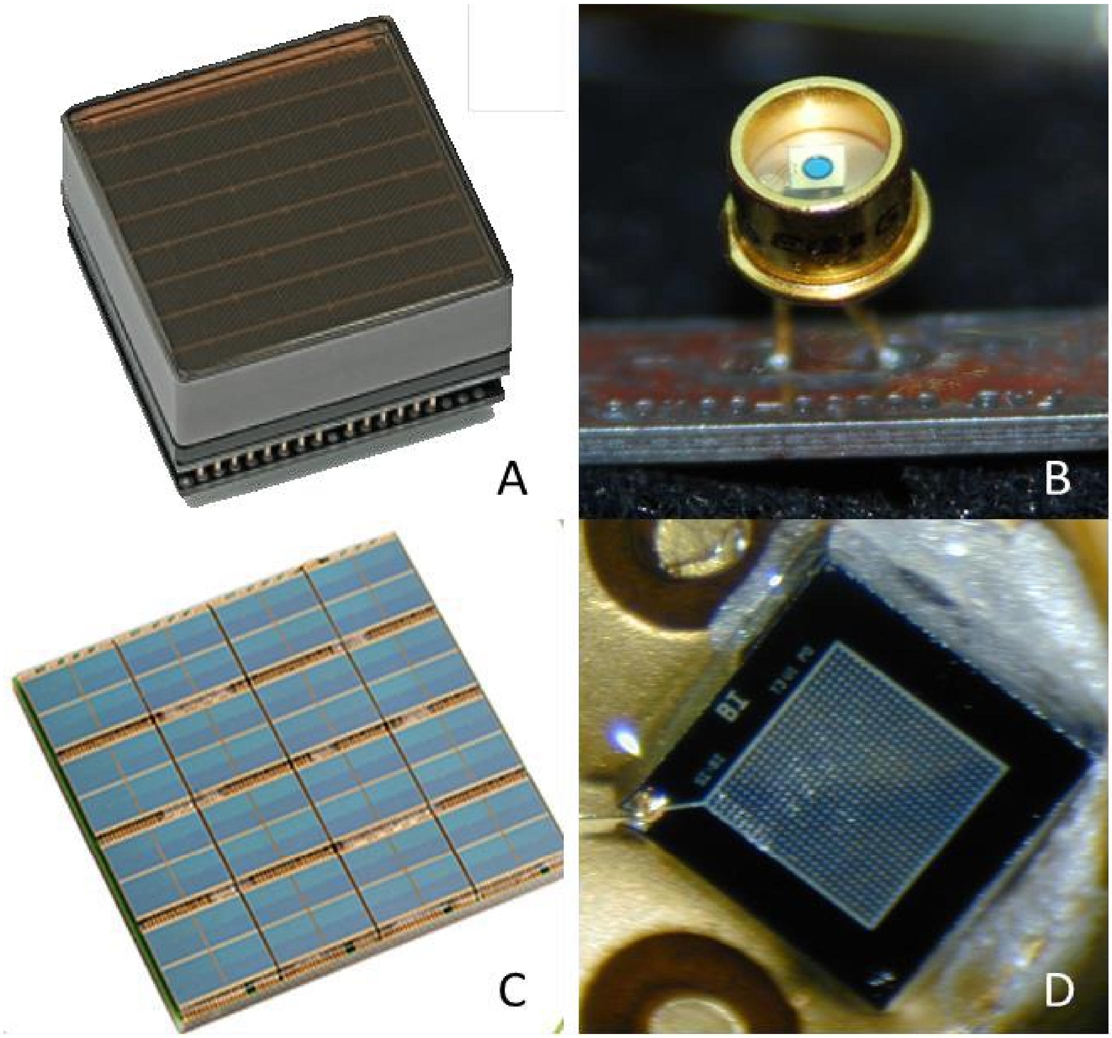

Figure 2. 8 A. Position- sensitive Hamamatsu H8500 PMT; B. APD (source-Wikipedia, CC); C. Philips digital photon counter, SPAD array; and D. FBK SiPM array

It can be deduced, of course, that higher density of smaller size distinguishable detector modules would produce more precise results, reducing the size of LoR. In this context, modern photodetectors comprise of smaller independent readout elements. Such granularity can occur in two manners. The one refers to photodetector pixelation. In this case, position sensitive photodetectors or a multitude of smaller independent ones are applied to detect the scintillation light and estimate the tridimensional location of its origin [34,35]. The other, concerns the pixelation of scintillators. In this approach, scintillators are cut in smaller size rods (pixels), which measure down to square millimeter size area in modern designs. The read out of these designs is performed by a position sensitive photodetector, in what is called “group coupling” or “block detector” approach [36]. This type of design is the standard for modern applications and will be further discussed in next chapters of this thesis.

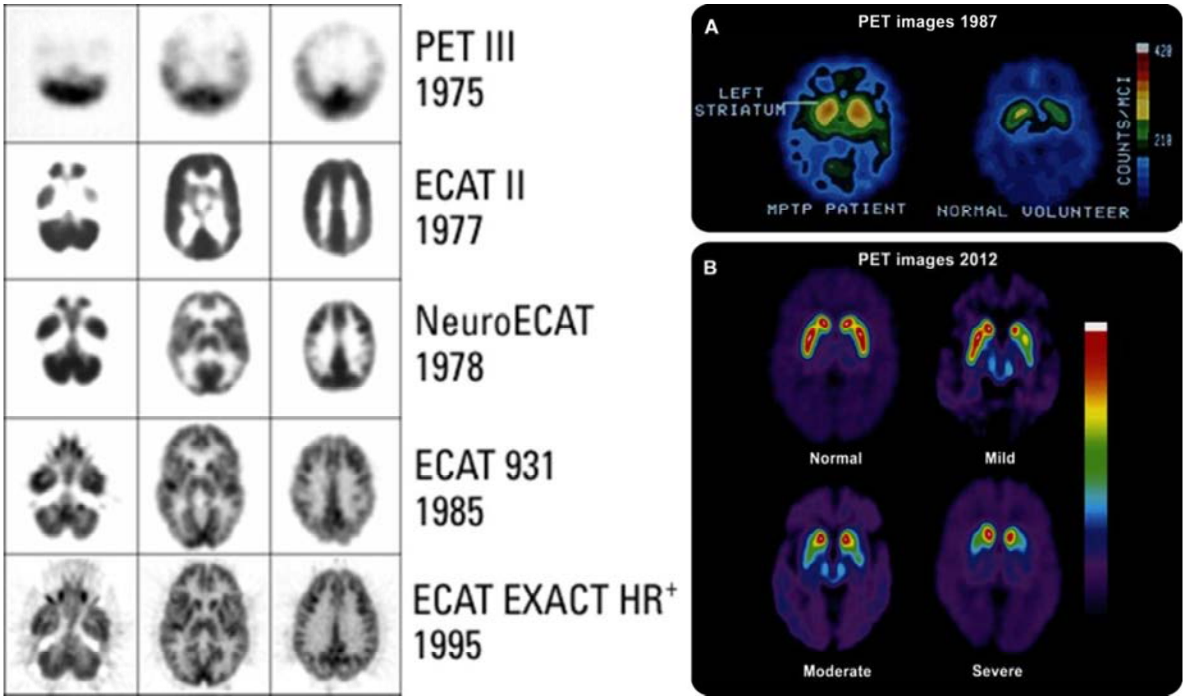

Figure 2. 9 Evolution of PET image demonstrating the development of resolution over the years; left 1975-1995 [37] and right 1987-2012 [38]

The basic PET detector is, thus, complete in principle and the field is open for improvement of its characteristics (figure 2.9), that will render it the scanner of choice for a multitude of medical and experimental scenarios.

E. PET detector specifications

Having reviewed the background knowledge in the previous paragraphs, it is necessary to delineate the desired features of detection that would characterize the quality of any novel detector design. Such characteristics concern the performance of the detector and correspond to the necessary trade-offs that need to be considered, as in every engineering project. In figure 2.9, the constant development of higher resolution images is profound; yet, from the detector development point of view, this evolution is not a simple issue, as a vast number of different factors need to be taken into consideration. The next paragraphs will be dedicated to the description of these factors.

The quality of the images we see in figure 2.9 is greatly affected by the detector's spatial resolution. As the purpose is tomography, a tridimensional depiction, the image quality is measured in the size of "voxels", volume-pixels. Several factors affect the size of voxel. Firstly, one shouldn't ignore the physical limitations, namely the positron range and noncollinearity, the errors of which are known, characterized in detail and unfortunately physically impossible to avoid. Another factor is the size of detector element, affecting the size of LoR, as mentioned before. The image reconstruction algorithm from planar projections always adds a significant and unavoidable error. Similarly, the proximity of detector elements, their small misalignments and the uncertainty due to occasional multiple interactions can be overlooked. A last part comes from the parallax error, the not exactly vertical line of sight that detectors have towards parts of the FOV. The spatial resolution is, thus, quantified in equation 2.1 and further explained in figure 2.10:

$$SR_{(FWHM)} = E_{rec}\sqrt{r^2 + (0.0022D)^2 + \left(\frac{d}{2}\right)^2 + b^2 + p^2} \qquad \text{equation 2.1}$$

where E_{rec} corresponds to the reconstruction algorithm error; r to the result of positron range; D to the distance between the detector elements affecting resolution due to γ pair noncollinearity; d to the equivalent dimension of the detector element; b resulting from coding/localization of detector elements; and p from the parallax error.

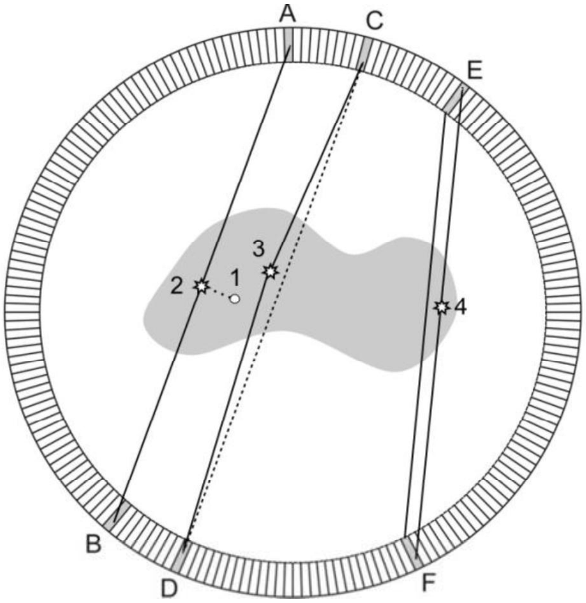

Figure 2. 10. Demonstration of positron range (1-2), noncollinearity (3) and parallax (4) errors

Looking in detail the figure 2.10, an inquiring mind might wonder why we don’t use scintillators of smaller depth. This indeed is a very vital issue, since the depth of scintillator affects directly the spatial resolution. The answer is that the sensitivity of the detector, meaning the amount of γ that can be detected from the multitude of the ones that are produced is, roughly, analogous to the mass of crystal. In this context, the stopping power of a detector corresponds to the density of scintillating material multiplied by the volume. This measure is also affected by the other materials that can be intersecting the scintillator, such as shielding and lightguides, leading to the equally important factor of packing ratio, the ratio of scintillating to non-scintillating material of the detector. Higher sensitivity leads to shorter examination times, a vital characteristic especially for human

PET. It can be theorized that resolution is more important than sensitivity for quantitation task performance, while sensitivity is a more significant issue for detection [39].

Nevertheless, this tradeoff is solved by the detection of depth of interaction (DoI) of the γ inside the scintillation crystal, a very important context in PET (figure 2.11). In this manner not only the aberration away from the center of the FOV is lowered, but also a bigger amount of LoRs can be considered, given that the differentiable depth levels of DoI can be seen as distinguishable detector elements.

DoI detection has led to various approaches on detector design, such as stacking pixels, different surface treatments [40], phoswich [41] and even readout of both sides of the scintillator [42], an approach facilitated by thin novel photodetectors, which are chip integrated and have minimum dimensions.

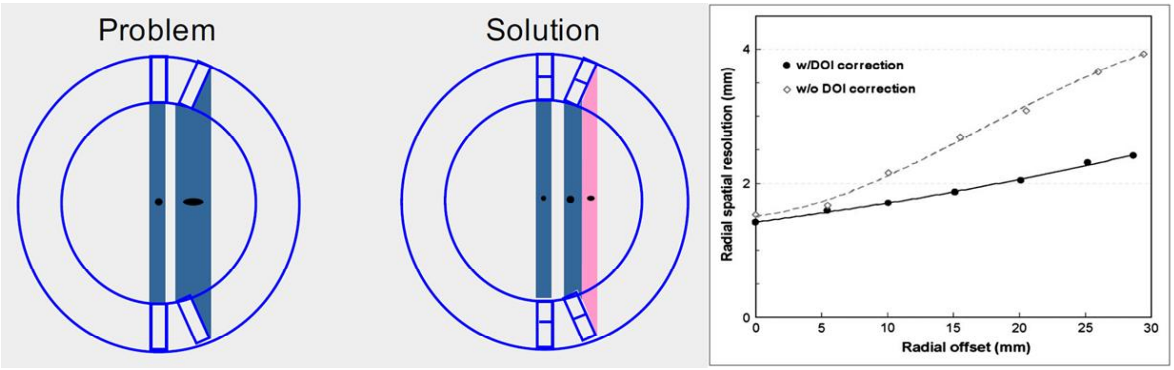

Figure 2. 11 (left) Demonstration of voxel deformation away from the center and solution; and (right) diagram of the effect of DoI correction

Earlier, it was mentioned how in order for γ pairs to be accurately attributed to corresponding pairs of detection events, energy and time coincidence of incurring radiation is detected. It is expected, in this context, that the resolution of measurement of these quantities is similarly vital as the spatial resolution. While, for the energy measurement, the linearity of conversion of γ radiation energy to electric signal solves the issue in the general sense, things are not equally straight-forward for the timing counterpart.

When we talk about the radiation inside the bore of a PET scanner, we shouldn't imagine a clean radiative environment, where only 511 KeV γ pairs are emitted by the annihilation of positrons from the radiotracer. In reality, a constant rate of γ photons is present, either due to the intrinsic radiation of the subject, detectors and environment, or from the cosmic radiation that constantly illuminates everything. Furthermore, the geometry of the scanner, which is not a closed solid, allows for pairs of γ to be lost, because only one is detected. In this framework, it is vital to have timing resolution as low as possible, in order to be able to confidently detect the actual coincidences and not falsely matched pairs of random singles [43]. Timing resolution factors are demonstrated in equation 2.2:

$$\Delta t \propto \frac{\sqrt{\tau}}{\sqrt{N_{ph}/_{ENF}}} \qquad \text{equation 2.2}$$

where τ is the slow component of scintillation light; N_{ph} the amount of photons produced by the fast component of the scintillator pulse per event; and ENF the excess noise factor, a characteristic of the photodetector, describing the statistical noise due to the stochastic multiplication process [44].

Another, more innovative, approach, made available with the development of sub-nanosecond detectors, is the calculation of time of flight (ToF) of the coincidence γ. Being able to detect at which length of the LoR the event took place greatly enhances the signal-to-noise ratio (SNR) and thus the quality of the image, as demonstrated in figure 2.12, In A, the possibility distribution of an event taking place at a particular length of the LoR, for conventional and ToF scanners, is demonstrated; B shows how this leads to better reconstruction with the same amount of events; and C how this directly affects the quality of the final produced medical image, which is sharper for the same amount of counts, as compared to the conventional approach. ToF is considered the new frontier for PET and the contemporary call is for scanners that will break the 100 picoseconds barrier of timing resolution, corresponding to 3 cm [45].

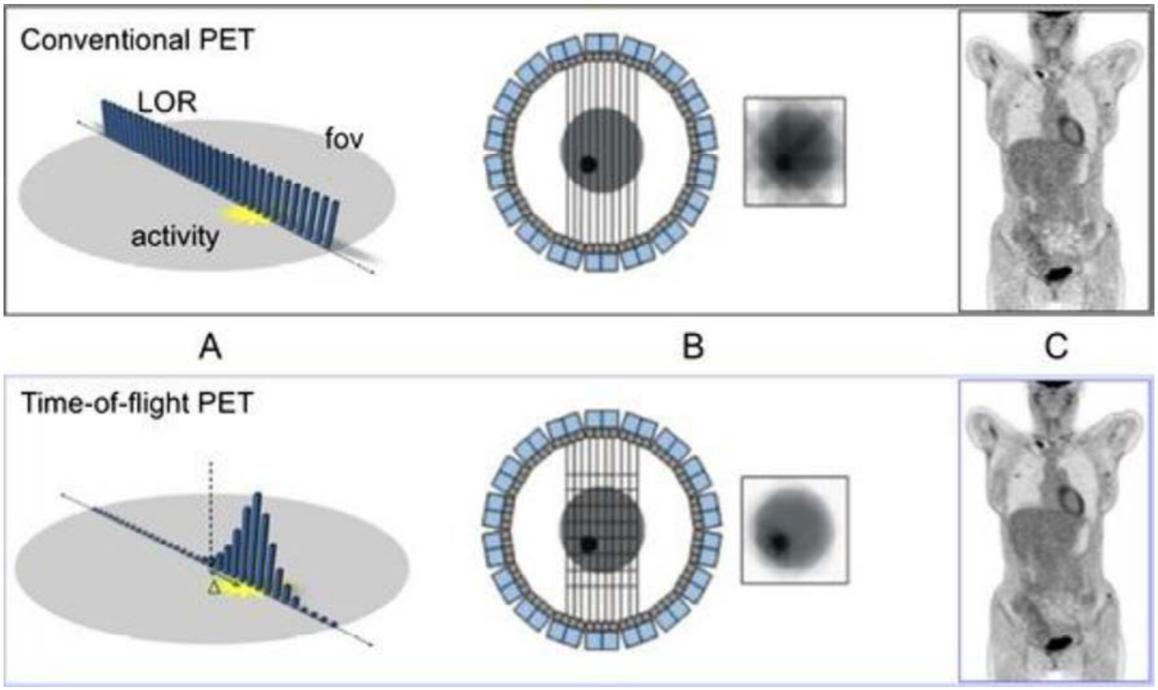

Figure 2. 12 Conventional versus ToF PET [46].

It can be perceived how the scintillator choice plays a vital role in timing, while the photodetector design is also important. Recently, sprouting from the ease of single photon detection, prompt Cherenkov light occurring due to particle production associated with scintillation, has been considered as an interesting candidate for more precise attribution of time of arrival of a γ. The corresponding energy measurement of scintillation remains the same as before [47]. Expanding this idea, Cherenkov PET without scintillator has also been proposed [48].

F. Small animal scanners and PET inserts

The characteristics mentioned up to now concern all PET scanners. Small animal scanners are not commonly found in medical scenarios and are mainly used for experimental purposes, what is covered by the term preclinical imaging (figure 2.13), the visualization of small animals for research purposes. As can be deduced, the specifications necessary for the tracking of vital functions of small animals, usually mice and rats, is several orders of magnitude higher than those of human, due to the vast difference in size. Indeed, an average adult human male weighs around 75 kg, while the equivalent average adult rat around only 250 g, an approximate 300 times. Another issue is the difficulty in conscious acquisition, given the tedious experience entering a tomograph bore is [49]. Nevertheless, small animal PET scanners already provide a very important laboratory solution for studies of neuroscience and drug trials in vivo (figure 2.14 left), saving the lives of thousands of laboratory animals by greatly lowering the amount of them that need to be used for a trial, providing precise in vivo imaging and in the same manner accelerating greatly the experimental research effort [50].

Figure 2. 13 SEDECAL Super Argus PET/CT preclinical imager

On the other hand, an interesting parallelism is developed, as it is exactly through these experimental applications that innovative designs of PET scanner find first application, researching technological possibilities in smaller sized designs. Precisely for this reason, our study of MR compatible PET inserts, in a similar manner like a good part of the already existing approaches, primarily concern small animal designs.

Figure 2. 14 (Left) RatCAP, conscious rodent brain PET scanner; and (right) human brain PET [51].

Such designs can be adapted relatively easily for single organ PET designs, such as brain PET (figure 2.14 right) or mammographic PET. This is a pivot of particular interest, since with the supreme sensitivity PET provides very important insight not only on cancer diagnosis for usual cases such as breast cancer, but furthermore on common neurological diseases such as Alzheimer's or Schizophrenia [52], which thus can be detected at an early stage, becoming curable, a groundbreaking frontier for the quality of life in modern societies. However, before eventually finding application in whole human body designs, several considerations on scaling up and human suitability must be answered.

REFERENCES

[1] Bijker, W. E., Hughes, T. P., Pinch, T., & Douglas, D. G. (2012). The social construction of technological systems: New directions in the sociology and history of technology. MIT press.

[2] Del Guerra, A., Belcari, N., & Bisogni, M. (2016). Positron Emission Tomography: Its 65 years. RIVISTA DEL NUOVO CIMENTO, 39(4), 155-223.

[3] Sweet, W. H. (1951). The uses of nuclear disintegration in the diagnosis and treatment of brain tumor. New England Journal of Medicine, 245(23), 875-878.

[4] Brownell, G. L., & Sweet, W. H. (1953). Localization of brain tumors with positron emitters. Nucleonics, 11(11), 40-45.

[5] Thompson, C. J., Yamamoto, Y. L., & Meyer, E. (1979). Positome II: A high efficiency positron imaging device for dynamic brain studies. IEEE Transactions on Nuclear Science, 26(1), 583-589.

[6] Hoffman, E. J., Phelps, M. E., Huang, S. C., Plummer, D., & Kuhl, D. E. (1982). Evaluating the performance of multiplane positron tomographs designed for brain imaging. IEEE Transactions on Nuclear Science, 29(1), 469-473.

[7] Massoud, T. F., & Gambhir, S. S. (2003). Molecular imaging in living subjects: seeing fundamental biological processes in a new light. Genes & development, 17(5), 545-580.

[8] Townsend, D. W. (2008, August). Combined positron emission tomography–computed tomography: the historical perspective. In Seminars in Ultrasound, CT and MRI (Vol. 29, No. 4, pp. 232-235).

[9] Del Guerra, A. (2004). Ionizing radiation detectors for medical imaging. World Scientific.

[10] Fasso, A., Göbel, K., Höfert, M., Ranft, J., & Stevenson, G. (1990). 4.2. 1 Ionization energy loss and multiple Coulomb scattering. In Shielding Against High Energy Radiation (pp. 358-360). Springer Berlin Heidelberg.

[11] Knoll G. (2010), Radiation Detection and Measurement. John Wiley & Sons.

[12] George, N., Gean, E. G., Nandi, A., Frolov, B., Zaidi, E., Lee, H., ... & Wong, D. F. (2015). Advances in CNS Imaging Agents: Focus on PET and SPECT Tracers in Experimental and Clinical Use. CNS drugs, 29(4), 313-330.

[13] Pacak J, Tocik Z, Cerny M (1969). "Synthesis of 2-Deoxy-2-fluoro-D-glucose". Journal of the Chemical Society D: CHEMICAL COMMUNICATION: 77–77.

[14] Newberg A, Alavi A, Reivich M (2002). "Determination of regional cerebral function with FDG-PET imaging in neuropsychiatric disorders". Semin Nucl Med. 32 (1): 13–14. doi:10.1053/snuc.2002.29276. PMID 11839066.

[15] Som P, Atkins HL, Bandoypadhyay D, Fowler JS, MacGregor RR, Matsui K, Oster ZH, Sacker DF, Shiue CY, Turner H, Wan CN, Wolf AP, Zabinski SV (1980). "A fluorinated glucose analog, 2-fluoro-2-deoxy-D-glucose (F-18): Nontoxic tracer for rapid tumor detection". J Nucl Med. 21 (7): 670–675. PMID 7391842.

[16] Fowler JS, Ido T (2002). "Initial and subsequent approach for the synthesis of 18FDG". Semin Nucl Med. 32 (1): 6–12. doi:10.1053/snuc.2002.29270. PMID 11839070.

[17] Fahey, F. H. (2002). Data acquisition in PET imaging. *Journal of nuclear medicine technology*, *30*(2), 39-49.

[18] Herzog, H., Tellmann, L., Qaim, S. M., Spellerberg, S., Schmid, A., & Coenen, H. H. (2002). PET quantitation and imaging of the non-pure positron-emitting iodine isotope 124 I. Applied radiation and isotopes, 56(5), 673-679.

[19] Schmor, P. W. (2010). Review of cyclotrons used in the production of radioisotopes for biomedical applications. In Proc. of the 19th International conference on cyclotrons and their applications (pp. 419-424).

[20] Mark Foreman personal web page, Chalmers University of Technology. Retrieved 09/12/2016

[21] Leo, W. R. (1990). Techniques for Nuclear and Particle Physics Experiments. Dr155.

[22] Birks, J. B. (2013). The Theory and Practice of Scintillation Counting: International Series of Monographs in Electronics and Instrumentation (Vol. 27). Elsevier.

[23] Crytur, Palackeho 175, 511 01 Turnov, Czech Republic

[24] EPIC crystals ,Rm 972, Block D, Zhongyin Int. Corp. Garden, Hyaqiao Town, Kunshan, Jiangsu 215332, China

[25] Furukawa Densi co. ltd, 1-25-13, Kannondai, Tsukuba-city, Ibaraki, 305-0856, Japan

[26] S. Derenzo, M. Boswell, M. Weber & K. Brennan, Scintillator properties, LBNL and DHS, http://scintillator.lbl.gov/, retrieved on 9/12/2016

[27] M. A. Spurrier, P. Szupryczynski, K. Yang, A. A. Carey and C. L. Melcher, "Effects of Ca2+ Co-Doping on the Scintillation Properties of LSO:Ce," in IEEE Transactions on Nuclear Science, vol. 55, no. 3, pp. 1178-1182, June 2008. doi: 10.1109/TNS.2007.913486

[28] Wei, Q. (2015). Intrinsic Radiation in Lutetium Based PET Detector: Advantages and Disadvantages. arXiv preprint arXiv:1501.05372.

[29] Krebs, A. (1955), Szintillationszähler, Ergebn. exakt. Naturwiss. 27, 361

[30] Marshall, F. H., Coltman, J. W., & Hunter, L. P. (1947). The Photomultiplier X-Ray Detector. Review of Scientific Instruments, 18(7), 504-513.

[31] Jaeger, R. C., & Blalock, T. N. (1997). Microelectronic circuit design (Vol. 97). New York: McGraw-Hill.

[32] Cova, S., Ghioni, M., Lacaita, A., Samori, C., & Zappa, F. (1996). Avalanche photodiodes and quenching circuits for single-photon detection. Applied optics, 35(12), 1956-1976.

[33] Saveliev, V. (2010). Silicon photomultiplier-new era of photon detection. INTECH Open Access Publisher.

[34] Anger, H. O. (1964). Scintillation camera with multichannel collimators. *Journal of Nuclear Medicine*, *5*(7), 515-531.

[35] Maas, M. C., van der Laan, D. J., Schaart, D. R., Bruyndonckx, P., Lemaître, C., & van Eijik, C. W. E. (2005, October). Performance of APD-based monolithic-crystal detectors for small animal PET. In IEEE Nuclear Science Symposium Conference Record, 2005 (Vol. 4, pp. 5-pp). IEEE.

[36] Uchida, H., Yamashita, T., Iida, M., & Muranatsu, S. (1986). Design of a mosaic BGO detector system for positron CT. *IEEE Transactions on Nuclear Science*, *33*(1), 464-467.

[37] R.M.E Sabbatini (1997), he PET Scan: A New Window Into the Brain, Brain & Mind Magazine.

[38] Portnow, L. H., Vaillancourt, D. E., & Okun, M. S. (2013). The history of cerebral PET scanning: From physiology to cutting-edge technology. Neurology, 80(10), 952–956.

[39] Lee, K., Kinahan, P. E., Miyaoka, R. S., Kim, J. S., & Lewellen, T. K. (2004). Impact of system design parameters on image figures of merit for a mouse PET scanner. IEEE transactions on nuclear science, 51(1), 27-33.

[40] G. Konstantinou, R. Chil, M. Desco and J.J. Vaquero, "Applications of SSLE on Monolithic Scintillator Crystals: Novel Pixel Geometries and Depth of Interaction", In *IEEE NSS/MIC,* Oct 2016.

[41] J. J. Vaquero, J. J. Sánchez, E. Lage, J. M. Udías, P. Guerra and M. Desco, "Design of DOI PET detector modules using phoswich and SiPMs: First Results", In *IEEE NSS/MIC,* pp. 3311-3313, Oct 2011

[42] Braem, A., Chamizo, M., Chesi, E., Colonna, N., Cusanno, F., De Leo, R., ... & Nappi, E. (2004). Novel design of a parallax free Compton enhanced PET scanner. Nuclear Instruments and Methods in Physics Research Section A: Accelerators, Spectrometers, Detectors and Associated Equipment, 525(1), 268-274.

[43] Farncombe, T., & Iniewski, K. (Eds.). (2013). Medical Imaging: Technology and Applications. CRC Press.

[44] Hyman, L. G. (1965). Time resolution of photomultiplier systems. Review of Scientific Instruments, 36(2), 193-196.

[45] Nemallapudi, M. V., Gundacker, S., Lecoq, P., Auffray, E., Ferri, A., Gola, A., & Piemonte, C. (2015). Sub-100 ps coincidence time resolution for positron emission tomography with LSO: Ce codoped with Ca. Physics in medicine and biology, 60(12), 4635.

[46] http://knowyourimages.blogspot.fr/2013/02/time-of-flight-pet-vs-mra.html. Retrieved on Jan 5, 2017.

[47] Vandenberghe, S., Mikhaylova, E., D'Hoe, E., Mollet, P., & Karp, J. S. (2016). Recent developments in time-of-flight PET. EJNMMI physics, 3(1), 1.

[48] Yvon, D., Renault, J. P., Tauzin, G., Verrecchia, P., Flouzat, C., Sharyy, S., ... & Starzynski, P. (2014). Calipso: An novel detector concept for PET imaging. IEEE Transactions on Nuclear Science, 61(1), 60-66.

[49] Schulz, D., Southekal, S., Junnarkar, S. S., Pratte, J. F., Purschke, M. L., Stoll, S. P., ... & O'Connor, P. (2011). Simultaneous assessment of rodent behavior and neurochemistry using a miniature positron emission tomograph. nAture methods, 8(4), 347-352.

[50] Kiessling, F., Pichler, B. J., & Hauff, P. (2011). Small animal imaging. Springer, Berlin Heidelberg.

[51] Tashima, H., & Yamaya, T. (2016). Proposed helmet PET geometries with add-on detectors for high sensitivity brain imaging. Physics in Medicine and Biology, 61(19), 7205.

[52] Del Guerra, A. (2015). TRIMAGE–Development of a Simultaneous Trimodal (PET/MR/EEG) Imaging Tool for Early Diagnosis of Schizophrenia and Other Mental Disorders. European Psychiatry, 30, 161.

Chapter 3: A feasibility study of Sub-Surface Laser Engraving for scintillators

I. INTRODUCTION

In the previous chapter it was discussed how the scintillator characteristics affect greatly both spatial resolution as well as sensitivity of a position sensitive γ radiation detector. Moreover, it was commented under what circumstances those two features are conflicting, especially through the parallax error lowering spatial resolution for longer scintillators, necessary for higher sensitivity [1]. This vital tradeoff has been an important line of investigation of nuclear instrumentation researchers. One aspect is the improvement of packing fraction [2, 3]. As can be theorized, the optimal configuration for maximizing sensitivity would comprise of a closed solid within which the subject under study is placed, surrounded by infinite length of continuous scintillating material, while the produced visible light would be detected by non-dimensional photodetectors with maximum efficiency. In this manner, only an infinitesimal percentage of the total activity would elude detection. Of course, this is not compatible with enhanced spatial resolution under current technologies, which most commonly require pixels (figure 3.1) [4].

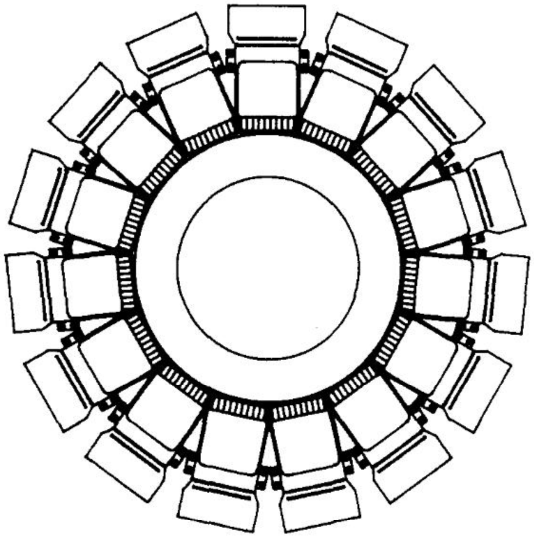

Figure 3. 1 A typical pixelated detector ring configuration. The radial lines at scintillator level correspond to pixelation light-guiding, deteriorating the packing fraction [4].

Pixelation for scintillator detectors corresponds to a simple principle: The light produced by a scintillation event should be contained within a crystal volume with as small as possible a cross section with the photodetector. This light is then detected and the transverse (X and Y) coordinates of detection, coinciding with that cross section, also correspond to those of the event. The way to optimization of this principle varies greatly with the type of photodetector, the manner the scintillator is optically coupled to it and the way it is read out. In most cases some light-sharing among scintillator elements improves the precision of detection, while the ideal alternative is when there is an one-to-one coupling between scintillator element and photodetector. The location of a scintillation event within the pixel is not directly known, the elemental detector being thus formulated and characterized by the dimensions and attributes of pixelation.

Consequently, optical wave-guiding (light-guiding) should be established within the scintillating material. Furthermore, in order for the energy conversion of a γ event to be linear, light guiding should take place in a controlled manner, meaning that if a percentage of light is lost or shared, it should be known and taken into account [5]. Different approaches have been tried and are still in application, including pixel surface treatments, paints and thin plastic reflector films [6, 7], this last being the way these considerations have very frequently been answered in clinical and preclinical PET systems (figure 3.2). Such films, very commonly applied, are Teflon [8], Vikuiti [9] and $BaSO_4$ [10], among others. These have excellent optical characteristics at the light band of emission for the most common scintillators [11], while furthermore being cost effective, readily available and relatively easy to apply, as compared to special pixel surface treatments, for instance.

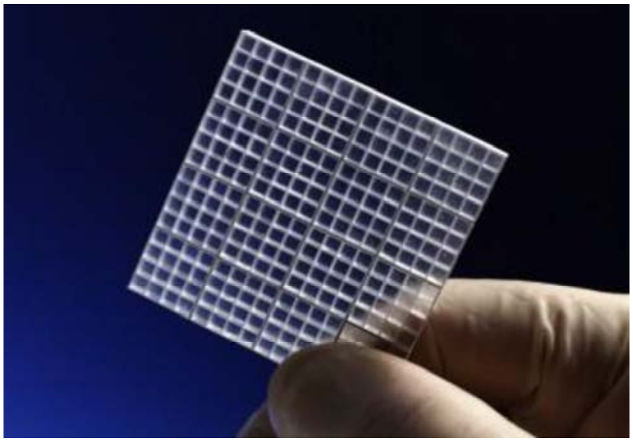

Figure 3. 2 A grid of reflector to be used for light-guiding in scintillators [12].

Unfortunately all these possibilities affect the sensitivity specifications of the detector. A pair of γ rays resulting from annihilation, where one of the two rays crosses through the reflector, will not be detected. The statistical possibility of this occasion is counted by the surrogate of the non-scintillating reflector to total detector surface ratio, an application of the packing fraction metric for pixelated arrays. The total performance of the detecting system is determined by this factor in a great extent.

Alternative methods for high resolution, without the application of standard pixelation techniques have been presented [13, 14]. The main problem with these is that they require the application of digital photomultipliers. Main disadvantage of these is the very high power consumption, while moreover multiplexing of readout channels is not permitted before digitalization. In this manner the data read-out chain is strenuously extended to unnecessary breadths, given the sparse nature, in time and space, of the physical phenomenon under study [15].

Another viable alternative is the application of sub-surface laser engraving (SSLE) techniques for scintillator crystals [16, 17]. A variety of custom-made setups that combine nanosecond and picosecond lasers have been used to implement this process and results have been demonstrated. Readout and detector architecture are the same as for standard pixelated arrays. Even though this technique has been previously presented, yet the extent of advantages of such method of pixelation only starts to unfold. Furthermore, it is anticipated that the cost, associated with building a variable system, since cost-optimized solutions for laser characteristics and system development can't be found in literature, would be prohibitively high.

Nevertheless, this approach was the first considered for the development of novel radiation detector front-ends in our research. The scintillator of choice would be Lutetium-yttrium oxyorthosilicate, also known as LYSO. As can be seen in table 2.1, this scintillator has supreme light yield and very high density; is not hydroscopic facilitating manipulation; shows very good timing characteristics; and due to it being used very extensively, relatively lower cost of development could be foreseen. A drawback for LYSO is the intrinsic radiation of Lutetium, with main spectrum peaks far from the 511 KeV, that is of interest in PET.

Thus, this chapter will focus on the study we performed on the viability and application of what has all the characteristics to be the next standard: the SSLE approach for LYSO scintillators, through studying and applying a very cost effective system of engraving.

II. MATERIALS AND METHODS

A. SSLE process

SSLE refers to the process of controlled local destruction below the surface of a transparent solid by focusing a laser. Each material has a laser-induced damage threshold (LIDT). The optical power density rises approaching the focal point and when the LIDT is exceeded, small fractures are created [18]. These fractures depend on the exact local conditions, on structural characteristics of the transparent material such as its crystal mesh, but also on the size of focal point and power density. They might have, favorably, a size of a few micrometers, hence called "microcracks" or, in case the accumulated power is much higher, they might form big cracks of several millimeters that propagate through the material, even away from the engraved point. The form of these is difficult to control, model or use for light-guiding.

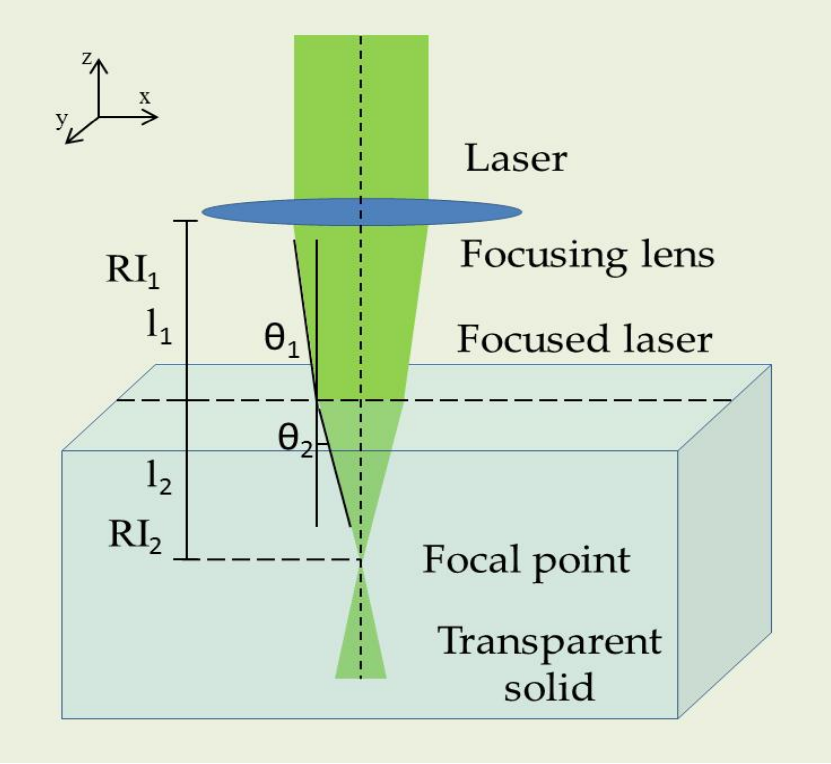

Figure 3. 3 Geometry of SSLE process conceptual demonstration

As demonstrated in figure 3.3, the x, y, z coordinates of the focal point are a function of the distances l_1, l_2 between the focusing lens and solid surface; position x, y of the solid; and angles θ_1, θ_2 which are related to the refractive index of air RI_1 and that of the solid RI_2 through Snell's law. A computer aided design (CAD) system can make the necessary transformations and guide a controllable tridimensional distribution of points.

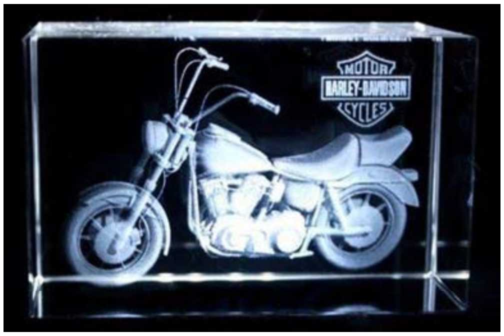
Figure 3. 4 Example of SSLE for commercial applications [19]

Commonly, high-grade optical quality materials, such as BK7 glass, are used to minimize distortion of the beam. The most usual commercial application is for touristic souvenir engravings, like in figure 3.4. The technique has been tried in different transparent materials, such as plastics. Since laser technology is becoming increasingly accessible, setting up a system or customizing an existing one becomes easier. Neodumium doped Ytrium Aluminium Garnet (Nd:YAG) based solid state lasers [20] can provide the power necessary for SSLE, while a computer aided design (CAD) system can provide the guidance necessary for motors.to move accordingly and recreate the x, y, z coordinates.

Taking advantage of the high optical transmittance of most inorganic scintillators in the visible band [21], a grid of this type of microcracks could be engraved. The specifics of engraving scintillators, in absence of literature and taking into account the novel characteristic of such approach remained to be researched. Nevertheless, a grid of such microcracks could provide the reflective structure needed to produce light-guiding pixels, without the necessity of physically separating the segmented pixels with mechanical tools. Control within a range of the optical characteristics and geometry of the optical barriers functioning as reflectors is provided and could be exploited. In this context, topologies such as hexagons, uneven size of pixels to compensate for separators between the photodetector elements, controlled light sharing or depth of interaction approaches would be possible to design. Most importantly, while respecting fundamental characteristics of the crystal material and limitations on the optical characteristics of the produced surfaces is paramount, the study and development of any design can happen from monolithic scintillating blocks at absolutely no additional cost.

B. Study and introduction of a cost-effective system

In the previous paragraphs the cost of a system capable of engraving scintillators has not been commented in detail. Indeed, existing approaches [16] had limitations related to the characteristics of produced laser pulse, such as pulse energy and duration, as can be understood by the upgrade in [17]. The problem arising is that building complex laser systems, while possible, can lead to severe cost rise, to the extent that a research group is not able to handle, as a very big amount of crystals should be engraved in application level to compensate for the investment. Furthermore, it is a skillset quite separate from nuclear medicine detector engineering, requiring a multidisciplinary approach.

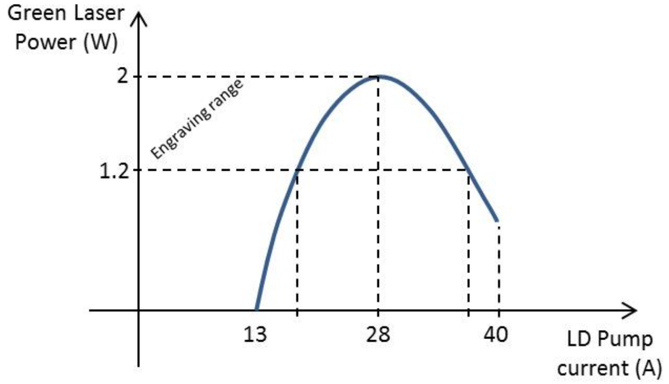

Figure 3. 5 Information of the engraving setup, relation of pump current with laser power

Taking all these into account, we came in contact with a Chinese company [22] that develops laser systems and discussed the possibility of procuring and customizing a cost-effective SSLE setting that would be able to engrave scintillator crystals. To confirm this, a study of comparison of a commercial system with the information that could be retrieved from existing literature [16] was performed. From information provided by the company engineers (figure 3.5), the LD pump current is the main factor controlling the energy per pulse. From the same information source, we found out that the average pulse duration is not controllable in this system and lies between 6.8 and 7.2 ns and averages at 7 ns. On the other hand, the engraving rate lies between 1 and 3 KHz, upper limit due to pump energy limitations. Pulse energy and power was possible to calculate by application of fundamental laws of physics (Equation 3.1, 3.2)

$$E_{focal} = \frac{E_{pulse}}{A_{focal}}, \qquad \text{Equation 3.1}$$

$$P_{pulse} = \frac{E_{pulse}}{t_{pulse}} \qquad \text{Equation 3.2}$$

Then, we procured a commercially available customized model, applying an Nd:YAG laser of 532 nm (green) after frequency splitting. The setup is integrated with a 3D translation stage as well as a basic movement control software, customized by the producer to fit our needs (figure 3.6). For a tridimensional pattern to be engraved with this machine, it is necessary to produce a CAD design. We used Autocad (Autodesk, 111 McInnis Parkway, San Rafael, CA 94903). The produced architecture had then to be enhanced with control information on engraving profiles, laser pulse energy, engraving rate and pauses. The final produced file of SCADA form, an industrial control programming language, is provided to the machine through a custom built parallel IO card through the PCI express bus. Through this, the engraving is controlled by steps at the x, y, z motors or by fine tuning the angle of the lens in the focusing unit (figure 3.6).

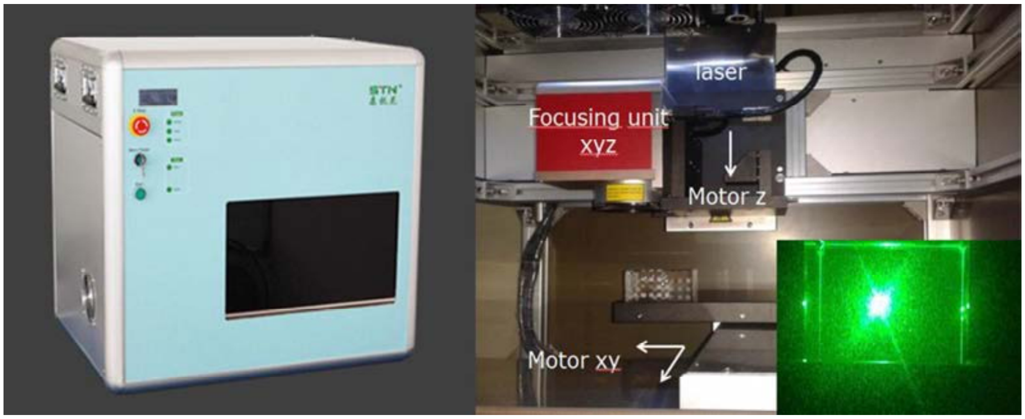

Figure 3. 5 (left) the commercial model; (right) internal structure; and (indexed right) an individual laser pulse at 532 nm (green)

C. *BK-7 testing and photometric experiments*

While our intention was to engrave LYSO, initial testing took place on inexpensive BK-7 glass blocks. This was done due to the cost associated with inorganic scintillators. While there are several differences between these two transparent materials, it was expected that very important insight and experience would be provided by such testing.

In this context, a vast amount of 5x5 mm^2 areas were engraved with different microcrack designs and engraving parameters, in order to be able to assess the effect that these features had on engraving surfaces. These included the voltage and current for the LD pump; rate of engraving, thought to affect the final shape of microcracks due to temperature gradient in the area of engraving; density and tridimensional distribution of engraved points; direction of engraving and grouping of engraved points; and step of the servo motor system. From these parameters a number of resulting surfaces needed be evaluated and since the intension was to create sub-surface light-guides inside scintillators, the reflective characteristics were thought to be paramount for this feature along with the thickness.

For such measurement, an photometric experiment would be necessary. A selective plane illumination microscopy (SPIM) setting was readily available [23] in our laboratory. While these microscopes are intended to provide numerous projections by recording the fluorescence under different illumination and changing the focusing plane inside a biological sample, constructing in this manner a tridimensional image, their function can be adapted in order to provide high precision, quantifiable images of the surfaces created by SSLE (figure 3.7 left).

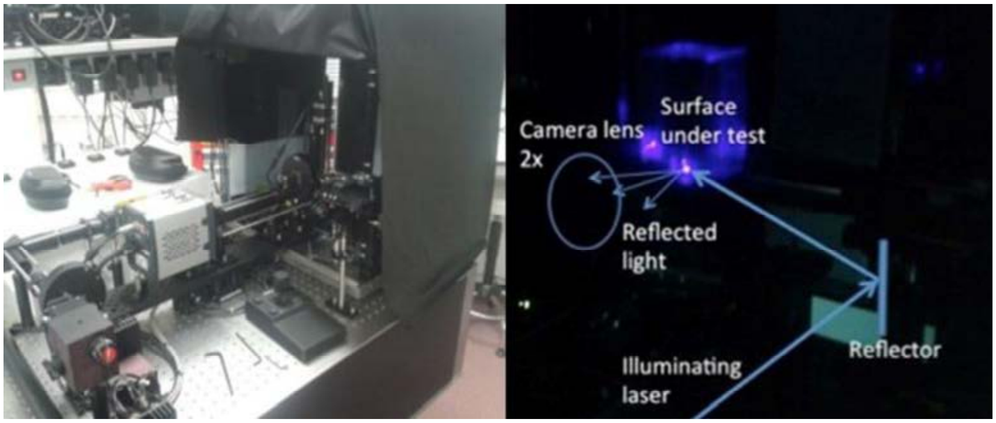

Figure 3. 6 (right) SPIM system; and (left) concept diagram of SPIM based photometric experiment

A simplified diagram to explain the operation can be seen in figure 3.7, right. Illuminating lasers of wavelength of 406 nm and 473 nm, around the wavelength of emission of LYSO (420 nm peak) [24], where used to illuminate the surfaces under test. The reflected light was focused by a lens to a monochromatic high resolution scientific CMOS camera. A white reflector strip (Lumirror) placed side by side to the engraved surfaces was measured at the same time and its image was used as the normalization reference.

Nevertheless, the SPIM system functionality is used to a very small fraction for the experimental procedure intended, as for the bulk of the measurements necessary to assess further characteristics of the surfaces, a simpler setup could suffice. From initial estimations, the different illumination wavelengths results were compared and even though a big discrepancy was found at absolute values, the normalized series presented 0.89 Pearson product-moment correlation (PPMC) coefficient. In this manner it was considered possible to continue with only 473 nm, a wavelength (blue) more easily available on light sources and camera filters.

In the same context a smaller and more versatile setup was built, using incoherent illumination of 473 nm provided by a blue LED, a simple focusing lens and a scientific Thorlabs DCC1545M high resolution monochromatic CMOS camera (figure 3.8). The quality of measurement of the second setup was confirmed through experimentation with the same series of surfaces as with the SPIM setup and confirmation that the provided results were similar (0.91 PPMC). A selection of four 5x5 mm^2 surfaces is presented in figure 3.8 right, as visibly differentiable cases of high density (top) and high energy (right).

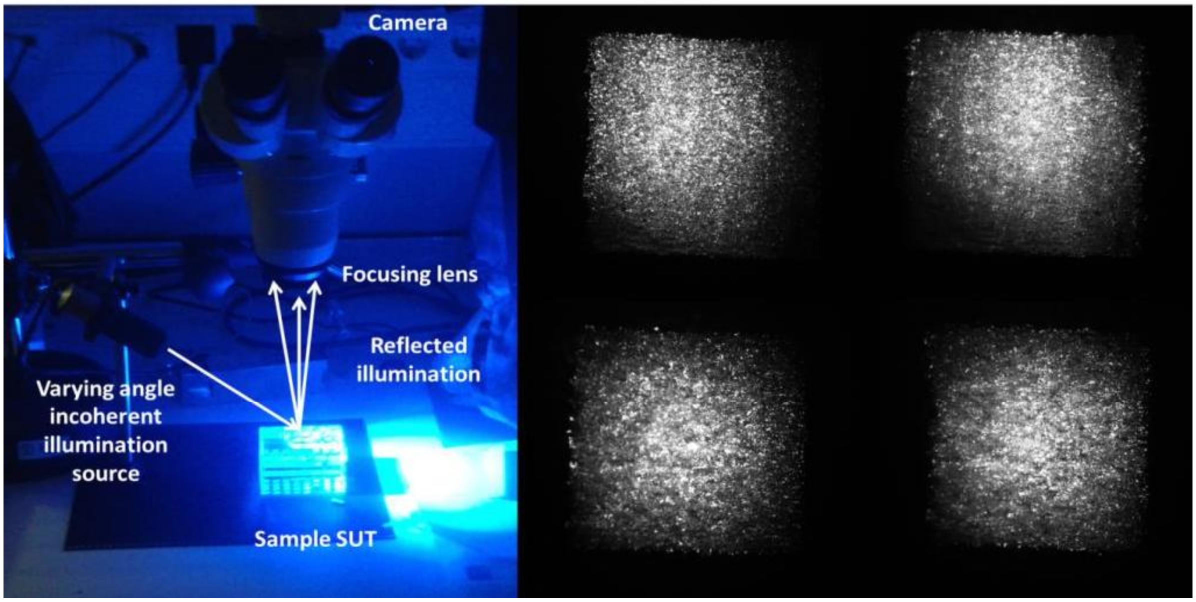

Figure 3. 7 (left) setting with incoherent illumination; and (right) token surfaces.

D. Simulations

At this juncture an interesting task appeared: Up to now, it had been possible to match engraving parameters to optical behavior. Yet, the real motivation was to be able to control the characteristics of pixelation and to confirm that an engraved crystal would be able to guide the light in a controlled manner. In order to do that, an exhaustive and expensive process would be foreseen, where it would be necessary to engrave a pattern, measure its optical features, then measure its pixel features and then fine-tune the engraving parameters for the next pattern.

In order to avoid such laborious and costly process, it was deemed reasonable to attempt to simulate the light propagation process in engraved pixelated crystals. Fortunately, our photometric experiments provided a number of parameters necessary, such as average reflectance and width of engraved surfaces, while the rest could be found in literature [25] or evaluated through equally exhaustive simulations, with the difference that the cost factor would now be minimized.

The procedure intended would be a particle level simulation (figure 3.9), as only in this manner it would be possible to fully understand the light transportation and collection process. It is possible to develop such simulations in-house, but such a process would add an unnecessary risk of result credibility, while being a strenuous and time consuming one. For this type of simulations, GEANT4 [26], a toolkit developed in C++ by a collaboration including the biggest institutes on particle physics in the world, is the golden standard. GEANT4 is a “Monte Carlo” simulator, meaning that some attributes are randomized, providing an estimation of the response on the practically infinite multidimensional space of possible trajectories, energies, particle interactions etc, by only a far more limited amount of truly random cases [27].

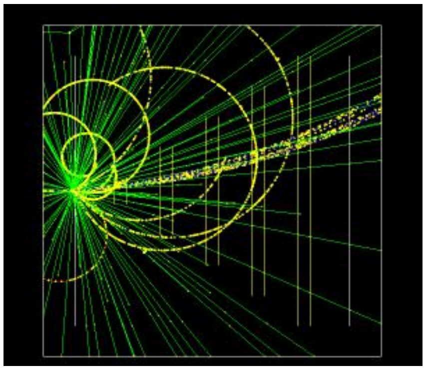
Figure 3. 8 GEANT4 example: Simulated proton 3GeV 1 tesla 10 events superposed

While this toolkit has vast possibilities, it also provides a very developed optical propagation library, inherent from the DETECT 2000 software [28]. Due to complexity reasons, a number of daughter software for simulations of this kind also exist, such as GATE [29] and GAMOS [30], both based on the GEANT4 toolkit. Both were tried, but the last one was found most applicable, due to simplicity of user interface and superior support.

GAMOS is in principle a pseudo-language, where pre-complied objects and functions of GEANT4 are invoked. The user has to build the simulated geometry and provide the characteristics of the materials. In this case, a simple parametrizable design was constructed (figure 3.10), composed of two types of LYSO crystal, one considered standard and the other engraved, drawing its characteristics from the experiments performed. A readout volume, a generic photodetector, was also added. This was a decision that served multiple purposes. Firstly, it is easier to determine the precise characteristics of photodetection at a next stage. Secondly, in this manner it is possible to use the pre-recorded particle photon propagation results for different possible detector configurations. Most importantly, providing an exact model of any photodetector, while adding complexity to the model, would not add any useful characteristics nor would the computing complexity of the routine lower substantially.

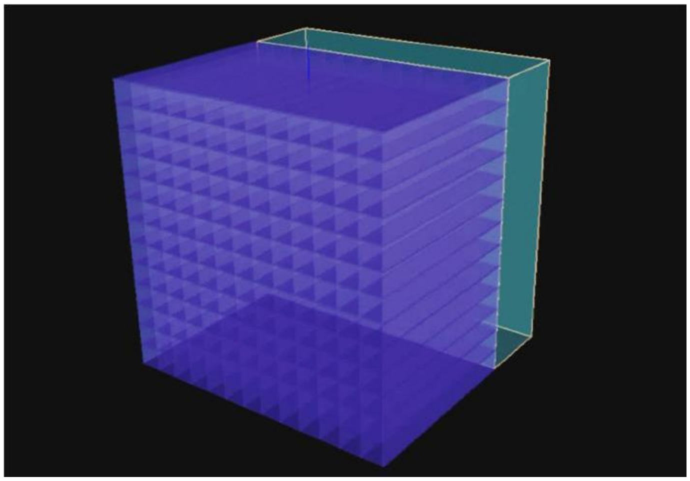
Figure 3. 9 (left) GAMOS generic simulated architecture and simplified diagram of the process

The optical characteristics of the transparent solids themselves, but also of the surfaces where they come in contact with each other had to be refined. This is of paramount importance for optical photon simulations. The dielectric-dielectric rough surface model included in the simulator is the Nayar-Oren model [31]. In this, the surface is considered as a collection of flat micro-size facets with angles with the plain that follow a Gaussian distribution with α standard deviation. An ensuing photon will either be either reflected with a possibility r, or transmitted. If it is reflected, it will either do so in a lambertian (possibility P_L), specular (possibility P_S), or quasi specular (possibility P_{SL}) direction. If transmitted, it would continue in perpetuity, reach the next surface or be absorbed, depending on the absorption length (L_A) defined as a metric of transparency of the materials. The amount of parameters (α, r, P_L, P_S, P_{SL}, L_A) ensures precise modeling of the light behavior. However, this approach also creates a vast multidimensional space that would make the definition for the tens of different surfaces -sets of parameters- we had engraved an impossible feat. Photometric results and estimations provided some (α, ϱ), repeated simulation routines were used to estimate others (P_L, P_S, P_{SL}) within a range of expected values, while some where finally refined after comparing and calculating from real acquisition results at a later stage (L_A).

On a second file, the user has to define the event runtime characteristics of the simulation, as well as what physics should be simulated with higher precision, what results would have to be recorded and an initial random seed for the Monte Carlo process. A source of 511 KeV γ photons is placed at a distance of 15 cm and the photos are directed in a cone at the direction of the scintillator. The scintillation related optical light creation and propagation process take place silently, for reasons of computing complexity, while in the event that any single optical photon crosses the theoretical surface between scintillators and photodetector, energy, time and exact location of crossing are recorded. Photon run files are automatically extracted in binary form from the GAMOS script and analyzed in Matlab (MATLAB 13.1, The MathWorks Inc., Natick, MA, 2013). Scripts developed served both for the extraction of light collection metrics and pixel characterization, as well as for photodetector modeling.

On the photodetector model, for reasons of conformity with the general purpose of our research the 4x4 Hamamatsu MPPC s12642 SiPM (figure 3.15 left) [32] was modeled, being the SiPM foreseen to be used for prototyping. Dimensions, photon detection efficiency information and in later versions also dark rate related noise levels and gain were applied to provide as realistic results as possible. Photons considered detected, from each simulated gamma, were added and averages of location where calculated by the sum of their locations, providing the center of energy of scintillation events. This way a nominal position sensitive readout was also simulated.

It was considered necessary, in order to be able to compare the simulation results with real acquisition results, to follow a characterization process similar to the ones considered for detectors. Guided by standards found in literature [33], first a field-flood diagram (FFD) was calculated. This is the bidimensional histogram of centers of energy of individual events (figure 3.11 left).

From such an image, it is possible to extract profiles, cuts of pixels in X and Y directions. In these profiles, the accumulated events are attributed to different pixels and are expected to follow a Gaussian distribution function, thus Gaussian fitting takes place. Then, it is possible to extract metrics such as the pixel resolvability index, defined as by comparison of the calculated full width at half maximum (FWHM) with the average distance between local and neighboring pixel maxima (PR-equation 3.3), and the peak-to-valley ratio, the ratio between maxima and average of minima per pixel (PVR-equation 3.4). The optical matching between the crystal and the surface of the photodetector was not simulated, providing relatively uniform pixel results. In this context only average PR and PVR were used. An explanatory diagram of the values can be found in figure 3.11 right.

$$PR = \frac{FWHM}{D_{peak}}\ ,\ \text{where } FHWM = 2355\sigma_{gauss},\ D_{peak} = \frac{\sum_{i=2}^{n} l_{max,1} - l_{max,i}}{n} \qquad \text{Equation 3.3}$$

$$PVR = \frac{P_{max}}{\langle P_{min} \rangle}, \qquad \text{Equation 3.4}$$

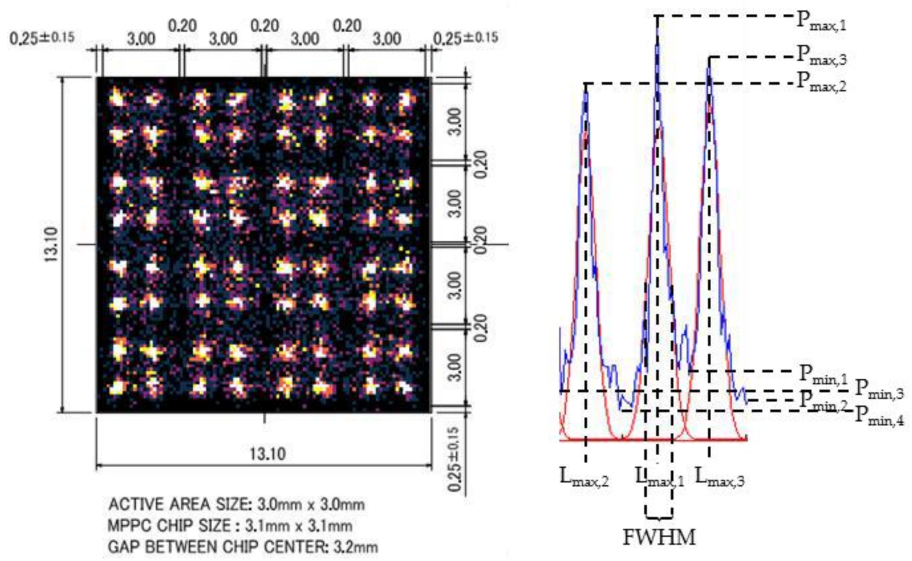

Figure 3. 10 (left) simulated FFD superimposed on the dimensions of SiPM modeled; and (right) brief explanation of the physical context of eq.3.3 and 3.4. Gaussian fit is also visible in red

III. RESULTS

A. *Engraving results*

Pulse energy is partly lost due to the density and high refractive index of the scintillating crystals [20], but for the pulses described, in a cylindrical volume of approximate 10 to 25um radius and 80 to 100um height (figure 3.12), the LIDT is exceeded and a microcrack is created. The final form of the microcrack is dependent on several factors related to laser (laser pulse duration, shape, focusing), crystal (material, type, doping), environment (local temperature) and design circumstances (proximity to neighboring cracks, repetition rate).

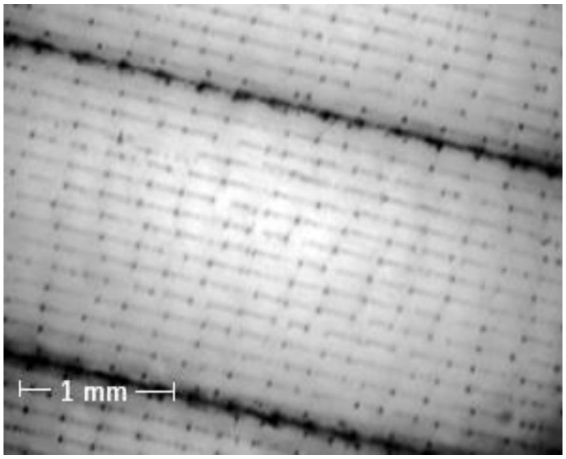

Figure 3. 11 Detail of picture of an initial effort of engraving an LYSO scintillator

The information retrieved provide an estimate for the calculation of individual pulse energy and power through application of equations 3.1 and 3.2:

$$E_{pulse} = \frac{P_{pump}}{f_{repetition}} \Rightarrow \frac{1.2W}{3kHz} = 0.4\ mj < E_{pulse} < \frac{2W}{3kHz} = 0.66\ mj$$

$$P_{pulse} = \frac{E_{pulse}}{t_{pulse}} \Rightarrow \frac{0.4\ mj}{7\ ns} = 57kW < P_{pulse} < \frac{0.66\ mj}{7\ ns} = 94\ kW$$

Equation 3.5

An estimation of microcrack size was also necessary. Without a quantitative figure for the quality of the focusing lens and the precise loss of power that might take place on the lens or within the crystal, an initial estimation takes all laser pulse power at the focal point into account. The dimensions were derived from the microscopic photos (figure 3.12) and the shape from literature on light propagation in such materials [20]. The microcrack was considered to correspond to the area that LIDT is exceeded and was thus modeled as a rod (cylinder), parallel to the light propagation axis, with radius r=~25 um and height l=~90 um. The area of cross section is a function of the material characteristics, while the length depends greatly on the les used. Using these numbers, power density and energy density at focal point were calculated (eq. 3.6):

$$P_{focal} = \frac{P_{pulse}}{A_{focal}} = \frac{57kW - 94kW}{\pi * (25um)^2} \approx 2.8 - 4.7 * 10^9 \, {}^{W}\!/_{cm^2}$$

$$E_{focal} = \frac{E_{pulse}}{A_{focal}} = \frac{400uJ - 666uJ}{\pi * (25um)^2} \approx 20 - 35 \, {}^{J}\!/_{cm^2} \qquad \text{Equation 3.6}$$

Table 3.1: Comparison of pulse characteristics between the procured setting in our lab and the one used at [16].

Specification	STN	Moriya
Pulse duration	~7 ns	10-20 ns
Pulse power	57-100 kW	3.5-7 kW
Pulse energy	400-660 uJ	50-100 uJ
Point distance on xy	100um	50um
Power density (at focal point)	10^9W/cm^2	10^{11}W/cm^2
Energy accumulated (on grid)	20-35 J/cm^2	2-4 J/cm^2
Speed	0.04 mm/s	50 mm/s
Repetition Rate	1KHz	1KHz

These numbers are in general comparable with the ones calculated from [16] and presented in table 3.1. However important differences can be found at the power density at focal point. This was compensated by the strategic decision to proceed with designing less dense microcrack grids.

Furthermore, it was quickly observed that spatial precision of engraving was in the order of few micrometers, while it was already known that the duration of pulses is variable to an extent of 6%, equally amplifying the standard deviation of volume size of engraved points. Another observation is that the microcracks tend to have variable characteristics, a feature that can be attributed to the imperfections of the system, especially relative to the lens. For this purpose, we focused directly on the macroscopic optical behavior of surfaces resulting from controlled engraving of a tridimensional grid of such microcracks. Nevertheless, it was important to try to refine the engraving characteristics that we would apply, such as pulse power and microcrack density.

B. Photometric results

With the application of SPIM it was possible to quantify the quality of different engraving configurations, expressing it as the percentage of the total reflection to the reference measurement, knowing the reflective characteristics of the reflector strip. For this comparison the mean value of reflected light from the illuminated area was used as a surrogate (figure 3.13). This area is visibly uniform in the case of the reference (left), while the SSLE one doesn't demonstrate equally uniform behavior. This can be attributed to the non-continuous nature of SSLE as well as less reflectance observed at the edges of engraved surfaces.

The high quality images produced from this setup provided very valuable information on how the characteristics of engraving affect the reflectivity of surfaces. Firstly, an evaluation of maximum reflectance possible was made, at around 60% of the reflectance of the standard reflector, known to be almost perfect [11]. Above this value the surface would be too thick, exceeding 100 us and uncontrollable cracking of the crystal would be too likely. Secondly, the reflective quality of such surfaces was considered for different wavelengths. The precision of measurement was guaranteed, due to the quality of equipment and professional calibration

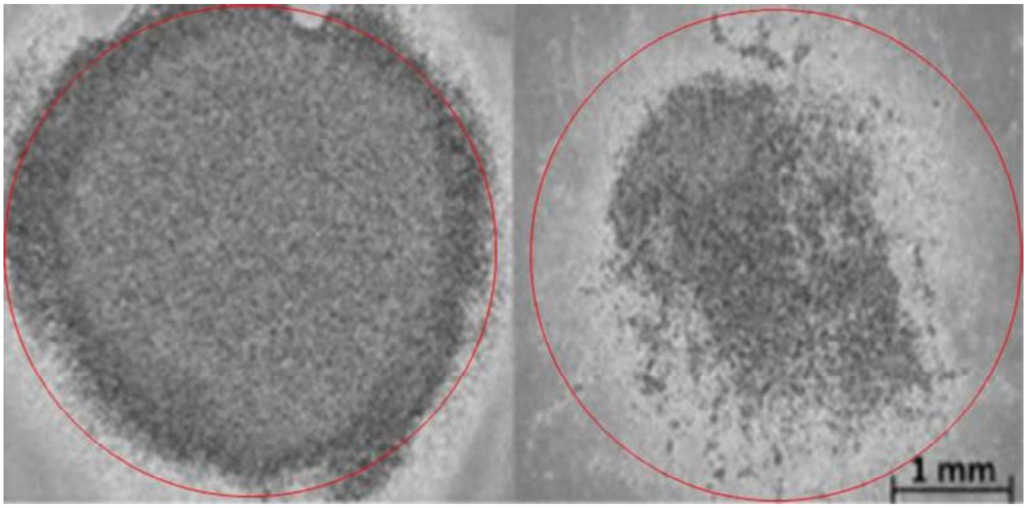

Figure 3. 12 Comparison of engraved surface (right) illuminated at 473 nm to reference reflector (left) from SPIM. The red circle is the area of interest

The simpler photometric setup with incoherent illumination presented in figure 3.8 provided higher flexibility and thus more functionality, even if precision of measurements was not equally guaranteed. It was possible, through microscopic images, to estimate the width of engraved surfaces, ranging between 30 um and 150 um, depending mainly on the engraved energy and density parameters. Also, a photometric sampling measurement routine was performed on a selected few surfaces, to establish the amount of reflectance for different angles (figure 3.14) and thus estimate the type of reflectance. No strong specular element was detected, thus a predominantly diffuse behavior was considered [34].

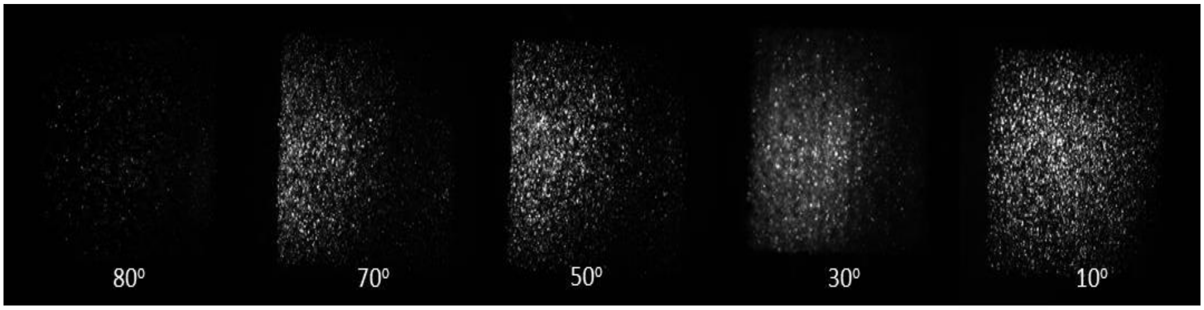

Figure 3. 13 Photometric sampling for different angles between the illumination source and focusing lens.

With the sets of measurements produced by this setup it was possible to quantify and plot the behavior of engraved surfaces for varying power and point density (figure 3.15). On the left, engraving energy was kept stable at a low value for different engravings up to very dense configurations. A direct effect of rising density on reflectance can be observed. On the right, the engraving energy was incremented for two different density configurations. A similar relation can be observed, even though the difference is very small for low and very high engraving energy levels. A routine to measure the absorption of engraved surfaces was also attempted, but the results were inconclusive.

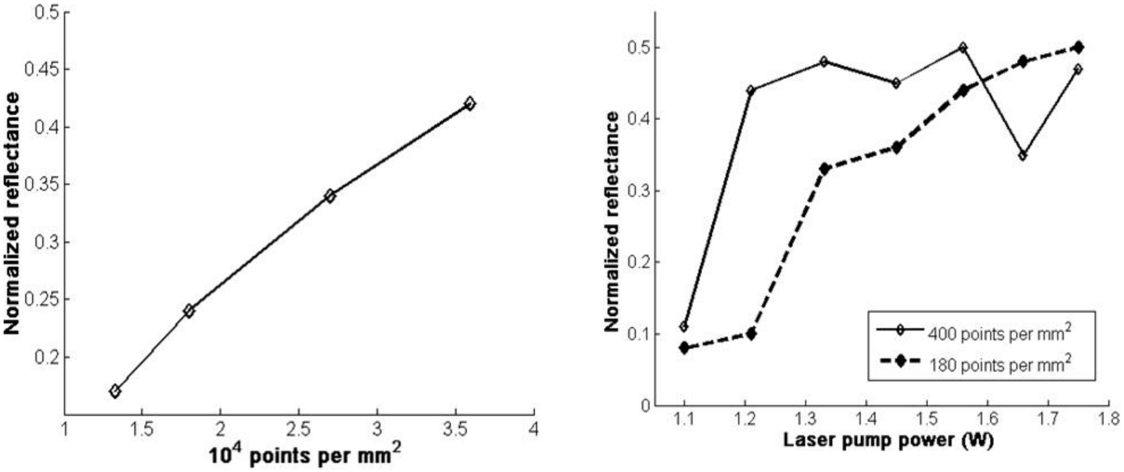

Figure 3. 14 (left) reflectance as a function of grid density of engraved surface; and (right) reflectance as a function of laser pulse power for configurations of 180 and 400 points per mm2.

Those results were very important as it was necessary in order to assess the possibilities that the procured setting could offer. Indeed, it was seen that it is possible not only to create reflective patterns, but furthermore to have nominal control on the optical behavior and dimensions of the surfaces, by controlling the engraving characteristics. Initially it was thought that the maximum reflectance could be further amplified by trying different parameters, such as warming up the crystals before engraving. However, soon it was found out that for all configurations attempted, not only higher reflectance was not possible, but furthermore reflectivity results were not deterministic, large cracks were very likely to appear, rendering the crystal useless and the ensuing walls tended to be very thick, canceling in practice the initial motivation, of attempting to improve the packing fraction. This is compatible with literature on SSLE[36] but also with experience, where even explosion of small crystals was observed at high energies. In this context, next efforts focused on developing a repeatable routine and evaluating whether walls of reflectivity in the order of 30-50% would provide enough light guiding for the production of pixel patterns in monolithic scintillators.

C. Simulations results

With the general outline of the generic parametrizable architecture, a very big amount of variable parameter simulations where executed at a virtual machine. In the various runs of tens of thousands of events each, values of the light transmission variables were tested and refined. The initial approach concerned fine tuning of the general characteristics of the modeling routine through simulation of standard pixelated arrays, in which case not only the characteristics of reflectors are known [35], but also a bulk of measurements was made available for comparison [36]. When this step was performed, estimations for different pixel sizes were made (figure 3.16) and in this way the limitations of the engraved pixels started to be uncovered and understood.

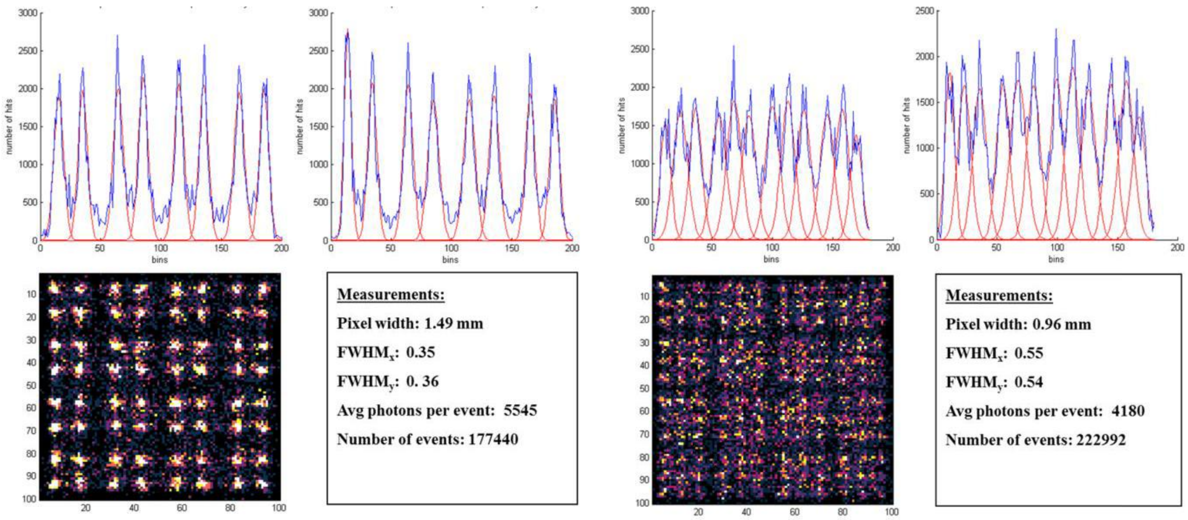

Measurements:
Pixel width: 1.49 mm
FWHM$_x$: 0.35
FWHM$_y$: 0. 36
Avg photons per event: 5545
Number of events: 177440

Measurements:
Pixel width: 0.96 mm
FWHM$_x$: 0.55
FWHM$_y$: 0.54
Avg photons per event: 4180
Number of events: 222992

Figure 3. 15 Simulation results and metrics resulting from simulations for 8x8 (left) and 12x12 (right) pixel configurations on 4x4 Hamamatsu MPPC s12642 SiPM

Collective results from series of simulations were also gathered and plotted (figure 3.17). Thus, it was assessed what could be expected, that less reflective light-guides add an uncertainty on the final center of energy location, perceived through the broadening of pixels and lower PR (3.17 left). An effect on the PVR from light-guide absorption length was also detected (3.17 center). On the other hand, after a number of runs for different values of lambertian-specular reflection components (P_L, P_S, P_{SL} tuples), it was demonstrated that the effect on PR and PVR is minimal (3.17 right).

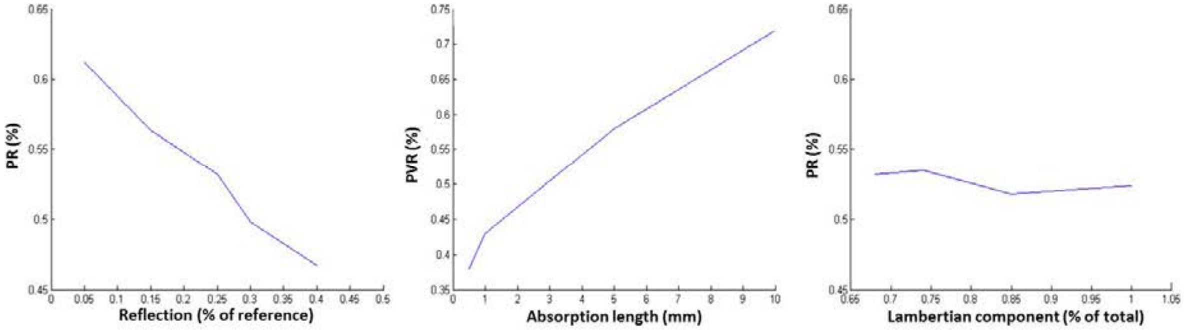

Figure 3. 16 Simulation results: (left) PR versus reflection of engraved surfaces; (center) PVR versus evaluated absorption length; and (right) PR versus lambertian component of reflection model

IV. CONCLUSIONS

With the results from simulations, the preferred solution to the first question occurring in the intention to develop SSLE for scintillators is materializing: To be able to tune pixelation features of a pixelated array in a monolithic scintillator block from the engraving parameters of an SSLE setup.

In the process, we made an evaluation of the necessary features such a setup should have. Only then, after engraving a big number of token surfaces on BK-7 and LYSO, we assessed the reflectivity of dense and relatively sparse designs, developing a photometric system in the process.

In order to estimate how this reflectivity would affect the pixelation resolvability, we developed a complex optical model of these surfaces and included this model in a routine of light propagation simulations. Furthermore, we created an accurate model of an existing SiPM and after estimating light absorption at the detector, applied metrics to understand the results of optical propagation.

A very important conclusion of the feasibility study was the decision taken to not pursue a research direction on intending to create denser and thinner surfaces, a direction closer to material science and manufacturing, than nuclear medicine instrumentation. Indeed, with the application of simulations, we established that semi-transparent light-guides of the range of measured characteristics provide sufficient light guiding for pixels, elemental detector elements, to be resolvable. The focus would be, thus, to demonstrate that this approach provides the desired characteristics in real world acquisitions.

Most importantly, it was possible to answer the question: Indeed, a cost-effective SSLE setup has everything necessary to attempt and succeed in engraving pixeling light-guides under the surface of monolithic scintillators.

V. REFERENCES

[1] Lee, K., Kinahan, P. E., Miyaoka, R. S., Kim, J. S., & Lewellen, T. K. (2004). Impact of system design parameters on image figures of merit for a mouse PET scanner. IEEE transactions on nuclear science, 51(1), 27-33.

[2] Nagarkar, V. V., Gupta, T. K., Miller, S. R., Klugerman, Y., Squillante, M. R., & Entine, G. (1998). Structured CsI (Tl) scintillators for X-ray imaging applications. IEEE transactions on nuclear science, 45(3), 492-496.

[3] Uribe, J., Wong, W. H., Baghaei, H., Farrell, R., Li, H., Aykac, M., ... & Xing, T. (2003). An efficient detector production method for position-sensitive scintillation detector arrays with 98% detector packing fraction. IEEE Transactions on Nuclear Science, 50(5), 1469-1476.

[4] Watanabe, M., Uchida, H., Okada, H., Shimizu, K., Satoh, N., Yoshikawa, E., ... & Tanaka, E. (1992). A high resolution PET for animal studies. IEEE transactions on medical imaging, 11(4), 577-580.

[5] Adams, M. J. (1981). An introduction to optical waveguides (Vol. 14). New York: Wiley.

[6] Schutt, J. B., Arens, J. F., Shai, C. M., & Stromberg, E. (1974). Highly reflecting stable white paint for the detection of ultraviolet and visible radiations. Applied optics, 13(10), 2218-2221.

[7] Moses, W. W., Janecek, M., Spurrier, M. A., Szupryczynski, P., Choong, W. S., Melcher, C. L., & Andreaco, M. (2010). Optimization of a LSO-based detector module for time-of-flight PET. IEEE transactions on nuclear science, 57(3), 1570-1576.

[8] "Teflon ™| Chemours Teflon™ Nonstick Coatings and Additives". www.chemours.com. Retrieved 09.01.2017

[9] http://www.spyeglass.com/downloads/3M-Screens/3M-Vikuiti-Film-Spec-Sheet.pdf, Retrieved 09.01.2017

[10] Patterson, E. M., Shelden, C. E., & Stockton, B. H. (1977). Kubelka-Munk optical properties of a barium sulfate white reflectance standard. Applied optics, 16(3), 729-732.

[11] Janecek, M. (2012). Reflectivity spectra for commonly used reflectors. IEEE Transactions on Nuclear Science, 59(3), 490-497.

[12] http://www.crystals.saint-gobain.com/products/pixellated-arrays, Retrieved 09.01.2017

[13] España, S., Marcinkowski, R., Keereman, V., Vandenberghe, S., & Van Holen, R. (2014). DigiPET: sub-millimeter spatial resolution small-animal PET imaging using thin monolithic scintillators. Physics in medicine and biology, 59(13), 3405.

[14] D. J. Van Der Laan, M. C. Maas, D. R. Schaart, P. Bruyndonckx, S. Léonard and C. W. van Eijk (2006). Using Cramér-Rao theory combined with Monte Carlo simulations for the optimization of monolithic scintillator PET detectors. IEEE transactions on nuclear science, 53(3), 1063-1070.

[15] Olcott, P., Kim, E., Hong, K., Lee, B. J., Grant, A. M., Chang, C. M., ... & Levin, C. S. (2015). Prototype positron emission tomography insert with electro-optical signal transmission for simultaneous operation with MRI. Physics in medicine and biology, 60(9), 3459.

[16] Moriya, T., Fukumitsu, K., Sakai, T., Ohsuka, S., Okamoto, T., Takahashi, H., ... & Yamashita, T. (2009, October). Development of PET detectors using monolithic scintillation crystals processed with sub-surface laser engraving technique. In Nuclear Science Symposium Conference Record (NSS/MIC), 2009 IEEE (pp. 3560-3564). IEEE.

[17] Moriya, T., Fukumitsu, K., Yamashita, T., & Watanabe, M. (2014). Fabrication of Finely Pitched LYSO Arrays Using Subsurface Laser Engraving Technique with Picosecond and Nanosecond Pulse Lasers. IEEE Transactions on Nuclear Science, 61(2), 1032-1038.

[18] http://www.princessglassworld.com/world-of-glass-decoration/sub-surface-laser-engraving. Retrieved 09.01.2017

[19] Wood, R. M. (2003). Laser-induced damage of optical materials. CRC Press.

[20] Exarhos, G. J., Gruzdev, V. E., Menapace, J. A., Ristau, D., & Soileau, M. J. (2010, October). Laser-induced damage in optical materials: 2010. In Society of Photo-Optical Instrumentation Engineers (SPIE) Conference Series (Vol. 7842).

[21] Mao, R., Zhang, L., & Zhu, R. Y. (2010, October). Quality of a 28 cm long LYSO crystal and progress on optical and scintillation properties. In *Nuclear Science Symposium Conference Record (NSS/MIC), 2010 IEEE* (pp. 1030-1034). IEEE..

[22] http://www.stnlaser.com/, Retrieved 09.01.2017

[23] Huisken, J., & Stainier, D. Y. (2009). Selective plane illumination microscopy techniques in developmental biology. Development, 136(12), 1963-1975.

[24] Mao, R., Zhang, L., & Zhu, R. Y. (2008). Emission spectra of LSO and LYSO crystals excited by UV light, x-ray and-ray. IEEE Transactions on Nuclear Science, 55(3), 1759-1766.

[25] C. M. Pepin, P. Bérard, A. L. Perrot, C. Pépin, D. Houde, R. Lecomte, C. L. Melcher and H. Dautet (2004). Properties of LYSO and Recent LSO Scintillators for Phoswich PET Detectors. IEEE Trans. Nucl. Sci., VOL. 51, NO. 3

[26] Agostinelli, S., Allison, J., Amako, K. A., Apostolakis, J., Araujo, H., Arce, P., ... & Behner, F. (2003). GEANT4—a simulation toolkit. Nuclear instruments and methods in physics research section A: Accelerators, Spectrometers, Detectors and Associated Equipment, 506(3), 250-303.

[27] Gentle, J. E. (2006). Random number generation and Monte Carlo methods. Springer Science & Business Media.

[28] WU, G., LIANG, G., LI, J., & QIU, S. (2011). Monte Carlo simulation of photons transport in LYSO crystal. Journal of Shenyang University, 6, 037.

[29] Strulab, D., Santin, G., Lazaro, D., Breton, V., & Morel, C. (2003). GATE (Geant4 Application for Tomographic Emission): a PET/SPECT general-purpose simulation platform. Nuclear Physics B-Proceedings Supplements, 125, 75-79.

[30] Arce, P., Rato, P., Canadas, M., & Lagares, J. I. (2008, October). GAMOS: A Geant4-based easy and flexible framework for nuclear medicine applications. In 2008 IEEE Nuclear Science Symposium Conference Record (pp. 3162-3168). IEEE.

[31] Oren, M., & Nayar, S. K. (1995). Generalization of the Lambertian model and implications for machine vision. International Journal of Computer Vision, 14(3), 227-251.

[32] Hamamatsu MPPC TSV reference sheet, http://www.nuclear.gla.ac.uk/~jrma/A2/Tagger/NewFPD/SiPMT/KSX-I50014-E_S12642%20Series%20(3mm%E2%96%A1-TSV%E3%83%BCArray).pdf, retrieved 11.01.2017

[33] Thompson, C. J., Goertzen, A. L., Kozlowski, P., Retière, F., Stortz, G., Sossi, V., & Zhang, X. (2012, October). Evaluation of very highly pixellated crystal blocks with SiPM readout as candidates for PET/MR detectors in a small animal PET insert. In Nuclear Science Symposium and Medical Imaging Conference (NSS/MIC), 2012 IEEE (pp. 3141-3145). IEEE.

[34] Scott M. Juds (1988). Photoelectric sensors and controls: selection and application. CRC Press. p. 29. ISBN 978-0-8247-7886-6.

[35] Janecek, M., & Moses, W. W. (2010). Simulating scintillator light collection using measured optical reflectance. IEEE Transactions on Nuclear Science, 57(3), 964-970.

[36] Schaffer, C. B., Brodeur, A., & Mazur, E. (2001). Laser-induced breakdown and damage in bulk transparent materials induced by tightly focused femtosecond laser pulses. Measurement Science and Technology, 12(11), 1784.

Chapter 4: Verification of Sub-Surface Laser Engraving for scintillators

I. INTRODUCTION

Having solved the recursive stand-off -described in the previous chapter- of relating engraving parameters of a sub-surface laser engraving (SSLE) setup to pixel characteristics of the final engraved monolithic array through analyzing the macroscopic optical behavior of the engraved surfaces, it was time to evaluate our results. The feasibility study, as well as some initial LYSO engraving, for the shake of measurements and proof of concept provided evidence of our approach advantages. However, the semi-transparent light-guiding technique needs further results analysis and quantification of its benefits and limitations, as compared to standard pixelated arrays and published works [1,2], in order to justify our effort.

Moreover, it would be important to confirm that the energy resolution of these scintillators wouldn't be compromised by the SSLE process and quantify the effect, since the energy measurement is vital for discrimination of events. Also, information on energy resolution as well as rate of events could provide very important insight on the nature not only of the engraved pixelated arrays, but also the engraved surfaces themselves.

On the other hand, it is important to be able to evaluate the simulation results, as compared to real acquisitions of scintillators engraved with same topologies. In this manner, the simulation suite can be fine-tuned and further used for the next steps that would go towards expanding the applications of SSLE on scintillators.

II. MATERIALS AND METHODS

A. Experimental setup

Because of the reasons detailed in the previous section, the next steps comprised of engraving various architectures of pixelated arrays in monolithic scintillator crystals, guided from the simulation results, and proceeding to measuring them, using a photomultiplier system. The system of choice was a read out element of the Argus detector, being a well-tested and documented setting developed in our lab [3]. This front-end (figure 4.1) houses a position-sensitive PMT (Hamamatsu R5900U-00-C8), high voltage distribution and control, charge multiplexing network and amplification stages. Digitalization and readout was performed using initially a customized USB-based system (Bitwise systems, 5272 Hollister Ave, Goleta, CA 93111) and later-on a 16 channel 125 MHz PicoDigitizer Nutaq system (Nutaq Innovations, Quebec City, Quebec, Canada). Data from both systems are analyzed and plotted through scripts developed in Matlab.

Figure 4.1 Argus detector element with a scintillator mounted on the PMT (right)

In order to achieve optimal optical matching between the surface of the crystal and that of the PMT a process had to be followed. Initially, any engraved crystal has to be cleaned with alcohol and wrapped in reflective tape (Teflon [4]). Then, optical grease (compound V-788, n=1.47, Visilox Systems, Troy, New York) is applied. This has two purposes. Firstly, in this manner the possibility of air interfaces that would distort the propagation of light is avoided. Secondly, the matching refractive index of the grease between the PMT protective glass and the LYSO, the photon transmission is is optimized. Finally, the crystal and PMT are wrapped in black opaque film. This is intended not only to mechanically stabilize the placement of the scintillator, but also to avoid external light pollution, given that the PMT practically has single photon sensitivity.

In order to acquire comprehensive results, the application of an external β+ is necessary. Natural radiation from the environment, as well as the intrinsic radiation of Lutetium [5] is available. However, these provide a very small number of counts per second, while not allowing evaluation of the quality of energy conversion of the scintillator detector, in the lack of clearly distinguishable peaks. Using external β+ sources is thus necessary, but also necessarily performed following a number of precautions and in a special designated areas due to radiation protection concerns. There are some available low activity β+ emitters used as test sources for positron emission detector technology, such as ^{22}Na and ^{68}Ge. We used the first as the most common, as in this manner it was possible to compare the energy spectrum with references in the literature (figure 4.4) and extract equally comparable metrics. Furthermore, in this manner the statistics gathered are enough and at such rate as to allow multiple acquisitions to take place daily.

In principle, the way to confirm the quality of energy conversion of the gamma detector prototype is perform a gamma spectroscopy experiment for every change on the crystal setup, or every different configuration. The quality is quantified by the full width at half maximum (FWHM) of the β+ corresponding peak, at 511KeV, usually calculated through Gaussian fitting [6].

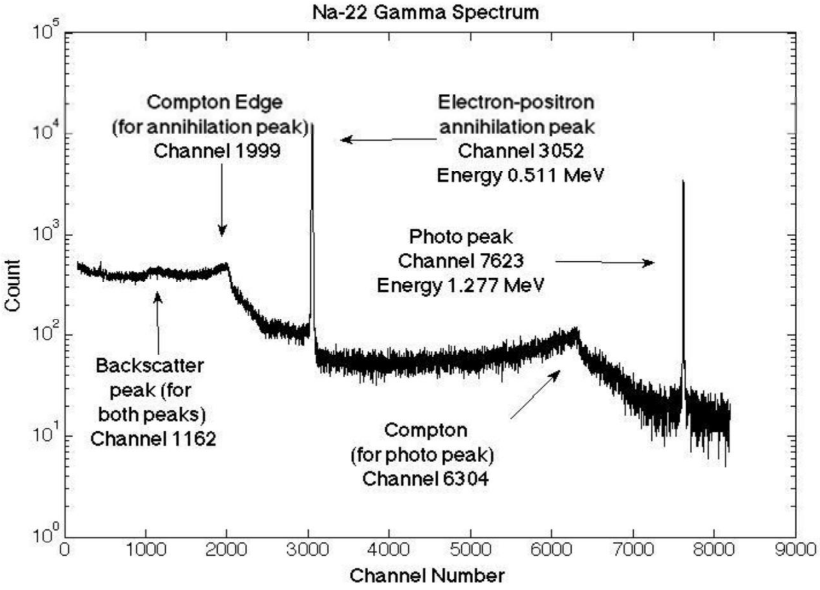

Figure 4.2 Sodium-22 spectrum in logarithmic scale. Clearly distinguishable peaks make detector characterization easier [7]

B. Design verification

Initially, several designs of square pixels where developed. These where used to establish the development technique, extract information on pixel size and design characteristics, but also to verify and fine-tune the simulation routine. Not only were the models applied to be confirmed, but also insight on characteristics of the surfaces required to expand. These designs included applying SSLE to various scintillator crystals, to assess repeatability and reproducibility of the process.

A pixel pitch of 1.6x1.6 mm^2 was chosen as a conservative attempt, for a first attempt on engraving a LYSO scintillator with the customized SSLE setup. The crystal depth is 8mm.

The SSLE pixelated array, presented in figure 4.3 (left) were used as a proof of concept on the possibility of developing a cost-effective, fast and repeatable routine for the application of SSLE techniques on scintillator crystals in-house.

While the microcrack form had already been imaged and analyzed, it was necessary to also acquire a figure on the effective size. Through experience it was elected to use standard pulse energy for most designs, corresponding to around 1.85 W of the laser diode pump. It was necessary, however, to estimate the maximum threshold of laser energy before uncontrollable cracking commenced. For these reasons, a very dense matrix was designed, with 4.22×10^5 points of high energy, in a volume of 12.8x12.8x12 mm^3 (figure 4.3 right), approximately 220 points per mm^2. The idea behind it was to be able to detect a difference in acquisitions before and after engraving. Discrepancy in rate, given same experimental conditions such as distance of radioactive source, optical coupling and detector gain, would demonstrate directly the deterioration of packing fraction, as compared to the non-engraved configuration. Difference in energy spectrums would demonstrate the level of absorption of the SSLE reflective patterns.

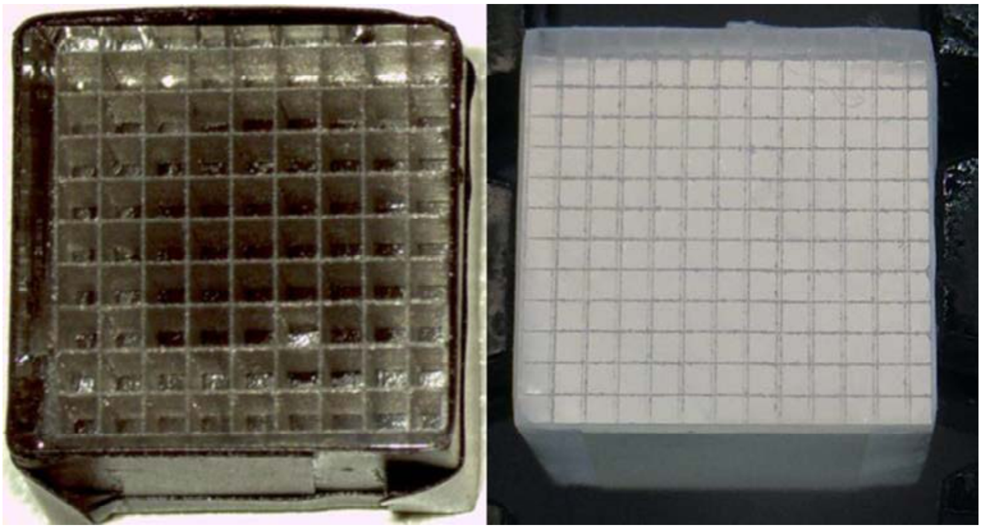

Figure 4.3 (left) an initial sparse SSLE LYSO design; and (right) a very dense engraved array with 1x1 mm^2 pixel size. The images are in scale.

Moreover, to be able to quantify the spatial resolution of SSLE scintillators, a comparison study of an engraved and a standard pixelated array was necessary. The crystals we engraved are of size 12.8x12.8x6 mm^3 and are engraved in a design of 100 square pixels. For comparison, we also used a standard matrix of 13x13 pixels of 1.4x1.4x7 mm^3 pixels as a reference to the known golden standard.

In the process of this testing and fine-tuning, effects not initially expected were observed. For instance, it was not foreseen that the application of an external commercial reflector (Teflon) would interact with the semi-transparent SSLE surfaces, affecting the light propagation inside the crystal. Indeed, an easily observable result was that the field-flood diagram FFD of SSLE monolithic crystal would shrink, as compared to an equal size standard pixelated array. This was feared to compromise spatial resolution results. A test for this effect was performed, with the application of black tape directly on the crystal surface which would correspond to an almost perfectly absorptive means. Calculations, new simulation approaches and a new model for semi-transparent pixels had to be developed to estimate these effects.

Considering first the traditional pixelated array where opaque reflective separators are used, we can theorize that the produced scintillation photons are kept within the pixel area (figure 4.4.A). On the other hand, when, for SSLE, it is known from photometric experimental routines and simulations that a percentage of the total number of photons produced traverses the separators (figure 4.4.B). Thus, apart from photons (figure 4.4.C), which follow the traditional distribution (L_1), seeing opaque walls, we can consider a second light field L_2 (figure 4.4.D) which escapes the pixel. For photons of the L_2 group the SSLE walls are as if non-existent.

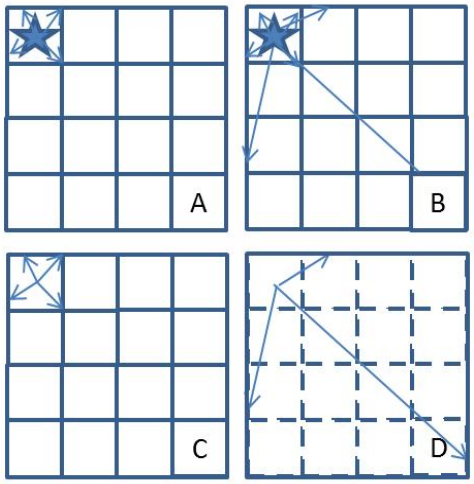

Figure 4.4 Semi-transparent light-guide model: (A) standard light-guide; (B) semi-transparent; (C) L_1 photons; and (D) L_2 photons

The amount of detected energy corresponds roughly to number of photons since those are within a concise range of energies and the photometric experiment over this range didn't demonstrate differences in transmission. In other words, the multitude of photons of L_1 and L_2 corresponds to the percentage of light reflected or transmitted in macroscopic level, respectively. The center of energy for L_1 is at the center of corresponding pixel due to internal symmetry. For the same reason, the one for L_2 lies at the center of the crystal. Thus, the center of energy is, in this case, the combination of the energy mean of L_1 and L_2, weighted by the known SSLE wall transparency.

III. RESULTS

A. *First engravings of scintillators*

Since experience with the engraving setup was still limited, as apart from few LYSO attempts, the main photometric effort took place with the application of BK-7 glasses, it was deemed reasonable to begin working with less costly scintillators already found in our lab. Big GSO and BGO crystal blocks from previous PET systems, of dimensions 6x20x30 mm^3 proved very useful, especially since their material features differ greatly.

In this manner, it was possible to evaluate that our system could overcome limitations found in literature [1], as we managed to engrave 30 mm deep scintillators. Moreover, very interesting insight was gained on the SSLE behavior that oxyorthosilicate based scintillators demonstrate as compared to other types of crystals (figure 4.5). It is possible to assess the visible difference in characteristics of engraved surfaces, as in the case of BGO highly absorptive (black) walls were created. Even though the mechanism seems to be same like BK-7 glass, where the crystal melts through plasma creation [8] due to heat accumulation, this feature was only observed with BGO.

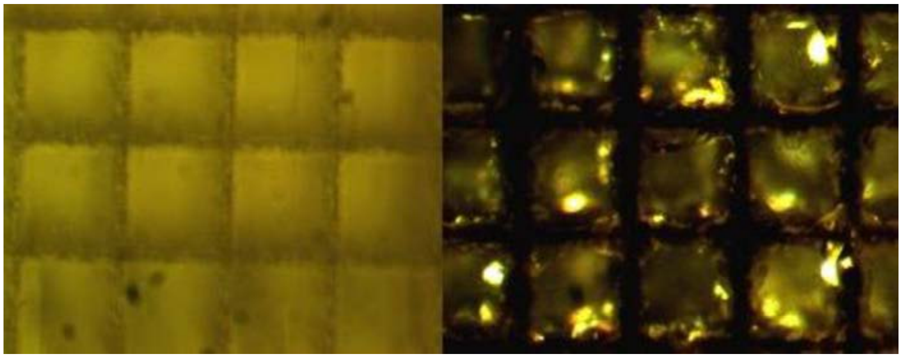

Figure 4. 5 Engraved arrays of 1.6x1.6 mm^2 pixels on GSO (left) and BGO (right).

An estimation of the LIDT for the Nd:YAG laser with frequency split at 532 nm, that we used, was also performed. By applying the equations 3.1 and 3.2, a formula for this estimation is constructed on equation 4.1. In this formula, the minimum laser power that was found to be necessary for engraving as well as the dimensions of microcracks as measured with microscopic images are used (table 4.1). A relation to the melting point was observed, even though the cracking mechanism is known to be related to non-linear ionization mechanisms and thus the band gap of respective materials, not their melting point [8].

$$LIDT = \frac{P_{LD}}{f_{rep} \times \pi \times r_{microcrack}^2} \qquad \text{Equation 4.1}$$

Table 4.1: Engraved materials and LIDT

Material	Melting point (C^o)	Laser power (W)	Average microcrack radius (um)	LIDT(J/cm^2)
BK-7	557	1.15	25	184
BGO	1050	1.35	25	216
GSO	1900	1.65	15	733
LYSO	2047	1.8	15	800

B. Spatial resolution results

Corresponding to the array of figure 4.3 left, in figure 4.6 the first results of acquisition of a SSLE pixelated crystal with a sodium source are presented. Conditions of the acquisition were not ideal. The source was placed very close to the scintillator, as can be derived by the asymmetry in activity between central and external pixels distinguishable mainly in the X profile. Furthermore, the analog and digital offsets of read-out channels were not corrected giving the feeling of perspective depth in the FFD. However, those results demonstrate distinguishable pixels for a very sparse array, with calculated reflectivity of light guides around 25%.

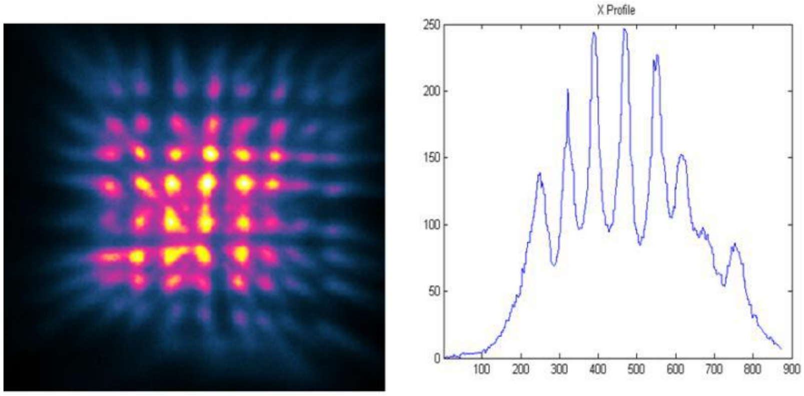

Figure 4. 6 (left) Field-flood diagram (FFD) and (right) a token central X profile of the first LYSO crystal engraved with our SSLE setup

More engraved crystals were acquired in the same setup and the results used to fine-tune the simulation process. Indeed, it was found out that the surface model was accurate enough to be used as a tool to guide the engraving characteristics of the more complex topologies intended. The metrics retrieved from simulations were compared with those of real acquisition for a pixel grid of 1.2x1.2x12 mm^3 volume and 32% calculated reflectivity (figure 4.7, table 4.2).

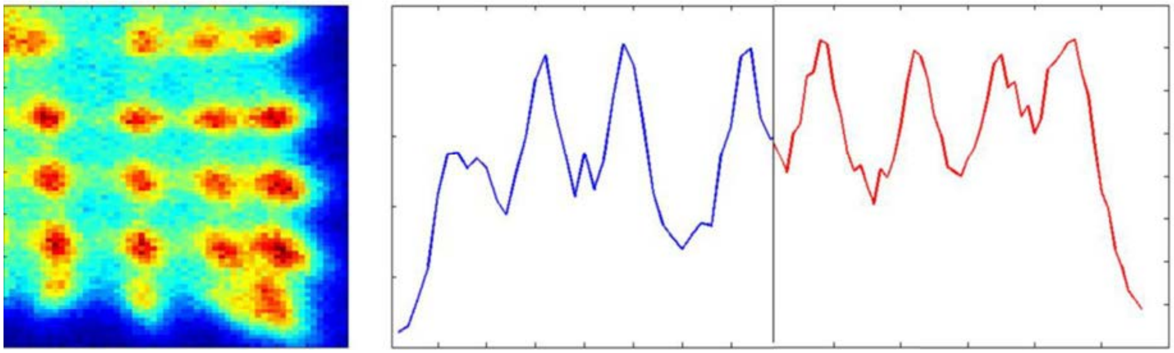

Figure 4. 7 (Left) detail of a 35% calculated reflectivity engraved LYSO; and (right) comparison of simulation (blue) with acquisition (red) pixel detail

Table 4.2: Comparison of metrics of simulation and acquisition

#	Pixel resolvability	Peak to valley ratio
Simulated	0.43	0.46
Engraved	0.4	0.44
Difference (%)	7.5	4.6

Images of a SSLE monolithic LYSO crystal were acquired and presented it figure 4.8, along with an image from a standard pixelated LYSO. In the same figure a comparison of profiles is also possible. In order to evaluate the pixel resolvability of both cases we fit each pixel with a Gaussian and receive the standard deviation which corresponds to the full width at half maximum (FWHM), presented in table 4.3 for both cases, and averages at 0.56 mm for the SSLE crystal and at 0.42 for the standard pixelated array. By dividing this with the corresponding pixel width, we measure the pixel resolvability. The relatively broader distribution of results ranging from 0.3 to more than double can be attributed to the effect of the external reflector which, being of higher reflective quality than the engraved surfaces directs a disproportionate amount of light towards the center. This effect is more expressed in the case of external pixels. While the SSLE array has visibly worse PI and PVR, quantification of results demonstrate that pixels are still quite resolvable, meaning that events can be directly attributed to a volume of the scintillator, confirming the viability of the technique.

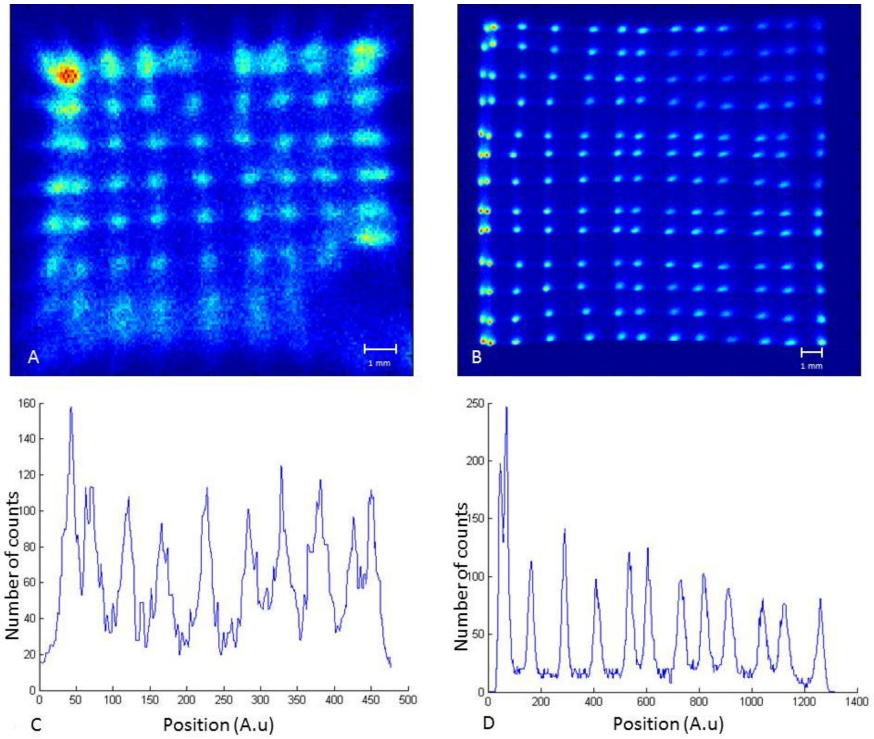

Figure 4. 8 (A) SSLE scintillator FFD; (B) Standard pixelated array FFD; (C) SSLE scintillator profile; and (D) Standard pixelated array profile. An estimation of scaling of position measurement is given in the FFD

Table 4.3 Comparison of spatial resolution characteristics between engraved and standard scintillator.

	FWHM (min, mm)	FWHM (max, mm)	FWHM (average, mm)	P.I. (average, %)
SSLE	0.38	0.74	0.56	44
Standard	0.32	0.59	0.42	31

C. Energy Results

For pixelated arrays, it has been detected that individual pixels have distinct energy spectrums. This can be attributed to different conditions, as even if the pixels belong to the same crystal growth, they have individual reflector fitting and optical coupling in all six surfaces. This was the initial intention for the SSLE array. However, after aleatory testing it was found out that due to the semi-transparent nature of the SSLE walls but most importantly, due to the lack of surface interfacing scintillators to reflectors, requiring optical matching, like with external reflectors within the array, energy spectrum was uniform throughout the volume.

In figure 4.9 the energy spectrum of a ^{22}Na source is presented. The spectrum of the full array demonstrates a clearly distinguishable peak at 511 keV, with FWHM corresponding to 14.4%. This is an improvement of 30% over the average energy resolution reported with the same photodetector [3]. The secondary peak at 1277 keV was detected at 1275 keV, demonstrating alinearity of the system of less than 0.2%. It could be commented that this spectrum quality allows precise thresholding for annihilation events and spatial uniformity simplifies that process.

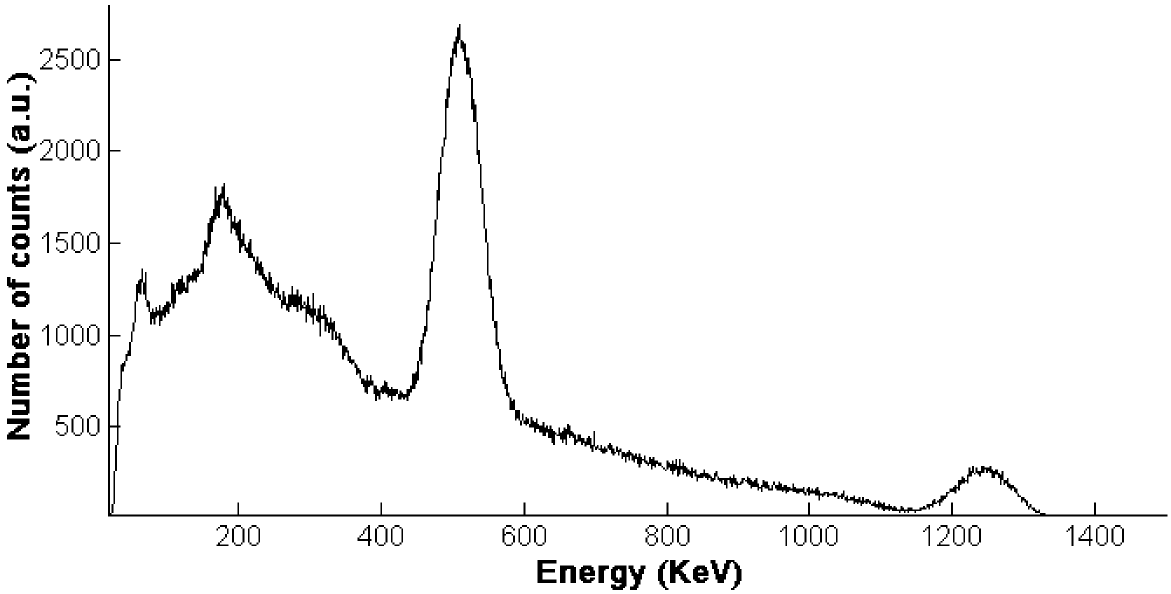

Figure 4.9 ^{22}Na spectrum from SSLE LYSO array

D. External reflector study

It was briefly mentioned that the interaction of light with the perimetral reflector caused image aberrations. From the test with absorptive external reflector conflicting results were acquired. While the size of FFD would stretch almost to the expected dimensions, energy resolution was gravely distorted (figure 4.10). The model based on two groupings of photons was evaluated. From this simplified model, it was possible to create a correction matrix and expand the FFD accordingly. Spatial resolution of the detector doesn't seem to be affected by this shift in position of center of energy of event, as the metrics considered, such as PR, are relative to the size of the image.

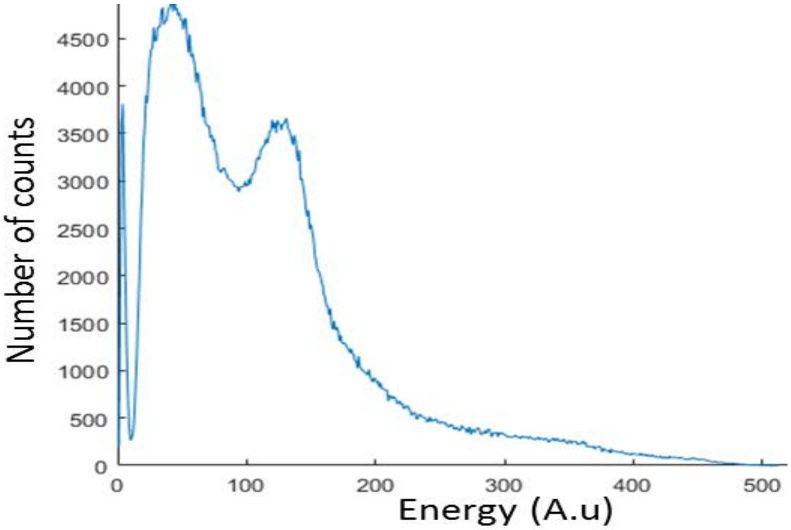

Figure 4.10 Energy spectrum of a ^{22}Na source for SSLE with absorptive external wrap. The 511 KeV is barely visible.

Yet, this is a simplification of the model, because in principle the L_2 group corresponds to all the photons that traverse through one or more SSLE walls, without considering the difference between those that traverse through one, two or all. This phenomenon was only possible to quantify through a recursive numerical simulation of light propagation routine, in Matlab. In figure 4.11 a matrix can be found for a 10x10 pixel distribution with 40% reflective light-guides. The bar represents the amount of light reflected at the external reflector, assumed perfect. Considering that this amount represents a shift towards the center, at the FFD, it is possible to reverse this phenomenon.

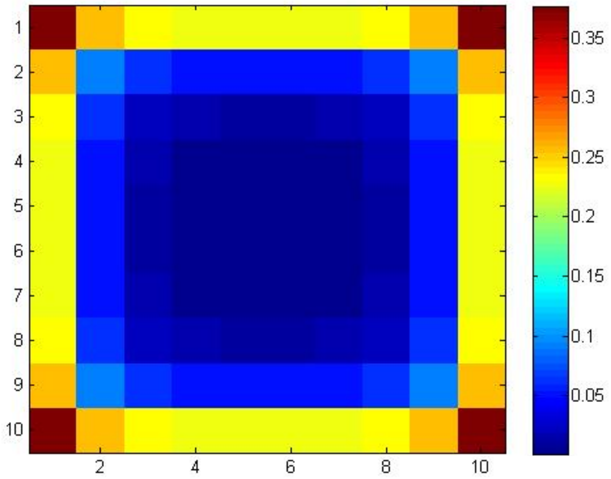

Figure 4.11 Simulation results for the position-dependent amount of light reflected on the external reflector for a representative 10x10 square SSLE engraved array with 0.4 reflective walls

E. *Quantification of detector characteristics*

From acquisition of the very dense SSLE configuration of figure 4.3 lower rate of events and difference in energy spectrums were detected. This lower rate, around 5%, is attributed directly to an equal percentage of volume of the scintillator having lost its scintillating properties. This volume was calculated and divided by the known number of engraved points. Through this calculation it was made clear that apart from the visible part of a microcrack, a volume around it is also destroyed. In this context, a value for maximum effective microcrack size in LYSO was found to be approximately 19×10^{-5} mm^3, compared to approximately 11×10^{-5} mm^3 measured through observation. From matching the engraved surfaces geometry with the non-scintillating volume calculated above, the maximum average effective thickness of engraved walls was found to be 21 μm. These measures can be extrapolated for the crack size of lower energy values.

Energy spectra also revealed a slight discrepancy. As demonstrated in figure 4.12, the FWHM is measured at 8.13% for the monolithic scintillator. Deterioration of 6.3% for the engraved matrix gives a measure of the uncertainty added in the energy measurement by engraving. It is noteworthy that the spectrum of this very dense engraving configuration is slightly deteriorated as compared to the one depicted in figure 4.9. Nevertheless, this is still better than the pixelated array.

Furthermore, the 511keV maximum is displaced by 4% before and after engraving. This number corresponds to the average light lost per event. For an approximate 45% calculated reflectance of the engraved pattern, the average engraved material traversed by a photon is approximately 20um. This number results as the product of the average number of surfaces crossed, estimated by the recursive simulation mentioned before, and the calculated effective thickness of the engraved walls (21 μm). In this manner, the light lost by this transversal corresponds to absorption length of SSLE walls for optical photons, calculated at approximately 0.49mm, by extrapolation of the exponential equation of light absorption.

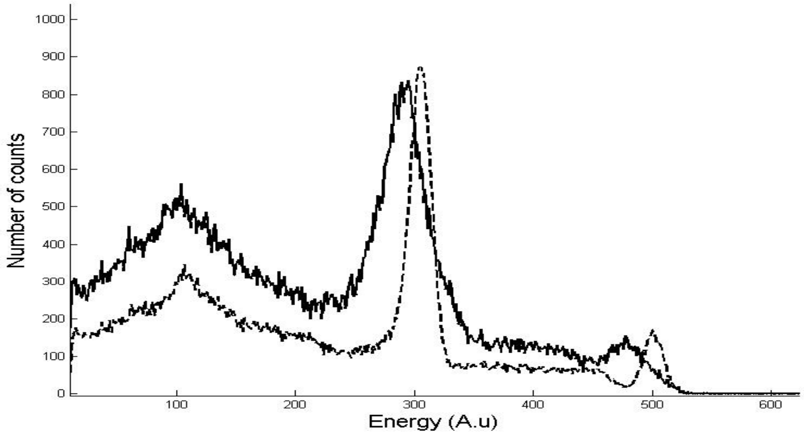

Figure 4. 12 Monolithic (dashed) and engraved crystal spectrum of a ^{22}Na source

The exact percentage of total microcrack volume depends on the configuration of engraving, however using the estimated effective microcrack size for the common energy in application, closer to the laser induced damage threshold, a theoretical calculation for the packing fraction was conducted. For the presented design, a configuration of reflective patterns with microcrack engraving power around 65kW and an 81 microcracks/mm^2 density of surface was used. Using the measured size and shape of microcracks, we calculate the average volume at 9.75×10^{-5} mm^3. For the crystal presented, of dimensions 12.8×12.8×6 mm^3 and volume 983.04 mm^3 the amount of microcracks was 1.12×10^5 and thus the total disrupted and non-scintillating volume is 10.92 mm^3. The packing fraction of our detector is, thus, 98.89%. An equivalent standard pixelated array would have, with pixel area of 1.4 mm^2 and reflector thickness 80um, a packing fraction of ~85.5%.

IV. DISCUSSION-CONCLUSIONS

Comparison of pulses between SSLE arrays and conventional ones demonstrate better light yield for SSLE. A reason for this could be the absence of plastic reflectors between the pixels, where imperfect of optical matching creates conditions for photon loss. This is a desired characteristic, as it gives more light for pulses of the same energy leading to faster rising edge that improves event timing estimation, a characteristic of paramount importance for PET applications. Moreover, crystal length has a detrimental effect on timing [7]. Higher sensitivity through superior packing fraction allows for shorter crystals to be applied, equally improving the timing behavior of the system.

Valuable experience was gained through numerous engraving designs and attempts, as well as knowledge on laser manufacturing for different scintillators and information on their nature, such as their LIDT. GSO and BGO crystals where also engraved, as cost-effective possibilities.

From information provided by different LYSO providers, the cost for a monolithic block is as low as one third of the cost of the corresponding pixelated array, depending on pixel dimensions. In addition, the higher sensitivity of the SSLE crystal as discussed, allows shorter crystals to be applied. In this context, SSLE pixelated crystals can be procured at a cost as low as one fifth of an equivalent standard array.

Controlled light-sharing can be achieved through precise manipulation of the optical characteristics of the engraved surfaces, limiting the necessity for independent light-guides between the scintillating material and the photodiode, allowing further miniaturization of gamma detectors.

The flexible nature, cost effectiveness and easiness of preparation of the SSLE crystals, along with the superior packing fraction compensate for the slightly superior spatial resolution shown by a standard pixelated array. Further experimentation on different engraving conditions is undertaken. Nevertheless, the study and quantification of characteristics of SSLE pixelation process in monolithic scintillators demonstrated that this can be a very advantageous alternative, being a dichotomy of existing approaches. Merits of standard pixelated arrays, such as ease of readout and good spatial resolution are retained while features of detectors based on monolithic scintillators such as superior packing fraction and ease of application coexist in a cost-effective and unprecedentedly flexible technology, especially applicable to small sized designs, such as MR compatible PET inserts.

V. REFERENCES

[1] Moriya, T., Fukumitsu, K., Sakai, T., Ohsuka, S., Okamoto, T., Takahashi, H., ... & Yamashita, T. (2009, October). Development of PET detectors using monolithic scintillation crystals processed with sub-surface laser engraving technique. In Nuclear Science Symposium Conference Record (NSS/MIC), 2009 IEEE (pp. 3560-3564). IEEE.

[2] Panetta, J., Surti, S., Singh, B., Nagarkar, V., Miller, S., & Karp, J. (2015). Impact of laser induced optical barriers on spatial resolution in thick continuous detectors for PET. Journal of Nuclear Medicine, 56(supplement 3), 604-604.

[3] Vaquero, J. J., Seidel, J., Siegel, S., Gandler, W. R., & Green, M. V. (1998). Performance characteristics of a compact position-sensitive LSO detector module. IEEE Transactions on Medical Imaging, 17(6), 967-978.

[4] "Teflon ™| Chemours Teflon™ Nonstick Coatings and Additives". www.chemours.com. Retrieved 09.01.2017

[5] Wei, Q. (2015). Intrinsic Radiation in Lutetium Based PET Detector: Advantages and Disadvantages. arXiv preprint arXiv:1501.05372.

[6] Shao, Y., Silverman, R. W., Farrell, R., Cirignano, L., Grazioso, R., Shah, K. S., ... & Cherry, S. R. (2000). Design studies of a high resolution PET detector using APD arrays. IEEE Transactions on Nuclear Science, 47(3), 1051-1057.

[7] https://lexieslogofphysics.wordpress.com/2013/02/18/experiment-1-high-resolution-gamma-spectroscopy/, retrieved 20.02.2017

[8] Schaffer, C. B., Brodeur, A., & Mazur, E. (2001). Laser-induced breakdown and damage in bulk transparent materials induced by tightly focused femtosecond laser pulses. Measurement Science and Technology, 12(11), 1784.

[9] Gundacker, S., Knapitsch, A., Auffray, E., Jarron, P., Meyer, T., & Lecoq, P. (2014). Time resolution deterioration with increasing crystal length in a TOF-PET system. Nuclear Instruments and Methods in Physics Research Section A: Accelerators, Spectrometers, Detectors and Associated Equipment, 737, 92-100.

Chapter 5: Non-square designs and depth of interaction by Sub-Surface Laser Engraving for scintillators

I. INTRODUCTION

Apart from the superior packing fraction, sub-surface laser engraving (SSLE) for scintillator crystals is expected to provide unprecedented flexibility in the design of pixelated arrays. Moreover, through the steps described in the previous chapters, a routine on evaluating, simulating, developing, engraving and testing SSLE scintillators has been developed. To be able to answer whether such process can be standardized and applied in prototype but also application development, all the above remain to be proven.

Another aspect of interest is that distinct pixel topologies are costly and difficult to produce, because factory standards are too tightly focused on square prisms for pixelation. Naturally, this can be a first goal not only for demonstration and benchmarking of flexibility, but also for evaluation of such exotic pixelation topologies. It has been proven, for instance, that a bidimensional Eucledian space is optimally packed in hexagons [1]. For this reason, application of such architecture directly enhances spatial resolution. Also, if different shapes would benefit the light-guiding quality of pixels, non-square grids can also promote this quest. From literature on optical waveguiding [2], this is indeed the case.

However, most useful product of the unprecedented flexibility gained is the foreseen possibility of creating depth of interaction (DoI) patterns. While if single photon detection is possible (figure 5.1) it is easier to estimate the depth of interaction due to differences in shape of the illumination “blob” [3], for multiplexed designs it becomes increasingly challenging.

The function of DoI as the ultimate compromise between resolution and sensitivity has also been discussed in previous chapters; moreover, for small size designs like the inserts under discussion, DoI becomes even more fundamental. The expansion of field of view (FoV) closer to the detectors, as compared to the radius of the PET ring, magnifies the parallax error distortion. Simulation of the architecture [4] is a necessary step to demonstrate what is the maximum required number of DoI levels. The smaller the design, though, the more DoI is needed.

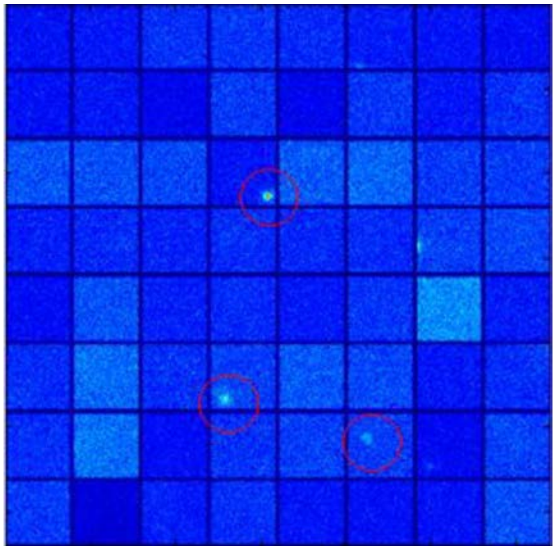

Figure 5.1 Superimposed single photon collection of simulated events. DoI is detectable (red circles) on single photon detection.

Apart from avoiding the parallax error, there is a second feature that makes DoI desirable. As can be understood by looking in detail the figure 5.2, the elemental detector is now smaller. This means that more lines of response (LoR) can be attributed to each element, making the reconstruction process more precise, albeit more computationally intensive.

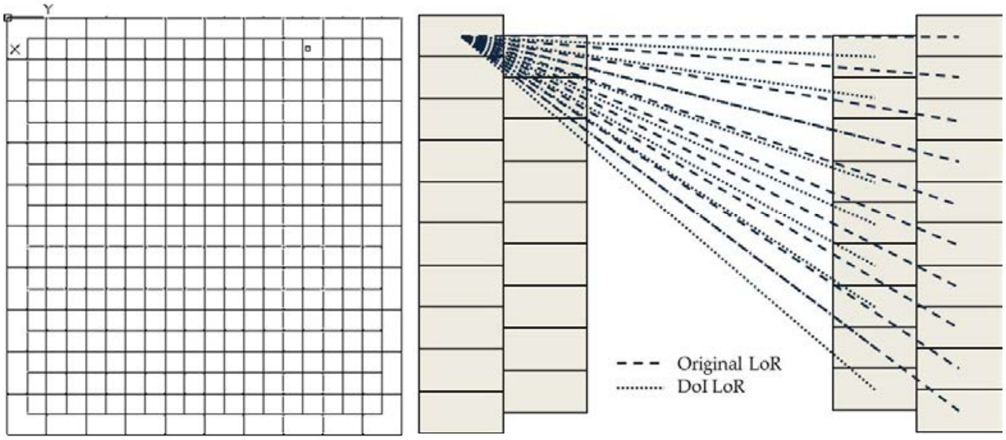

Figure 5.1 Stacked configuration concept: Dotted LORs are added to the dashed ones in DoI scenarios

Moreover, a routine on evaluating, simulating, developing, engraving and testing SSLE scintillators has been developed. This process can be expanded with the necessary studies on DoI and possibility of inclusion of a number of schemes in the available SSLE architectures for radiation detectors.

II. MATERIALS AND METHODS

A. Demonstration of flexibility through novel pixel topologies

A generic study was conducted on the development of pixel geometries different from the standard rectangular or squared ones. This approach has obvious limitations on designing patterns that full cover the face of the scintillator. In this context, arrays of same pixels and tiling patterns [5] where initially researched. This has at least two purposes: to improve light collection at the photodetector coupled to the scintillator crystal; and also to modulate the light-sharing among the different pixels of the position sensitive areas of the photodetector. These characteristics will result in better and more uniform timing, energy and spatial resolution.

Another application concerns the usage of collimators on scintillating detectors, for instance in scintigraphy modalities. In this case also, it was foreseen that pixel geometries coupled to the collimator architecture would provide superior results. The intention to approach more circular designs is also based on the possibility, as estimated from the theory of optical propagation, that round pixels would have superior light-guiding characteristics that would enhance energy and timing resolution of the detector. This tendency can be seen in other scientific fields, as for instance photonics, where optical fibers used have exclusively cylindrical shape. Moreover, the standing goal of a depth of interaction topology leads us to consider different pixel schemes.

Sprouting from the newly gained ability to calculate and design optimal pixel dimensions and surface reflectivity, precise fitting on photodetector dimensions was for the first time possible (figure 5.3), regardless of pixel shape.

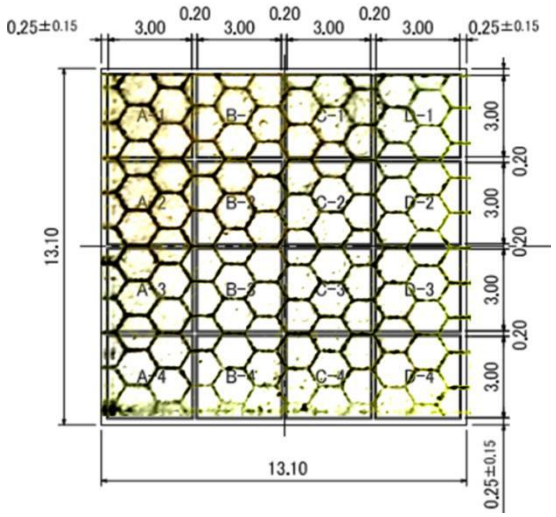

Figure 5.3 4x4 Hamamatsu MPPC s12642 SiPM [6] fitted with hexagonal pixels; symmetry of design guarantees more uniform light collection

However, the main objective addressed by developing such distinct pixel topologies is to benchmark the characteristics and performance of crystal engraving and demonstrate that the gained flexibility doesn't sacrifice precision, control or repeatability of the pixelation process. Having developed routines to work with the SSLE technique, construction of such distinct geometry is as simple as designing it. As can be observed in figure 5.4, the steps necessary for the development of innovative architectures have been in place. For this benchmark a honeycomb design was elected, as the optimal packing solution of the bidimensional Eucledian space [1].

First, the architecture is simulated and light collection results are used to define dimensions and optical characteristics of the design (figure 5.4.A). The acquired experience in using the SSLE setup guides this first step to a great extent. With the application of the known reference between microcrack distribution and laser power on the one side, and average reflectance and thickness on the other, we proceed to the design and development phase. A CAD model of the average microcrack distribution is composed, which after being enhanced with laser pulse characteristics drives the system (figure 5.4.B).

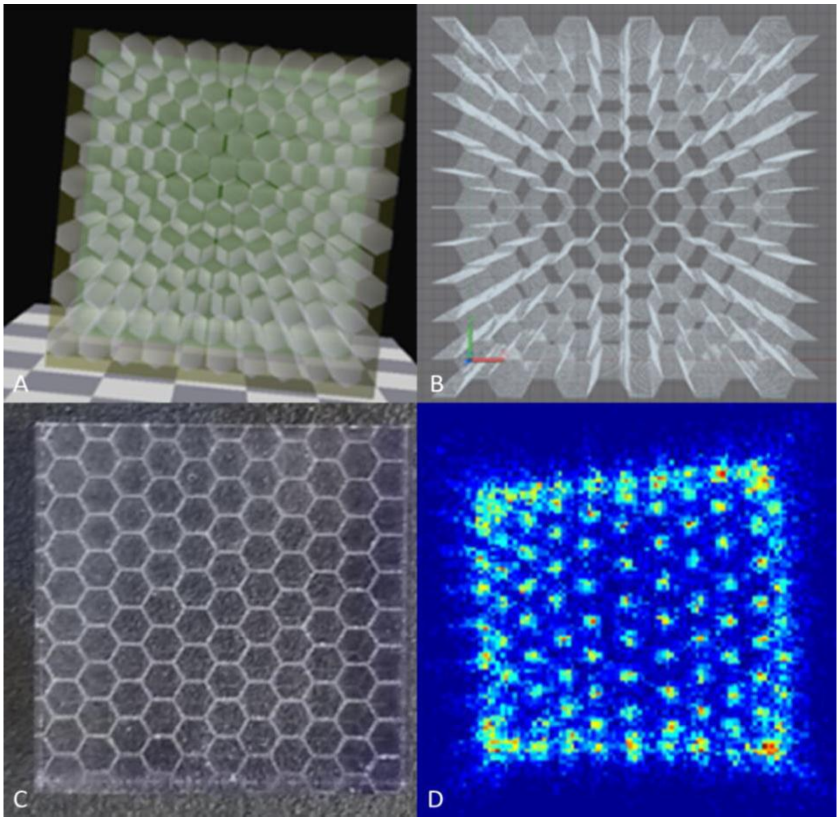

Figure 5.4 A. Simulations phase; B. Design and development phase; C. Engraving phase; and D. Quality assessment phase

At that point, the SSLE process is ready to be launched. After extensive experimentation with machine profiles, it is currently possible to engrave at an approximate rate of one thousand microcracks per second. To quantify this in a real world scenario, a grid of 1.6 mm^2 pixels is developed in a 12.8x12.8x12 mm^3 scintillator in approximately 20 minutes. The transverse spatial precision of the system has been estimated to have a standard deviation of around 5 μm. A LYSO crystal is used and the desired pixel architecture (figure 5.4.C) is engraved. The crystal is finally ready and an evaluation process takes place. The crystal is optically matched to the Hamamatsu R8520-00-C12 PS-PMT, described in the previous chapter using optical grease and illuminated by a ^{22}Na radioactive source. Field-flood map (FFD- figure 5.4.D), profiles and metrics such as pixel resolvability (PR) index are retrieved and used for quantification and verification of the characteristics of the array.

Especially for the honeycomb example of figure 5.4, being the first benchmarking attempt, very useful results were obtained. It can be seen in 5.4.C that at the edges of the crystal the superimposition of the rectangular crystal shape with the hexagonal engraved grid create smaller irregular pentagonal and tetragonal prisms. These were used to explore minimum sized resolvable pixels.

Having developed this routine, it was possible to expand our approach in different novel geometries. Such included also designs with multiple size pixels. Tiling geometries provide full area coverage on both faces of scintillator, making this type of designs applicable not only in experimental, but also in industrial development scenarios, if deemed necessary. The flexibility and distinct pixel geometries study was concluded with the development of dodecagonal prisms as the optimal possibility for approaching the desired cylindrical topology. In a truncated hexagonal tiling geometry (figure 5.5), the small triangular prisms, though too small to be resolved, only deteriorate the packing fraction to a minimum extent [7].

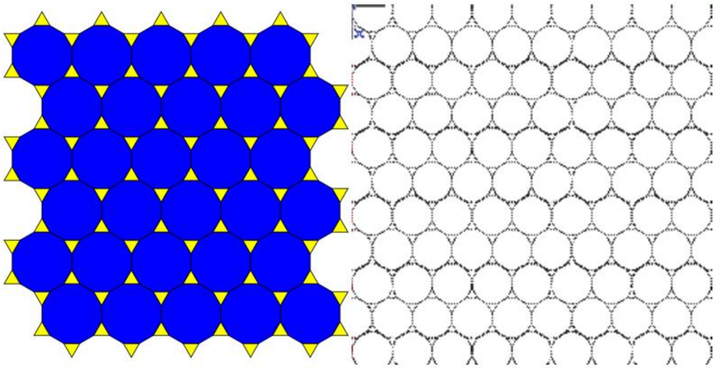

Figure 5.5 (left) Truncated hexagonal tiling; and (right) application on SSLE for scintillators. Dodecagons have area of ~1.4 mm^2

B. DoI approaches on SSLE

As mentioned in previous chapters, DoI approaches exist and include various technology and design innovations [8]. For instance, in figure 5.6 left, the stacked approach is demonstrated. This concept produces event footprints at different positions, depending on the stack, top or bottom, that the sub-pixel that the event took place belongs to (5.6 center). This can be used as a surrogate to localize the event not only by its x and y position, but also by its DoI layer. Such DoI design is easily adaptable to SSLE. To demonstrate this flexibility, we developed a stacked design by engraving a double hexagonal grid, where the top part is displaced by half pixel in both x and y directions (figure 5.3 right). Area of pixels is approximately 1.4 mm^2, while the configuration was tried in a 12.8x12.8x12 mm^2 monolithic LYSO.

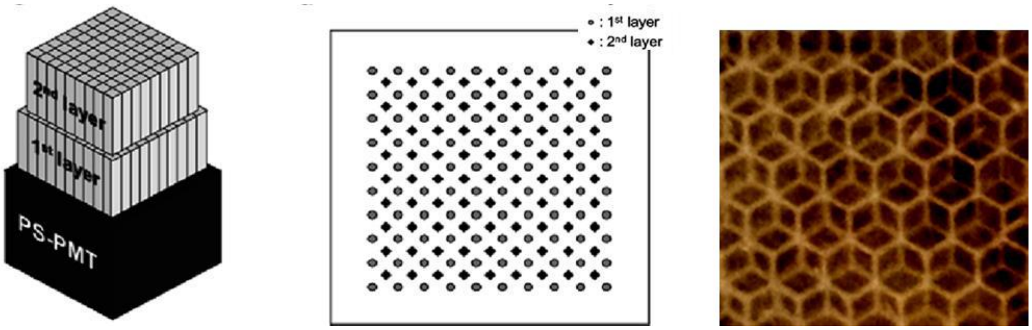

Figure 5.6 (left) stacked DoI approach [3]; (center) center of gravity location for top and bottom layers; and (right) adaptation of this concept in SSLE hexagons

Another design concerns manipulation of the light sharing on different DoI levels, with the intention of producing a position-resolvable DoI surrogate [9]. In the case of ideally reflective and uniform reflectors, no matter where the scintillation event takes place, the center of energy will be at the center of the pixel. This happens because the statistic possibility of photons reaching the detecting surface is geometrically symmetrical, due to the uniform ideal reflection. As explained in figure 5.7 left though, if a percentage of light is shared with neighboring pixels, the symmetry is broken and the spatial distribution of detected photons at the photodetector will be gradually shifted.

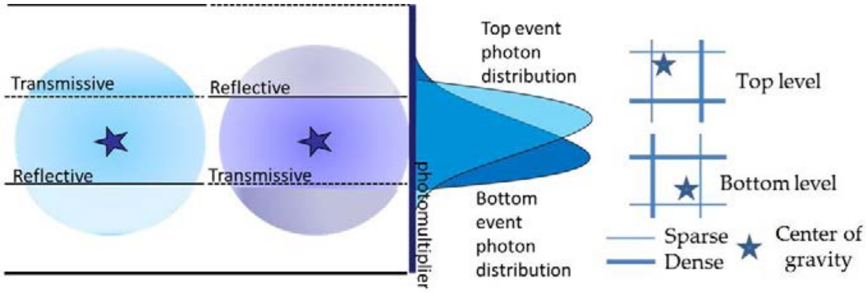

Figure 5.7 (left) controlled surface characteristics DoI approach: top (light blue) and bottom (dark blue) events and their respective light distribution; and (right) bidimensional adaptation for for SSLE

Controlling the surface characteristics for DoI can be facilitated, taking into account the semi-transparent nature of engraved walls. In figure 5.7 right, the principle is adapted to SSLE, by changing "reflective" and "transmissive" with "dense" and "sparse", respectively. This approach was studied and simulated also in a honeycomb grid design of 1.4 mm^2 area pixels before being engraved in a 12.8x12.8x12 mm^2 monolithic LYSO (figure 5.8).

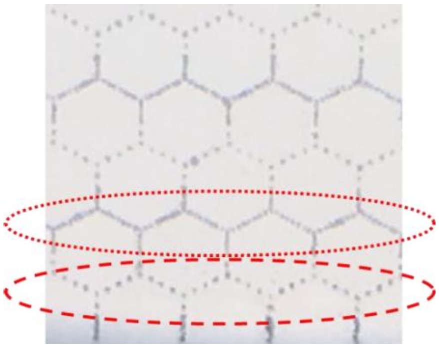

Figure 5.8 Controlled transparency SSLE design; Dotted demonstrates an area of dense engraving, dashed one of sparse

Another approach addresses the possibility of DoI in angled crystal configurations, detectable with a slight modification of the readout circuit [10]. The time-energy distribution is noted to change according to the gradual change of pixel size, providing DoI information. In figure 5.9, the CAD conceptual design integrating this approach by the application of a truncated square tiling patron [5] is demonstrated. The ratio of octagon to square areas is $2 \times (1 + \sqrt{2}) \approx 4.8$. The angle of the SSLE walls at the example depicted, of 8 mm crystal depth and 1 mm square side approximately 15°. Pixel walls cross in this design due to the geometrical distribution created by the misplacement of the tiling design on the two faces of the crystal. This complex irregular solid type is very difficult to be created in separate pixels and can be effectively realized through the application of SSLE.

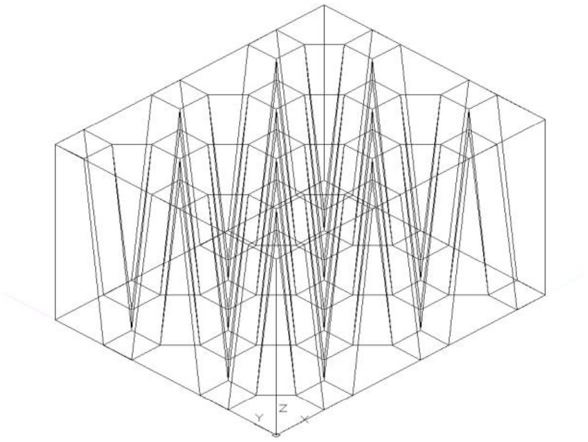

Figure 5.9 Angled pixels configuration concept

Phoswich concerns stacking different scintillators with distinct pulse shapes that can be resolved at the time-energy plane, commonly by integrating the incurring scintillation pulse over a time window (figure 5.10). A pair of scintillator crystals often used in phoswich is LYSO and GSO. While SSLE can't change the timing characteristics of the engraved scintillator to create phoswich inside the same monolithic crystal, in the previous chapter it was demonstrated that both GSO and LYSO have been successfully tried with SSLE, adding another possible DoI application in the repertoire.

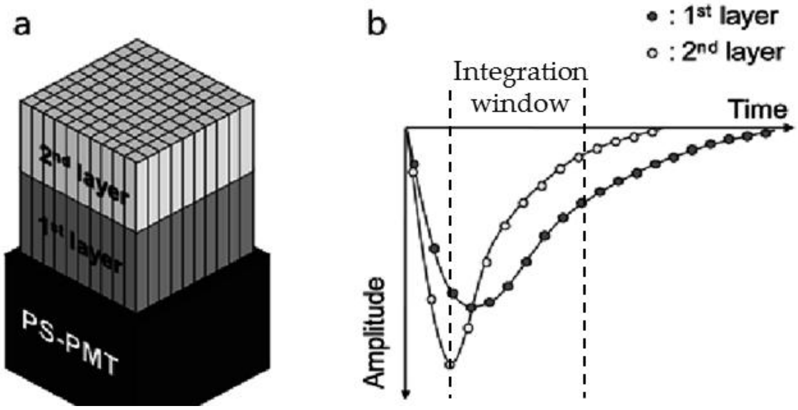

Figure 5.10 Phoswich approach [10]

C. Theoretical framework for the addition of more layers

Other approaches presented concern designs with two photodetectors placed at both ends of the crystal [11] or with more than two DoI levels [12]. Either approach can be directly included in SSLE development studies and possibly greatly facilitated and expanded. For instance, a scenario concerning two transparency levels interchanged in such manner that can produce nine DoI layers, was developed (figure 5.11). A cluster of 3x3 pixels is engraved with the procession of dense and sparse surfaces at nine different layers (5.11 right). The centers of energy of events corresponding to these layers will be roughly placed around the areas of pixel shown in 5.11 left. The same geometric algorithm can be expanded in pixel clusters of 4x4, to produce 16 layers. It can also be directly adapted to prisms with more sides in the same manner like for two layers.

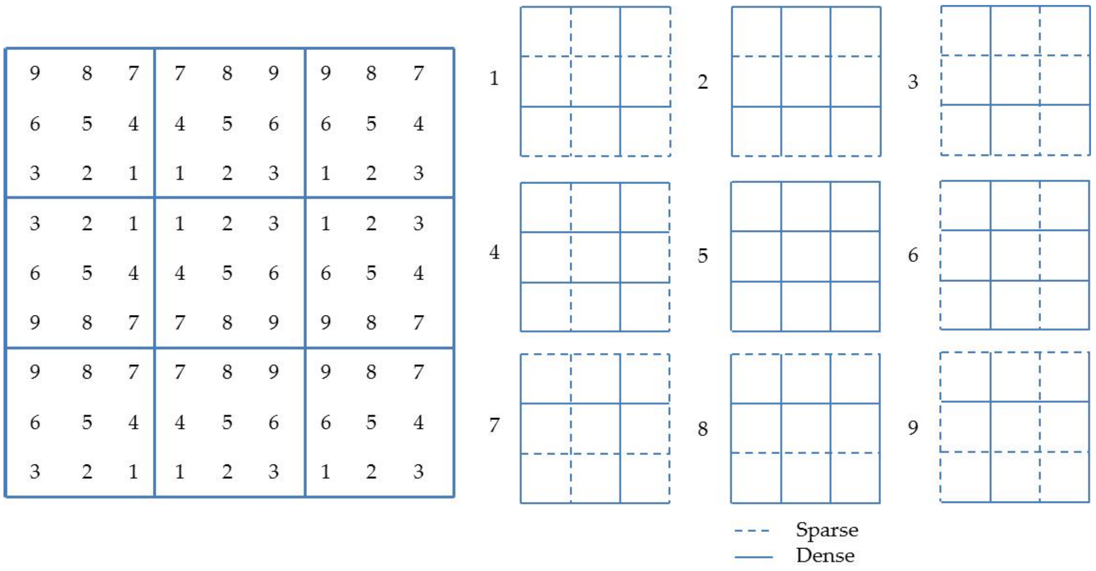

9	8	7	7	8	9	9	8	7
6	5	4	4	5	6	6	5	4
3	2	1	1	2	3	1	2	3
3	2	1	1	2	3	1	2	3
6	5	4	4	5	6	6	5	4
9	8	7	7	8	9	9	8	7
9	8	7	7	8	9	9	8	7
6	5	4	4	5	6	6	5	4
3	2	1	1	2	3	1	2	3

Figure 5.11 A 3x3 pixel cluster and the positions of centers of energy for corresponding 1-9 DoI layers (left), engraved in different dense and sparse alternations per level (right)

With this study a question arises: How many DoI layers can be pushed in pixel array architecture? A hard limit for amount and size DoI configurations is when a scintillation event can be attributed to a particular DoI level with enough confidence. This limit is of course depending on the DoI technique and readout, but for position surrogate designs it could be traced using a metric similar to pixel resolvability (PR, equation 3.3). Adapted for DoI layers, DoI Layer Resolvability (LR) is presented in equation 5.1. In the same manner as the threshold set on PR to distinguish resolvable pixels, in the LR DoI position surrogate a limit was also applied. When this value is 1, there is 2.355σ confidence on the characterization of the DoI layer of an event. The threshold was set at this value.

$$LR_{DoI} = \frac{FWHM_{top}+FWHM_{bottom}}{2*\sqrt{(x_{top}-x_{bottom})^2+(y_{top}-y_{bottom})^2}} \qquad \text{Equation 5.1}$$

However, such approaches could benefit greatly by the application of prior knowledge of specifics on detector architecture [13], while experiments precisely expanding this knowledge can be performed. Nevertheless, the number of desired DoI layers is limited by the geometrical survey of the tomograph design and relative size of FoV [1].

Optimization of this study comes with optimization of the geometrical packing of centers. An equilibrated topology is designed, when the centers of neighboring pixels (p) and DoI layers (l) are equally spaced. This is called regular distribution of points, as contrasted to random and clustered [14]. It is not important if a (p,l) peak belongs to one or the other layer. This can be considered again as an application to the circle packing problem, given that the distributions in a FFD are fitted with bivariate normal function shapes around a central maximum.

In theory, the resulting shapes are expected to be circular, due to the anticipated symmetry of the pixels and corresponding light distribution and known uncertainty of center of energy position. Setting different thresholds of resolvability changes the dimensions of the circles. In practice, due to unavoidable construction characteristics, the shape tends to be ellipsoidal, however the analysis doesn't change. As optimal packing corresponds to regular distribution of the centers, this can be approached by equation 5.1. However, the minimum center distance must be taken, and an overlapping threshold should be set. In this context, DoI with hexagons is the most advantageous solution, as mentioned already. Thus, as for the honeycomb benchmarking design, the DoI study has also been entirely conducted using hexagonal patterns.

This equilibrium can be equally described for more layers. In order to provide a quantifiable solution we consider each elemental (p,l) maximum as a node. Dividing the available FFD space by the number of peaks (corresponding to number of pixels multiplied by number of DoI layers) and placing one node per area provides the uniform solution. To construct a metric, we take the assumption that these nodes would tend to cluster in groupings of n_{DoI}, as a result of the physical construction of n-layer DoI. We connect all nodes among them and create sub-graphs by choosing the n closest nodes to each, representing maximum proximity neighborhoods. Then, the average length of edges is calculated. Minimum deviation from this average represents optimal and uniform packing, and the normalized value of this measure can be used as a figure of merit. In this approach, scintillation events with centers of energy within the overlapping zone between normal function maxima can't be attributed to any element. However, novel approaches can be considered, given that automatic pattern recognition methods are becoming available, as shown in the next section.

III. RESULTS

A. *Hexagonal array results*

As now the procedure demonstrated in figure 5.4 is finally complete, radiation of a ^{22}Na source was acquired for the honeycomb benchmarking design. As a metric of the pixel quality, we calculate the average pixel resolvability as described in equation 3.3. The image is fitted with the bivariate normal model for each pixel, in order to extract the FWHM (figure 5.12). For the hexagonal grid, an average of the six neighboring maxima was used for this calculation. Furthermore, a limit was set to the PR function. If the FWHM is bigger than the average center-to-center distance, the pixel is considered not resolvable. Profiles are also depicted to show uniform behavior regardless of transverse direction.

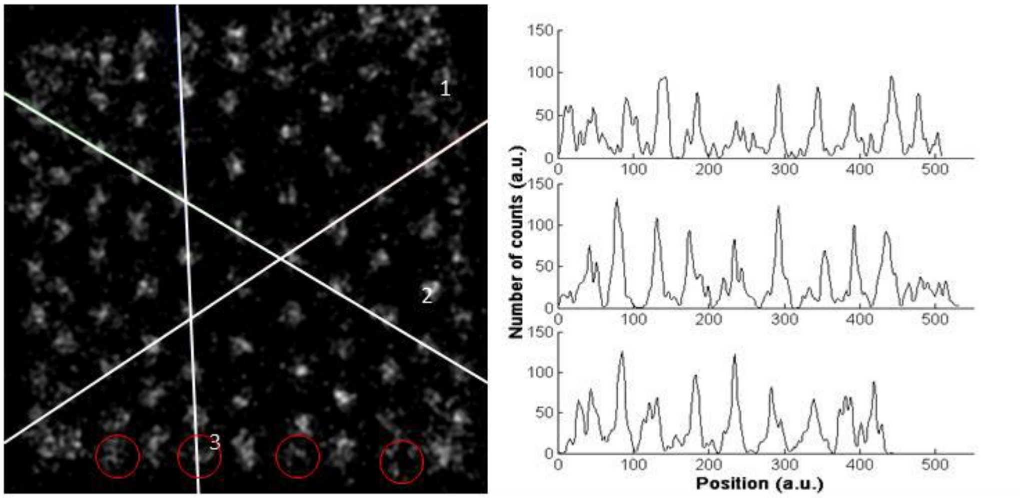

Figure 5.12 (Left) grayscale FFD with minimum size resolvable pixels in red circles; and (right) profiles corresponding to the numbered cuts

As foreseen by the nature of the engraving example, the distribution is uneven but an average PR at 0.32 is demonstrated. This is a very hopeful result for SSLE light-guides of approximately 35-40% reflectance. Non hexagonal prisms at the edges were resolvable to a lesser extent, as not only the interaction of light with the external reflector distorts the transverse location of center of energy, but also because the distance with the centers of neighboring pixels is smaller. Nevertheless, smallest resolvable pixels have an area of 0.95 mm^2.

It has been theorized [1] that by choosing a honeycomb design, we allow the maximum area possible per pixel. This, in comparison to the square equivalent of same pixel area, is an improvement of 8.8% which corresponds to the distance between the centers, explaining why the honeycomb design is better than the square SSLE arrays presented in the previous chapter.

B. DoI results

Due to limitations in material and read-out resources, it was not possible to try all the studied DoI architectures, as some would require the study and development of whole novel detector modules. In figure 5.13 DoI results for two designed approaches are demonstrated. On the left a controlled transparency design was illuminated by a ^{22}Na gamma source. The limitations of the study are observed, as even though the intention was to calculate reflectivity in order to create a uniform distance pattern, DoI layers are clustered; nevertheless, in general also resolvable. The free space around these clusters demonstrates that the DoI capacity is higher for this configuration and threshold, thus at least two more DoI levels could be tried. In the FFD of the stacked approach in figure 5.9, right, clustering has been avoided and DoI levels are more regularly spaced. Indeed, in this manner resolvability is observably better, even though a gradient difference in spacing between top and bottom grids can also be noticed. This can be quantified and attributed to the effect of the external reflector. Initially, the LR figure of merit was applied and results are demonstrated in table 5.1.

Table 5.1 DoI LR index results for different techniques

DoI technique	Minimum	Average
Stacked	0.6	1.06
Controlled transparency	0.9	1.2

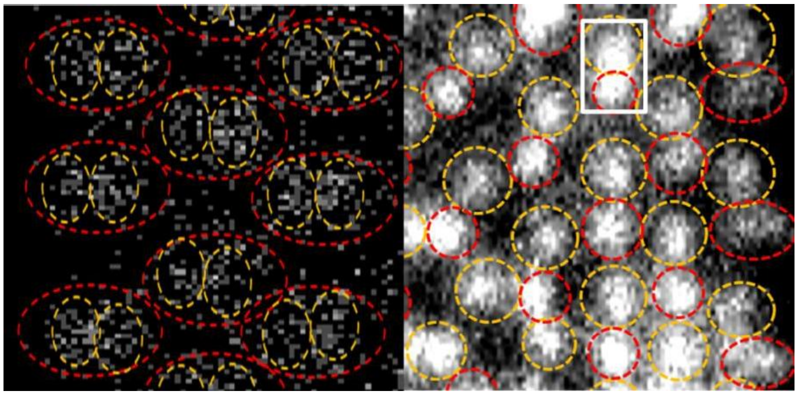

Figure 5.13 DoI results: (left) controlled transparency and (right) stacked configuration

By comparing the DoI scenarios presented above with a phoswich scenario [15], it can be demonstrated that the stopping power of this configuration is approximately 21% higher, due to the higher packing fraction and higher density of LYSO, compared to GSO.

Furthermore, for pixelated arrays used on small animal systems with pixel size smaller than the detector pixel size, lightguides are used, in order to achieve the light sharing necessary. Such light guides offer substantial advantage on resolving the position of the scintillating event, enhancing the spatial resolution of the detector. Light guides can be used at different depths, depending on the application and readout [16]. In the SSLE scenario, we can make the engraved surfaces semi-transparent to improve light sharing, thus removing the need for a light guide.

Due to these two characteristics, SSLE crystals are ideal for detectors where high sensitivity and small dimensions are paramount, such as MR compatible PET inserts. Compared to a phoswich of 6mm GSO and 6mm LYSO with a lightguide of 2mm, the equivalent necessary SSLE LYSO is only 9.5mm deep, 32% shorter.

C. *Fuzzy logic approach*

For more levels, or when the LR figure of merit exceeds the threshold set by far, a novel approach drawn from the field of fuzzy logic was deemed necessary and has been developed. In this, an event is not directly characterized as belonging to one DoI layer, but by the probability it has of having occurred there. This is in principle an unsupervised learning algorithm that can be applied to unearth the DoI of a scintillating event based on prior study of the FFD and matching with DoI features extracted through experimentation. The image is fitted using the bivariate normal function for each detected peak as in the non DoI designs. Different peaks are attributed to different pixels and DoI layers (p,l). This can happen either automatically, by interchanging attributed DoI layers, or by hand.

The probability of a position of the image belonging to any of the (p,l) as compared to all other (p,l) is given by equation 5.2. In figure 5.14 the process is described in a single-dimension example of the region delineated in a white rectangle in figure 5.13. The profile fit of a bad pixel is demonstrated along with the fitted curves. In table 5.2 the values of various are given.

$$P(p,l,x,y) = \frac{Gauss(p,l,x,y)}{\sum_{pixel,level} Gauss(p,l,x,y)}, \forall(p,l,x,y) \qquad \text{equation 5.2}$$

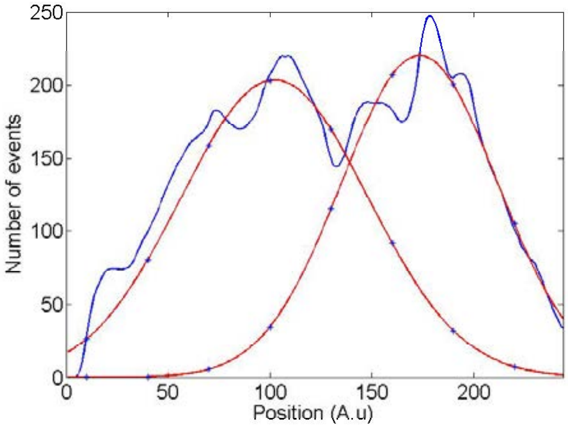

Figure 5.14 Example of high-proximity DoI distributions (blue) and their Gaussian fit (red). The stars show the positions of table 4.3 in one axis.

Table 5.2: demonstration of fuzzy logic results for different positions

x (A.u.)	10	40	70	100	130	160	190	240
P(1,x)	0.9991	0.9939	0.9656	0.8540	0.5950	0.3074	0.1389	0.0659
P(2,x)	0.0061	0.0009	0.0344	0.1460	0.4050	0.6926	0.8611	0.9341

With the application of the algorithm and the equation 5.2 it can be demonstrated that even for this difficult case, most of the area (69%) can be attributed to one DoI layer with more than 0.8 probability. This approach can have a systematic character, evaluating the quality of a detector. The average maximum percentage for all locations, as in equation 5.3, can be used as a figure of merit.

$$FoM = \langle \max(P(x,y)) \rangle,\ \forall (x,y) \qquad \text{equation 5.3}$$

Due to the fuzzy nature of SSLE scintillators, sprouting from the uncertainty and lack of uniformity of the engraving process and ensuing reflectance/transparency distribution, it could be commented that this type of metric can be more applicable. However, such application can only be pursued if and once the DoI behavior has been properly characterized, by dedicated experiments applying collimated beams. It can be expected that then also spurious but deterministically repeatable DoI layers might be observed and put into application without any expansion of this fuzzy model.

IV. CONCLUSIONS

Liberation of the pixel geometry design towards non-conventional shapes is equally possible as the standard rectangular shape, facilitating matching the scintillating pixel to the exact necessities of every application, as for instance matching with collimators or the dimensions of silicon photomultiplier pixels. Exotic designs, such as Voronoi tessellations can be easily engraved inside monolithic crystals, while a random distribution of pixel sizes can facilitate the application and expansion of compressed sensing techniques [17], given the extensive light sharing, a subject that will be discussed in the next chapter.

Hexagonal prisms have been elected as optimizing the packing fraction and spatial resolution, an important tradeoff that has been difficult to overlook. In the same manner it could be expected that better light guiding, a feature of more blunt shapes, could lead to better timing behavior. However, simulations have been inconclusive on whether hexagonal or dodecagonal pixelation could lead to better timing due to better light-guiding, which could be the case, taking the example of optical fibers. Precise measurement and experimentation needs to be performed for the timing behavior of SSLE pixelation to be estimated.

Most of Depth-of-Interaction techniques for conventional pixels found in literature, with the exception of phoswich, can be developed with the same ease, thus designs with DOI properties can also be generated within a monolithic scintillator crystal without any additional cost. More precise simulation and further experimentation with existing and novel techniques, exploring their application in SSLE is foreseen.

DoI characteristics can be added to any distinct geometry imaginable, expanding the application of SSLE. More measurements, especially ones using a collimated beam, will be performed, and more precise light guiding simulations, including the effect of external reflector to DoI light collection will be designed. In this manner, valuable information for the characterization and improvement of DoI designs will be collected, while designs with more levels will be made possible.

Moreover, a non-classical algorithm has been proposed to resolve the position of scintillation events, enhancing information gathering and possibly improving the spatial resolution of detectors applying SSLE. This algorithm has automatic characteristics and can easily implemented in look-up tables in low cost FPGAs, while by its fuzzy nature matches the general SSLE process and its non-uniform nature. More details and precise quantification can occur only by the application in tomographs and comparative studies with other algorithms.

However, application of DoI through a spatial surrogate means that existing and serviceable tomographs can be directly upgraded with hexagonal SSLE DoI crystals and enhance their performance in a cost-effective and easy manner, proposing an industrial alternative that combines classical geometrical theories, material science and laser manufacturing with nuclear medicine applications.

V. REFERENCES

[1] Chang, Hai-Chau; Wang, Lih-Chung (2010). "A Simple Proof of Thue's Theorem on Circle Packing". arXiv:1009.4322

[2] Adams, M. J. (1981). An introduction to optical waveguides (Vol. 14). New York: Wiley.

[3] Van Der Laan, D. J., Maas, M. C., Schaart, D. R., Bruyndonckx, P., Léonard, S., & van Eijk, C. W. (2006). Using Cramér-Rao theory combined with Monte Carlo simulations for the optimization of monolithic scintillator PET detectors. IEEE transactions on nuclear science, 53(3), 1063-1070.

[4] Moses, W. W., & Derenzo, S. E. (1994). Design studies for a PET detector module using a PIN photodiode to measure depth of interaction. IEEE Transactions on Nuclear Science, 41(4), 1441-1445.

[5] Grünbaum, B. Shephard, G. C. (1987). Tilings and Patterns. New York: W. H. Freeman. ISBN 0-7167-1193-1

[6] Hamamatsu MPPC TSV reference sheet, http://www.nuclear.gla.ac.uk/~jrma/A2/Tagger/NewFPD/SiPMT/KSX-I50014-E_S12642%20Series%20(3mm%E2%96%A1-TSV%E3%83%BCArray).pdf, retrieved 11.01.2017

[7] Hales, T. C. (2000). Cannonballs and honeycombs. Notices-American Mathematical Society, 47(4), 440-449.

[8] Ito, M., Hong, S. J., & Lee, J. S. (2011). Positron Emission Tomography (PET) detectors with Depth-of-Interaction (DoI) capability. Biomedical Engineering Letters, 1(2), 70-81.

[9] Miyaoka, R. S., Lewellen, T. K., Yu, H., & McDaniel, D. L. (1998). Design of a Depth of Interaction (DoI) PET detector module. IEEE Transactions on Nuclear Science, 45(3), 1069-1073.

[10] Lerche, C. W., Ros, A., Herrero, V., Esteve, R., Monzo, J. M., Sebastia, Á., ... & Benlloch, J. M. (2008). Dependency of energy-, position-and Depth of Interaction resolution on scintillation crystal coating and geometry. IEEE Transactions on Nuclear Science, 55(3), 1344-1351.

[11] Huber, J. S., Moses, W. W., Andreaco, M. S., & Petterson, O. (2000). A LSO scintillator array for a PET detector module with depth of interaction measurement. In Nuclear Science Symposium Conference Record, 2000 IEEE (Vol. 2, pp. 14-46). IEEE.

[12] Seidel, J., Vaquero, J. J., Siegel, S., Gandler, W. R., & Green, M. V. (1999). Depth identification accuracy of a three layer phoswich PET detector module. IEEE Transactions on Nuclear Science, 46(3), 485-490.

[13] España, S., Herraiz, J. L., Vicente, E., Herranz, E., Vaquero, J. J., Desco, M., & Udías, J. M. (2007, October). Improved image reconstruction in small animal PET using a priori estimates of single-pixel events. In 2007 IEEE Nuclear Science Symposium Conference Record (Vol. 5, pp. 3876-3880)

[14] Cressie, N., & Wikle, C. K. (2015). Statistics for spatio-temporal data. John Wiley & Sons.

[15] Vaquero, J. J., Seidel, J., Siegel, S., Gandler, W. R., & Green, M. V. (1998). Performance characteristics of a compact position-sensitive LSO detector module. IEEE transactions on medical imaging, 17(6), 967-978.

[16] Kang, J., & Choi, Y. (2016). Simulation study of PET detector configuration with thick light guide and GAPD array having large-area microcells for high effective quantum efficiency. Computer methods and programs in biomedicine, 131, 79-87.

[17] Chinn, G., Olcott, P. D., & Levin, C. S. (2013). Sparse signal recovery methods for multiplexing PET detector readout. IEEE transactions on medical imaging, 32(5), 932-942.

Chapter 6: A time-over-threshold technique for multiplexed read-outs of MR compatible PET inserts

I. INTRODUCTION

A. General

Until now, the main concern of our work had been to develop and expand the characteristics and specifications of innovative detectors, mainly by developing concepts related to the scintillation crystal and pixel design. However, this is only a partial goal. Detectors need to be considered not as single independent devices, but included in the framework of their specific application. While the sub-surface laser engraving (SSLE) study can be considered for various designs of broader objectives, such as astrophysics, particle physics, phytology and other, the goal is to use it for nuclear medicine appliances.

The merits for particular application in novel MR compatible PET inserts have already been discussed. In brief, they concern the superb packing fraction that allows shorter scintillators to acquire equivalent stopping power as compared to standard pixelated arrays; easily implementable depth-of-interaction features; compatibility with standard read-out techniques used for pixelated arrays, in comparison with other monolithic approaches; and finally, notable cost-effectiveness.

Other aspects can’t be addressed by processing the scintillator. As explained in the second chapter, the standard approach includes photodetectors and several layers of electronics to perform the necessary conversions (figure 6.1). Apart from the scintillator, other aspects also provide engineering challenges that support extensive research, in order to be applicable or improved for MR compatibility.

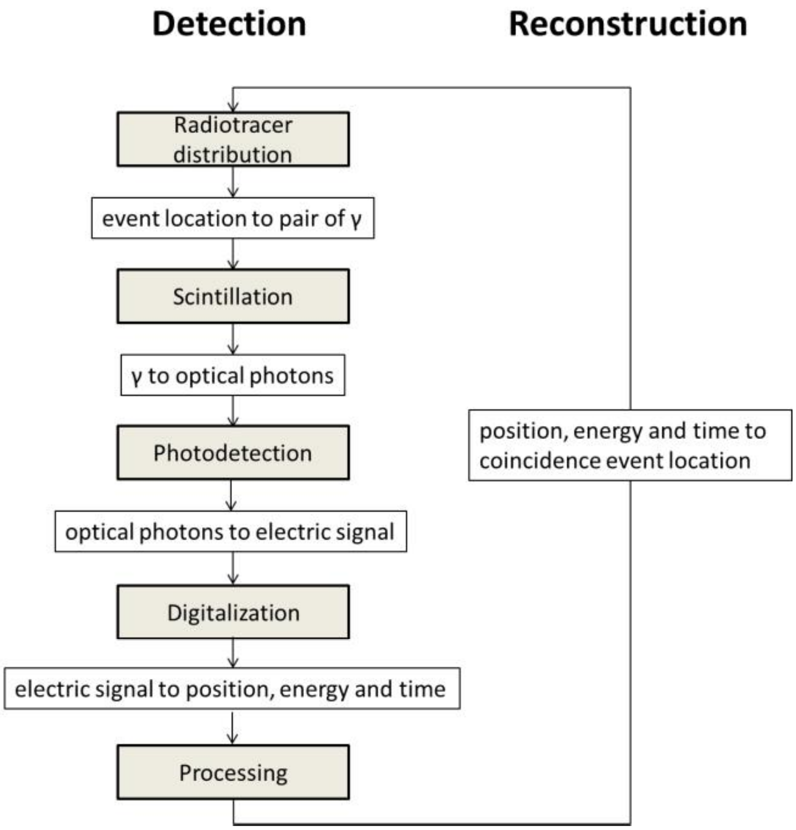

Figure 6.1 Schematic representation of the conversions required in order to reconstruct the tridimensional distribution of radiotracer inside a subject

In order to expand the study from a single detector to a complete tomograph, the idea of what geometry is best to cover the space around the subject under study with detector elements is one aspect. Moreover, it is necessary to get into some depth on the architecture of interconnection of the photodetectors and try to approach optimal solutions, in terms of material usage, power consumption, data throughput, volume and architecture flexibility. Deep understanding of the scintillation signal as recorded from the photodetectors is necessary to produce and apply possibly beneficial signal treatment schemes for this purpose. Also, signal multiplexing approaches that have already been mentioned in a general sense, should be further analyzed. Finally, the differences between a small animal detector and a human equivalent need to be noted, since the application and radiotracer dosage vary.

B. Detector to tomograph scaling-up considerations

As was already the case in the pioneering works [1,2], the question of how exactly the individual detectors can be arranged, in order to achieve maximum coverage of the geometrical space around the subject is valid still today. This has a direct effect on sensitivity, but might hinder the medical or experimental process, or cause distress [3]. In the core of scaling up lies the organization of independent detector elements.

Up to know, we considered the elemental detector as the minimum detector element at which lines-of-response (LOR) can be attributed. A more precise description, however, takes into account all the details of matching between scintillator elements and the photodetector. Since the inserts under discussion are foreseen to function inside a magnetic field and are required to have as small size as possible and MR compatibility, silicon based photodetectors are the devices of choice.

One approach is the application of single photon avalanche diodes (SPADs) or digital silicon photomultipliers (dSiPM), as described in [4,5,6]. The later design has been a breakthrough on the discussed application and as such has revealed the difficulties: Massive interconnection necessary between the photodetector and corresponding digital logic requires a digital station to be placed inside the MR bore [7]. This is a problematic condition given that digital electronics are susceptible to error inside magnetic field due to spurious currents induced, called "Eddy" currents [8]. Moreover, as can be observed in figure 6.2, this solution is not only bulky and power hungry, thus requiring digital transceivers and active cooling (A), but also creates distortion of the magnetic field (B) which asks for thicker shielding (C).

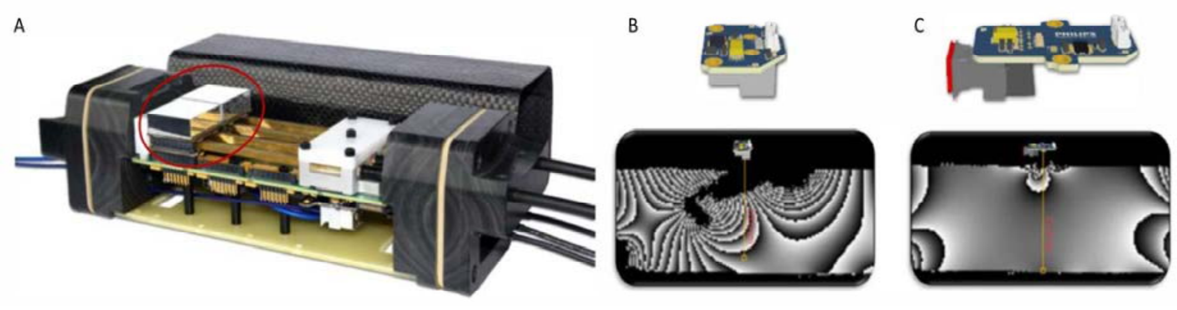

Figure 6.2 Hyperion II PET insert [7]; (A) For the dSiPM in the red circle, massive electronics are required within the magnetic field; (B) heavy magnetic field distortion due to transceiver; and (C) less magnetic field distortion attributed to power electronics and digitalization

While we describe the requirement of direct digitalization as a vice, in other cases it can be considered as a virtue, because with this type of photodetection single photon detection is possible, providing superb timing and directly resolving depth of interaction (DoI) questions. Nevertheless, it is not only a matter of principle, but equally a matter of optimization to demonstrate whether simpler and smaller designs are also possible.

An intermediate solution is that of using silicon photomultipliers (SiPM) which, as described in the second chapter, are an approach including parallel interconnection of micrometer size avalanche diodes [9]. Groupings of size of few millimeters match, in general, the dimensions of scintillators for human applications. The quasi-analog signal created in the case of photon detection can be read-out by independent channels per SiPM pixel [10]. This design takes advantage of the sparse spatiotemporal nature of photon detection, meaning that it is unlikely to have a lot of independent photon events at any given moment. First photon detection is possible, providing robust energy and timing resolution specifications and readout is a lot lighter; however, presence of digital electronics inside the highly magnetic environment of MR is again unavoidable due to the still extensive requirements for interconnection.

The only way to provide solutions that allow even lower number of independent readout channels, desirable for lower cost and complexity, is to use analog multiplexing approaches. Such approaches have been historically the standard for block detectors based on photomultiplier tubes (PMT) and the most common architecture is a charge division multiplexing (CDM) network [11]. In figure 6.3 the first such network is presented (left) along with a simplified square analogous (right), where variable resistor values create a unique combination of outputs X_1, X_2, Y_1, Y_2 that can reveal the position and energy of an event according to equations 6.1.

$$X = \frac{X_1 - X_2}{X_1 + X_2},\ Y = \frac{Y_1 - Y_2}{Y_1 + Y_2},\ E = X_1 + X_2 + Y_1 + Y_2 \qquad \text{Equations 6.1}$$

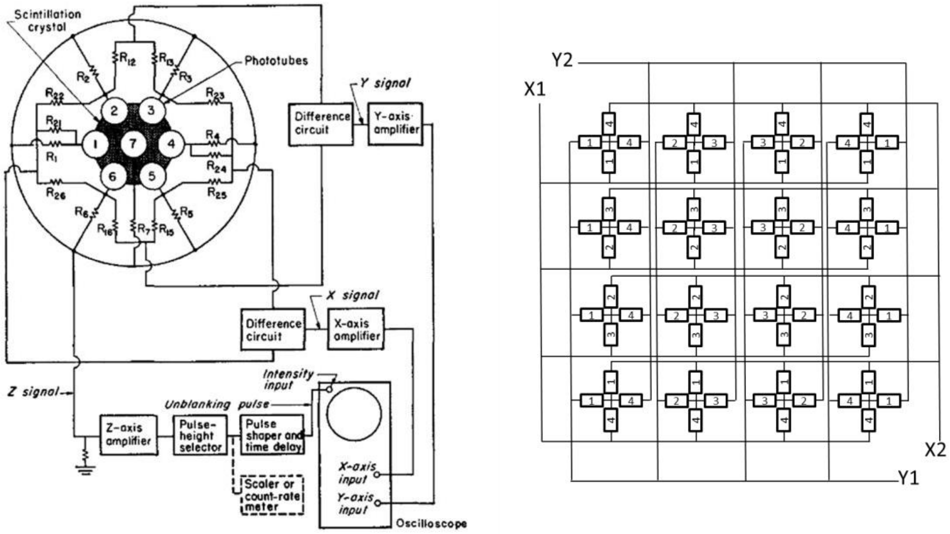

Figure 6. 3 (Left) first demonstration of CDM for nuclear applications; and (right) the square analogous circuit

Different approaches (figure 6.4) of the same CDM idea exist with the intention of either lowering the amount of elements necessary (figure 6.4.A) [12]. For applications with SiPM there is a main drawback [13]. Due to the capacitance added by the network by the high capacitance of SiPMs, spurious low-pass filtering occurs, deteriorating the timing behavior of such detectors. Transimpedance amplifiers provide a remedy for this condition (figure 6.4.B). A slightly different approach takes advantage of the two-terminal nature of SiPM. In cross-strip multiplexing [14], the fact that both sides of the diode have in principle same signal behavior, while being separated by the non-linear elemental diode is applied (figure 6.4.C). This design has been developed with the same MR compatible PET insert topology in mind.

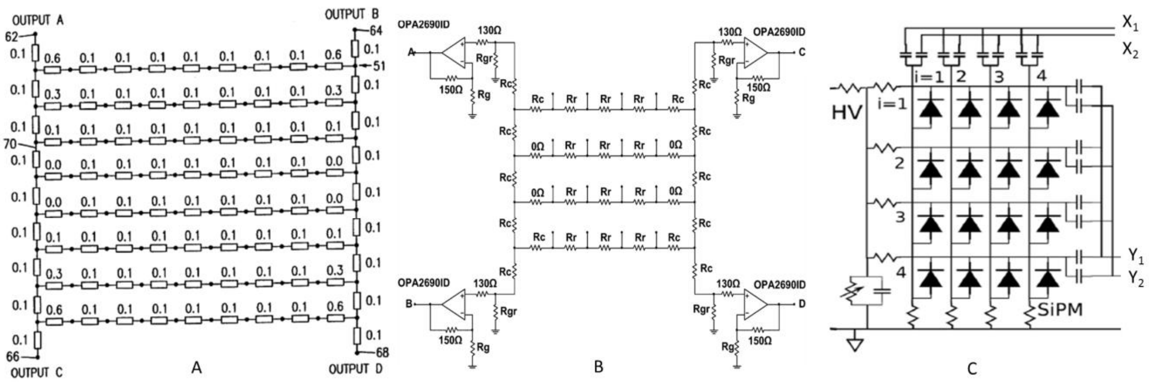

Figure 6. 4 Alternative CDM architectures [12, 13, 14]

The aforementioned designs address approaches where either direct scintillator to SiPM pixel matching is the case, or the dimensions of scintillator pixels are bigger or smaller than those of the SiPM. In this case, light-sharing is necessary [15]. Noise sensitivity studies are required to confirm that light-sharing is enough and not excessive.

Same studies need to be performed in order to define the maximum amount of elements that can be multiplexed in the same outputs. For instance, one can claim that since the (X, Y, E) area of results is tridimensional, so should the (A, B, C) space of electronic multiplexing outputs be. Such designs have been presented [16] but demonstrate incondonable uncertainty. Setting thus the current limit of the denominator at 3, the size of the numerator needs to be discussed.

Linearity of conversion of X_1, X_2, Y_1, Y_2 to (X, Y, E) tuples is the standard. However, novel pre-processing corrections can be applied transforming the objective of linearity to that of injective relation between circuit outputs and event energy and coordinates. In this context, newer designs have tried to approach this subject by non-linear multiplexing attempts. As has been demonstrated in [17], the spatiotemporal sparsity of PET signal can be taken advantage of and state of the art sparse reconstruction techniques could be applied [18]. As demonstrated in figure 6.5, light sharing can control the sparsity of the light detection correlation matrix and compressed sensing analysis can provide ratios of multiplexing as high as 16:4, similar to the standard technique. Moreover this design is demonstrated to be insensitive to noise through the application of a dictionary of possible combinations. This approach is ideal for MR compatible inserts due to the very high multiplexing ratio they demonstrate and lightweight design [19].

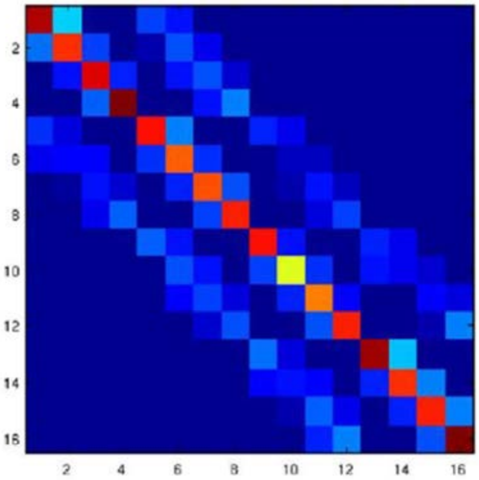

Figure 6. 5 Sparse matrix of correlation of light detection among the 16 pixels of a SiPM based block detector [17]

C. Signal characteristics

Another manner of limiting the cost and complexity is treating scintillation pulses with a non-linear function. It has been demonstrated that those pulses, as recorded by photodetectors, have a standard form which in general is modelled as a biexponential expression (equation 6.2). This form corresponds to the physical characteristics of the scintillator chosen as the fast (τ_{rise}) and slow (τ_{decay}) coefficients are characteristic of material and doping [20], as already demonstrated in table 2.1. Intrinsic photodetector and circuit capacitance can have an important but measurable effect on the bandwidth of the pulse, accordingly affecting those coefficients. This is the case especially in high ratio multiplexing approaches due to extensive interconnection of parallel branches.

$$f(t) = \frac{1}{\tau_{decay} - \tau_{rise}} \left(e^{-\frac{t}{\tau_{rise}}} - e^{-\frac{t}{\tau_{decay}}} \right) \qquad \text{Equation 6.2}$$

It is calculable that there is an injective relation between the duration of a pulse along this model over a given amplitude threshold and its energy. Compromising factors are the noise and baseline restoration, irrelevant at the fast rising edge, but severely distorting the slower falling one. This approach of measuring the time over threshold (ToT- figure 6.6) instead of calculating the energy of analog pulses is commonplace in high-energy physics experiments and extensively applied and documented [21, 22, 23]. Creating a binary signal that can be transformed in digital through time-digital converters (TDC [24]) and transmitted through digital communication devices lowers greatly the data throughput and processing power requirements. In this context it is also used in PET inserts [10] with proven results.

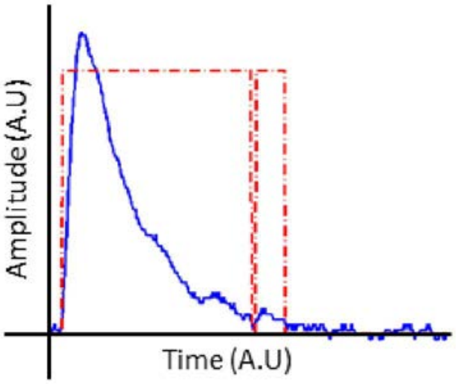

Figure 6. 6 Typical scintillation pulse and ToT equivalent

In ToT applications it is common to have to take into account siginifcant hysterisis, especially when the slope of the signal is slow.Presence of noise is also the reason why ToT architectures have limited accuracy and are very sensitive. Timing can be easily retrieved from the ToT time measurement that corresponds to energy. However, analytical corrections or fitting to a model can be applied.

An extension of the ToT approach is the multi-voltage-threshold (MVT) ToT, where in order to minimize the effect of noise on the duration of ToT, several different voltage thresholds are set and a pseudo, low resolution analog to digital conversion (ADC) takes place. For such design, fitting the acquired pulses to a known model is possible, nevertheless robust time and energy resolution results have already been demonstrated [25]. Even though a ToT pulse is created by simple discriminators, for these applications stability and very fast switching capability are paramount. Analog or mixed analog and digital ASIC designs are available and demonstrate high input flexibility, low power consuption and small size [26, 27].

However, whether ToT or MVT ToT approaches can be applied on multiplexed designs is an issue that hasn't been addressed so far. Such combination, if possible, can provide novel sollutions suitable for MR compatible PET inserts greatly reducing the material inside the MRI bore and subsequent power, cost and complexity of data transmission.

II. MATERIALS AND METHODS

A. SiPM

In order to be able to develop a novel scheme of data compression and high multiplexing ratio, it is necessary to first proceed in an offline analysis.. Initially the Hamamatsu s12642 MPPC [28], the model and considerations on which has already been described previously, was used. Apart from simulation, in previous work of our laboratory [29] an MR compatible PET detector prototype has been developed and characterized. Comprising of 16x16 1.6x1.6 mm^2 LYSO/GSO phoswich pixels and four 4x4 Hamamatsu s12642 MPPCs, this design demonstrates a 64:4 CDM ratio. In figure 6.7 a picture of the miniaturized prototype is shown, housing the MPPCs connected through a CDM network [30], alongside with a FFD (6.7.B) recorded using a ^{22}Na positron source. Also, a set of energy spectrums of a ^{22}Na for different pixels has been indexed (6.7.B), to give an estimation of the energy resolution.

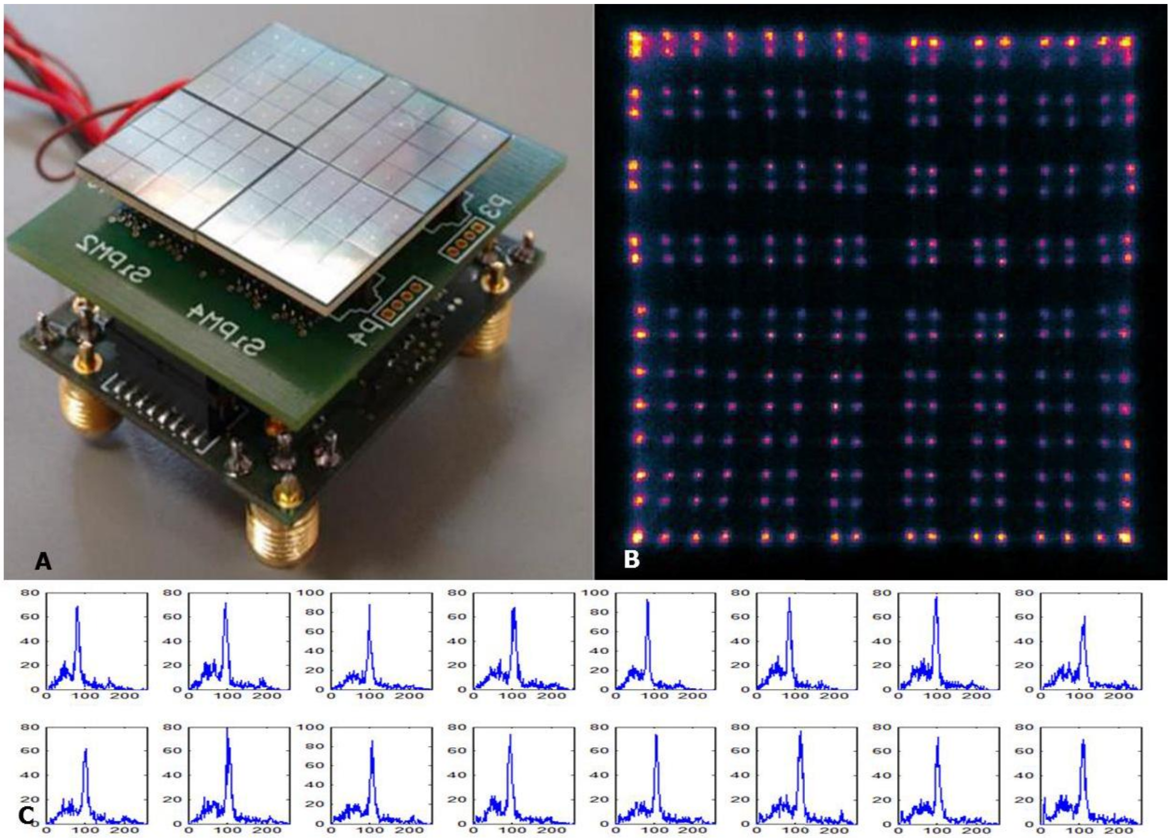

Figure 6. 7 MR compatible PET detector prototype housing 4 Hamamatsu s12642 MPPCs. (A) FFD, (B) photo of the prototype and (C) energy spectrums for the pixels noted in the FFD.

B. Multiplexing ratio considerations

From the aforementioned it can be derived that under given circumstances, the multiplexing ratio can be quite high [29]. However, the amount of SiPM pixels that will eventually be multiplexed is not only limited by signal quality considerations, which could eventually be resolved by careful design and intelligent processing. A non-negotiable limit is set by the inability of multiplexed photodetectors to resolve more than one event occurring before the scintillation pulse has finished. This time duration is called dead time. The sparse spatiotemporal character of PET signal is gradually becoming statistically dense as the size, or more precisely, the solid angle of independent readout elements as seen from the subject under study, becomes bigger.

In this context, a model (figure 6.10) must be built to estimate what the maximum multiplexed area (a^2) should be and apply this estimate used for detector design. A number of factors must be included: shape of model of the subject under study, which can be spherical (6.10.A) for single organ inserts (eg. brain) or ellipsoidal (6.10.B) for small animal ones; maximum solid angle (α'), resulting from the distance between the detector and the subject and the overall dimensions of FoV (r,d); detector sensitivity, controlling at a huge extent the rate at which events would occur; and finally, radiotracer dosage. These numbers should be combined with acquisition characteristics, such as detector dead time.

This calculation can furthermore answer most of the geometrical considerations necessary for the development of an insert. Issues such as necessary number of detectors or depth-of-interaction layers by quantifying the parallax error, can be addressed in the same context providing a unified analytical approach on the geometry of MR compatible PET inserts.

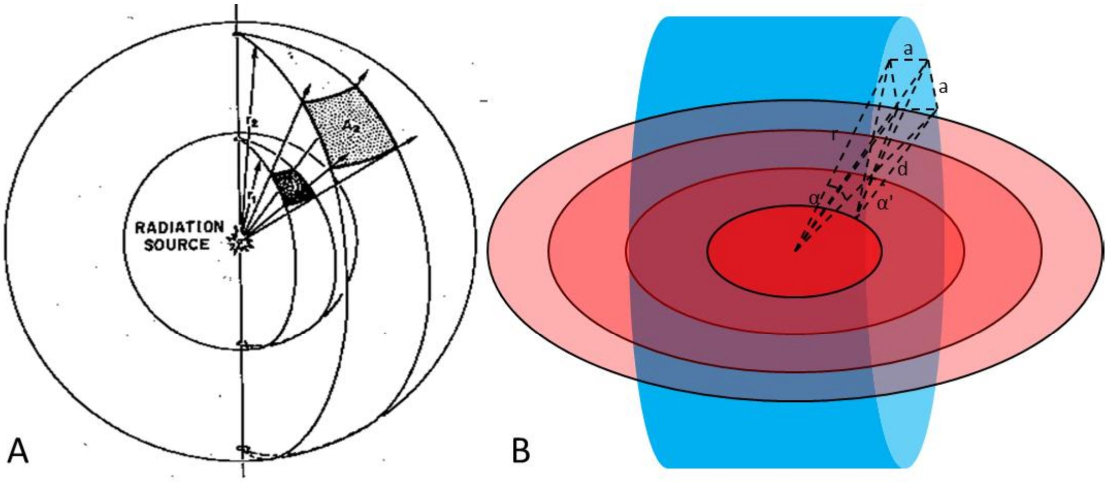

Figure 6. 8 Geometrical model of subjects under study for PET inserts: (A) single organ spherical model; and (B) small animal ellipsoidal one

C. ToT MVT study

Optimally MVT ToT measurement should demonstrate minimum deviation from the corresponding energy measurement, as well as multiplexing designs should allow precise reconstruction of the position of center of energy for each scintillation event. However, this is not always the case due to the noisy environment of the signal and circuit, along with the non ideal characteristics of the electronic elements. Nevertheless, significant preprocessing intelligence could imporve this precision. In this context, a series of experiments was conducted to evaluate this possibility. 1500 (X_1, X_2, Y_1, Y_2) from the MPPC prototype were recorded at very high sampling rate (20 GHz) and analyzed using Matlab.

Since unfortunately no coincidence data has been available, timing was not readily available to characterize the robustness of any algorithm that could be applied on MVT. For this reason, a biexponential model of the prerecorded pulses was reconstructed and noise was added. With this configurable dataset it has been possible to evaluate fitting schemes and demonstrate timing understanding of pulses of the form of the multiplexed ones.

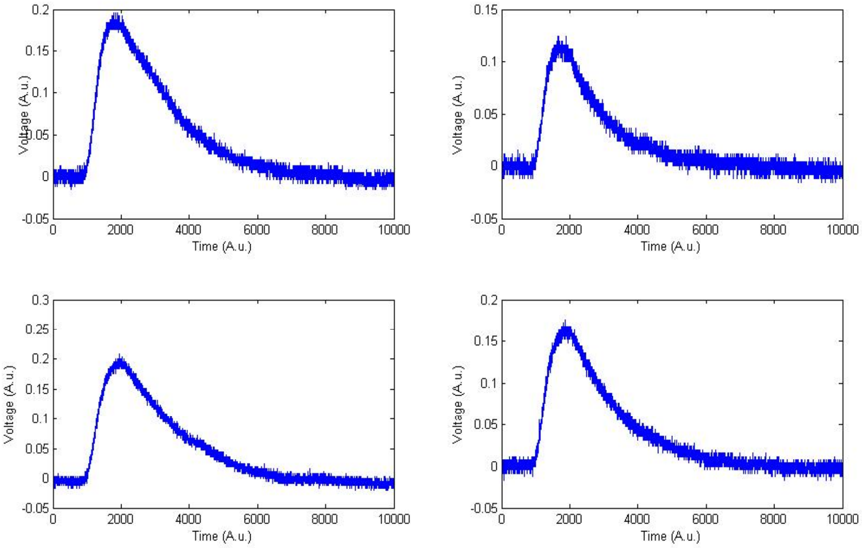

Figure 6. 9 A tetrad of (X_1, X_2, Y_1, Y_2) pulses from the MPPC prototype. The rising edge is relatively slow as compared to the model, due to paracitic capacitance.

Timing should be addressed in more detail, as it is known and expected that in the case of multiplexed pulses, several factors deteriorate the precision of measurement. Optimal timing strategies refer to detection of the first photon [5]. This is not easily possible in SiPM with limited PDE and circuits intended to provide optimal energy measurement, which is furthermore critical for position reconstruction in CDM scenarios. Usually timing is retrieved by setting a very low threshold or by applying a secondary circuit with very fast operational amplifiers; these solutions though are liable to saturation due to the high dark counts demonstrated by SiPM. Even if extensive statistical studies are performed and demonstrate an optimally low threshold, noise adds uncertainty, while the skew of the multiplexed area and circuit cannot be overridden. This means that such approach probably can't achieve timing at the region of 100 ps, which is the goal for novel PET designs, with the intention of applying time of flight (TOF) corrections [31].

III. RESULTS

D. Multiplexing ratio results

The dimensions and values that would characterize a PET insert scenario are analyzed and two different designs, a human brain PET and a small animal one have been explored. Initially, it is important to calculate the maximum solid angle that a square detector of side α will cover. According to literature [32], this is limited by the lowest order Taylor polynomial factor, equal to α^2/r^2. The radiation activity this solid angle will receive corresponds to the steradian it covers as compared to the total spherical area of 4π steradians around the subject. A ratio of this radiation activity will be captured by the detector, depending on its sensitivity.

It is important to confirm that the area α^2 will not be too big so that no events will occur within the dead time of the detector often. Given that the statistical nature of intervals between pulses is Poissonian with mean λ corresponding to the average rate of captured events, we can calculate how much the maximum average rate λ_{max} is so that for 99.9% or 99% of the captured γ the next γ will not occur within the Δt dead detector time (equations 6.3).

$$P(k) = \frac{\lambda^k e^{-\lambda}}{k!} \Rightarrow 0.001 = \frac{\lambda^2 e^{-\lambda}}{2} \Rightarrow \lambda_{max} = 0.0438/\Delta t$$

equations 6.3

$$P(k) = \frac{\lambda^k e^{-\lambda}}{k!} \Rightarrow 0.01 = \frac{\lambda^2 e^{-\lambda}}{2} \Rightarrow \lambda_{max} = 0.1324/\Delta t$$

The main factor controlling the dead time of the detector is the duration of scintillation pulse. In the case of LYSO, this dead time can be set at around 400 ns, expecting for total baseline restoration, while literature [10] provides figures for different depths, which can be extrapolated for size around 10 mm and the superior packing fraction of SSLE. LYSO intrinsic radioactivity is providing a lot less counts as compared to the ones expected from a medical or experimental scenario. In this context, this radiation as well as background counts are not included in the calculation.

The rate λ_{max} corresponds to the captured events, thus should be divided by the sensitivity percentage and compared with the expected average rate. This is a product of the maximum radiation activity limited by the maximum radiotracer dose and the solid angle the detector occupies as a ratio to the sphere. The maximum total activity of the brain PET insert is calculated by the maximum FDG radiotracer dosage for a human more than 90 kg, extrapolated for the percentage that is metabolized in the brain [33]. All this is wrapped up in equation 6.4 and table 6.1.

$$2 \times A \times s \times \frac{\alpha^2}{4\pi r^2} \leq \lambda_{max} \overset{99.9\%}{\Longleftrightarrow} \alpha \leq \sqrt{\frac{0.0438 \times 4\pi r^2}{2 \times A \times \Delta t \times s}}$$

equations 6.4

$$2 \times A \times s \times \frac{\alpha^2}{4\pi r^2} \leq \lambda_{max} \overset{99\%}{\Longleftrightarrow} \alpha \leq \sqrt{\frac{0.1324 \times 4\pi r^2}{2 \times A \times \Delta t \times s}}$$

For the calculation of DoI levels, the relation between FoV and internal detector radius gives an extreme absolute value of the parallax error, given that the detector elements have a radial direction. The theoretical trajectory of a γ occurring at the edge of field provides the maximum angle of parallax error (figure 6.20). The γ trajectory creates an orthogonal triangle with r, l sides. The angle α, for which $\cos\alpha = l/r$, is equal to the angle between the trajectory and the tangent, as acute angles with vertical sides. Given that the crystal depth d is much smaller than the radius of the detector, the arc c′ roughly coincides with the straight line c and is practically orthogonal to the sector d. Given these assumptions it is now possible to calculate the maximum number of DoI layers, by comparing the section c with the pixel side p, as can be seen in equation 6.5.

$$\mathrm{c} = \frac{\mathrm{d}}{\tan\cos^{-1}(^{l}/_{r})}, \quad n_{DoI} = \lfloor \frac{c}{p} \rfloor \qquad \text{equation 6.5}$$

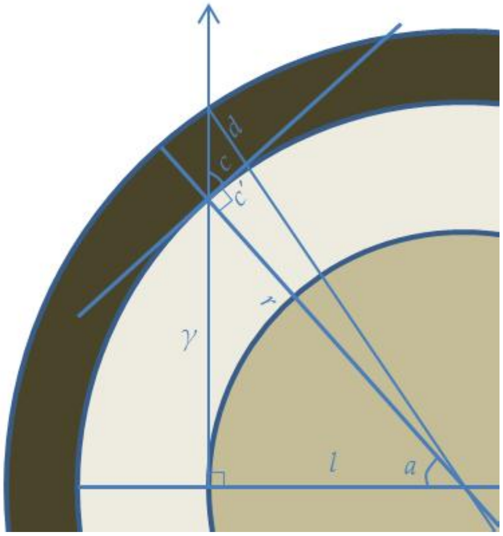

Figure 6. 10 Section of detector ring to support the calculation of necessary DoI levels for elimination of parallax error.

To build a cylindrical insert, it must be taken into account that the diameter D of which is dictated by the dimensions of the MRI bore and the thickness of the whole module (s) including the SiPM, circuit, scintillator and shielding. This has been set at 22 mm, in the context of an initial study. The height of the cylinder (h), since not the whole length of the bore is necessary, is calculated by the dimensions of the desired field of view. To evaluate the number of modules per ring we follow the equations 6.6.

$$\mathrm{N_{detectors}} = \left\lfloor \frac{2\pi}{\sin^{-1}\left(\frac{a}{D-2*s}\right)} \right\rfloor, \ \mathrm{N_{rings}} = \left\lceil \frac{h}{a} \right\rceil \qquad \text{equation 6.6}$$

A hemispherical insert, however, includes a lot more complicated studies, as covering this type of area with square detectors available doesn’t have a single optimal solution. Different approaches are being tried [34, 35]. Nevertheless, estimation on the maximum amount of detector elements can be made by comparing the resulting area with the calculated area of a hemisphere.

Table 6.1 Metrics for the dimensions of inserts for two different realistic scenarios

	Human brain PET insert	**Small animal PET insert**
Max total activity (A)	239 MBq[36]	185MBq[36]
Internal insert radius (r)	90 mm[37]	75 mm (from dimensions of MR bore and PET detector)
FoV dimensions (l,h)	70 mm[38]	25 mm, 200 mm (size of adult rat)
Pixel area (p^2)	2.56 mm^2	1.6 mm^2
Detector dead time (Δt)	350 ns	
Sensitivity (s)	~12%[10]	
Scintillator depth (d)	10 mm	
Detector side (a)	14.96 mm for 0.1% pileup, 26.01 mm for 1% pileup	14.11 mm for 0.1% pileup, 24.5 mm for 1% pileup
Number of DoI levels	7	3
Number of detector elements	227 for 0.1% pileup, 75 for 1% pileup	495 for 0.1% pileup, 162 for 1% pileup

The calculated side of detector for 99.9% detection coincides roughly with the dimensions of the 4x4 SiPM arrays simulated and experimented with. Higher multiplexing ratios include the danger of losing a big number of events due to pile up. The DoI levels calculated are a theoretical maximum occurring by the solution of the geometrical structure, for uniform size of voxels throughout the FoV. However, any amount of layers will improve resolution.

E. *ToT study results*

Given the relatively small size of maximum CDM area, it is paramount to demonstrate that it is possible to use some ToT solution for CDM pulses. By analyzing the multitude of recorded tetrads, it was possible to acquire ToT pulses. A number of different ToT and MVT scenarios were attempted and will be presented in the next paragraphs. In figure 6.11, an outline of these scenarios is demonstrated and will be expanded in the next paragraphs.

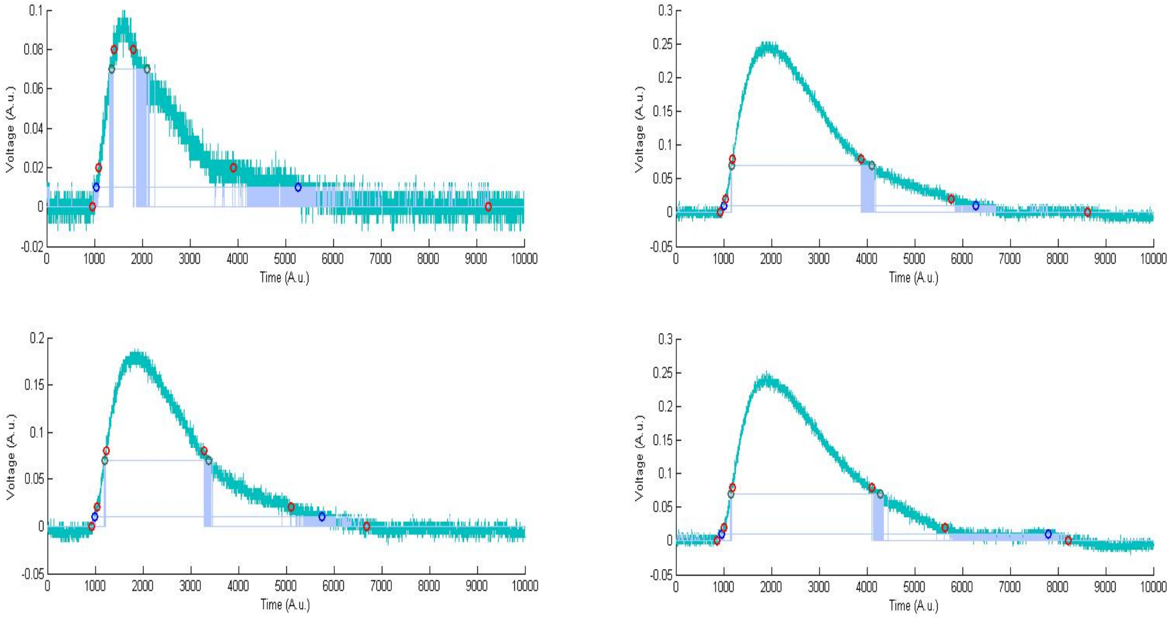

Figure 6.11 A random tetrad of CDM pulses. Two ToT waves for different threshold are also plotted, along with retrieved edges for energy calculation, for four different scenarios. Blue represent a low threshold ToT, green a high one, and red are the noise switching activity estimators.

Initially, the voltage was set at the border of noise, so that false triggering can be avoided while event onset can be traced. In order to evaluate the precision of measurement a comparison between the integrated pulse content, equivalent to energy, with the corresponding ToT surrogate, resulting from multiplication of ToT duration with the threshold, is plotted for the four CDM channels. As can be seen in figure 6.12, there is a rough relation between the recorded integral of the pulse that corresponds to its energy and the equivalent ToT value. However, the uncertainty of measurement is so extensive, that not only such measurement can be used for a multiplexed solution, but can’t even provide a reliable estimation for energy of pulse. The measurement is compromised basically by the presence of noise and not perfect baseline restoration after the pulse. This can be evaluated by the extensive switching at the beginning and ending of the ToT signal.

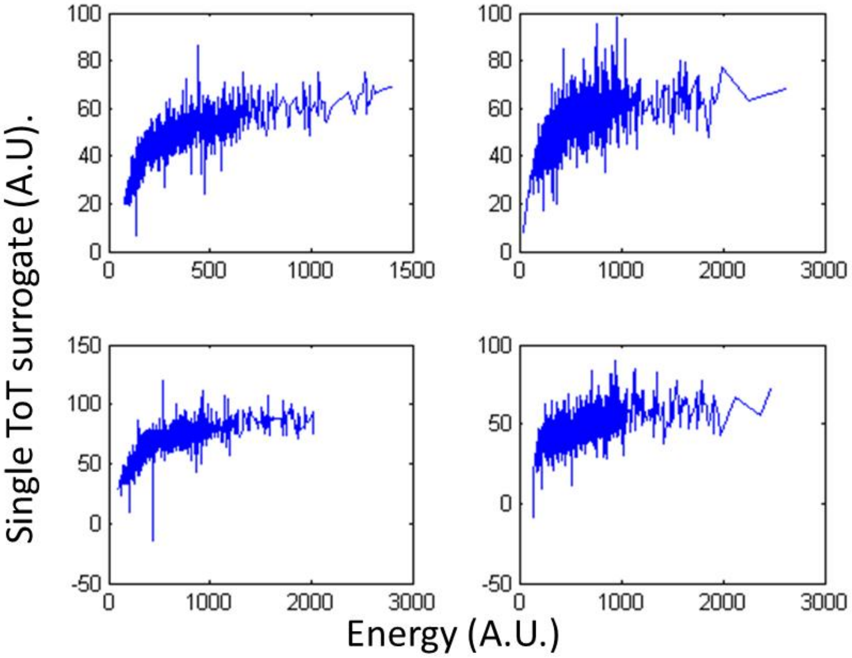

Figure 6.12 Single ToT at the border of noise as compared to measured energy of pulses for four CDM channels (blue point scenario).

In order to provide a better energy estimation, a different threshold was chosen at a higher value. This value was elected as being high enough to have more brief switching area, lowering the uncertainty of measurement.. The same approach for an energy measurement evaluation for four channels can be found in figure 6.13. There is a clear improvement, even though unfortunately with such threshold no precise timing estimation can be made.

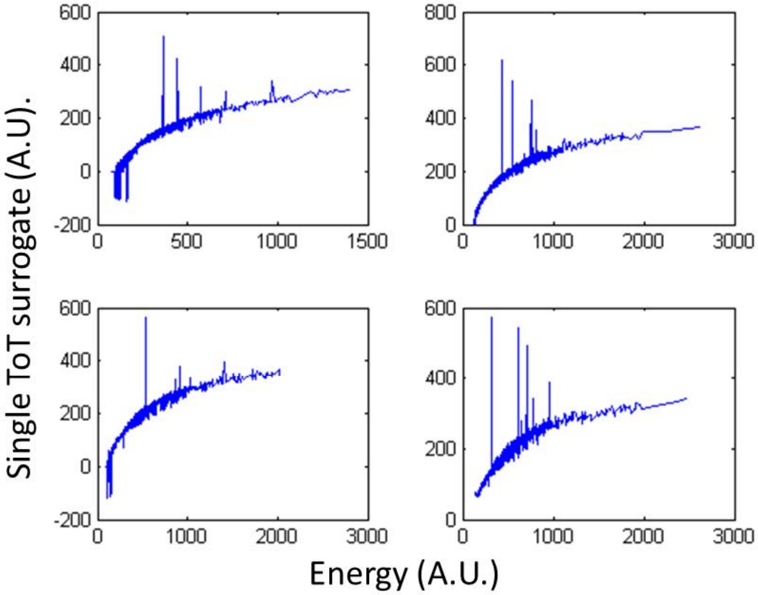

Figure 6.13 Single ToT out of noise estimator as compared to measured energy of pulses for four CDM channels (green point scenario).

However, if one would intend to acquire both energy and timing, an MVT approach with at least two thresholds would be favorable. Both those channels provide information that can be harnessed. Yet, an addition of the ToT durations per pulse deteriorates the energy measurement. This might sound absurd, since more information should provide better precision; however in principle, as can be observed in figure 6.14, measurement error is a combination of the errors of the two previous approaches.

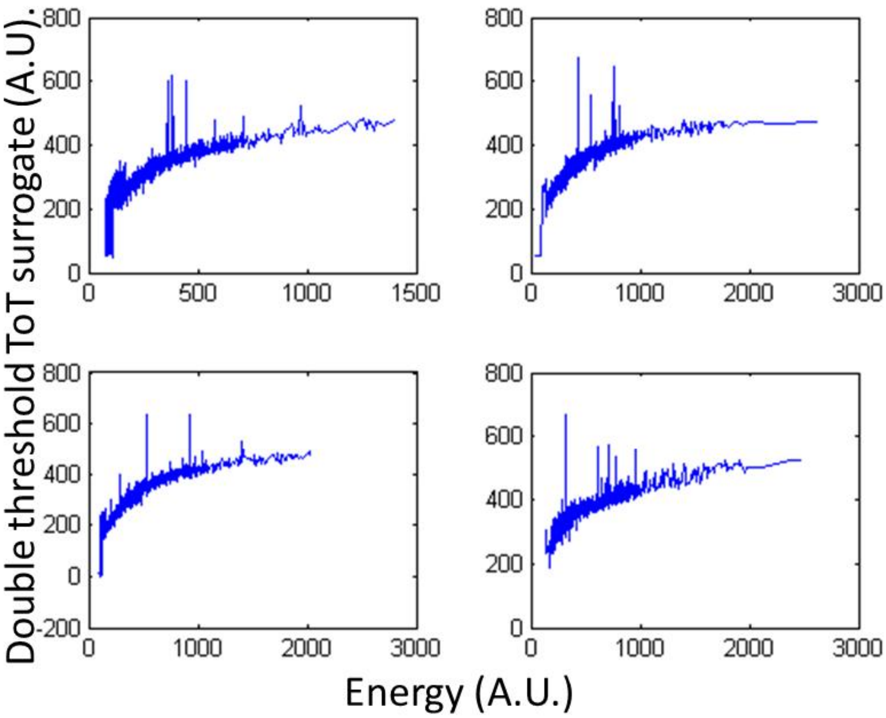

Figure 6.14 Double threshold MVT ToT estimator as compared to measured energy of pulses for four CDM channels (green+blue point scenario).

Since those methods are not satisfactory for the application of MVT ToT on CDM architectures, a new approach is necessary. The main idea sprouts from quantifying the characteristics of noise. In the acquisition under study, the noise band corresponds to approximately 2.5% of the average maximum scintillation event pulse value. This, from experience with different settings, is a realistic scenario. By analyzing its statistical characteristics (figure 6.15), noise is found to follow normal distribution. This means that if a big enough statistical sample can be gathered around a given voltage, the percentage of values higher or lower than this voltage correspond to the relation of that value with the mean of the noise distribution. The mean of noise, though, is the signal and that relation can be quantified following the cumulative distribution function of the normal distribution [39].

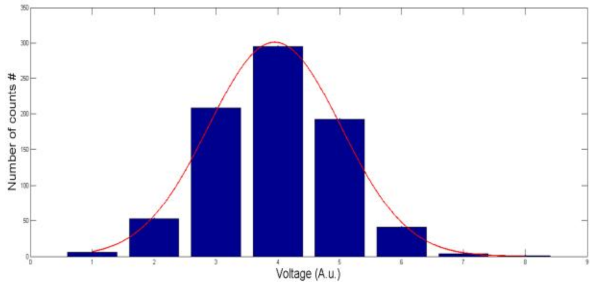

Figure 6. 15 Histogram of a random sample of recorded noise

Expanding this approach, if the signal follows a known trajectory over time, like the biexponential model, enough information exist to estimate more points of the signal, by evaluating the statistical characteristics of switching area (figure 6.16). Indeed, the pulses where found to follow roughly that model with a slower rising coefficient than anticipated, around 12 ns, due to the capacitance of SiPM and circuit. As can be confirmed from the figure 6.16.A, even under this circumstance this area is quite short (approximately 3 ns) at the rising first half and provides enough measurements only at very fast sampling rates. If in this scenario we include a realistic rising time, such as the 300 ps of NINO [26], as a golden standard, it is understandable that no more than two values might be possible at the rising part. However, the slow return provides a lot more statistical samples, as it can be found to last as much as 20 ns for the higher threshold and 50 ns for the lower one (figure 6.16.B).

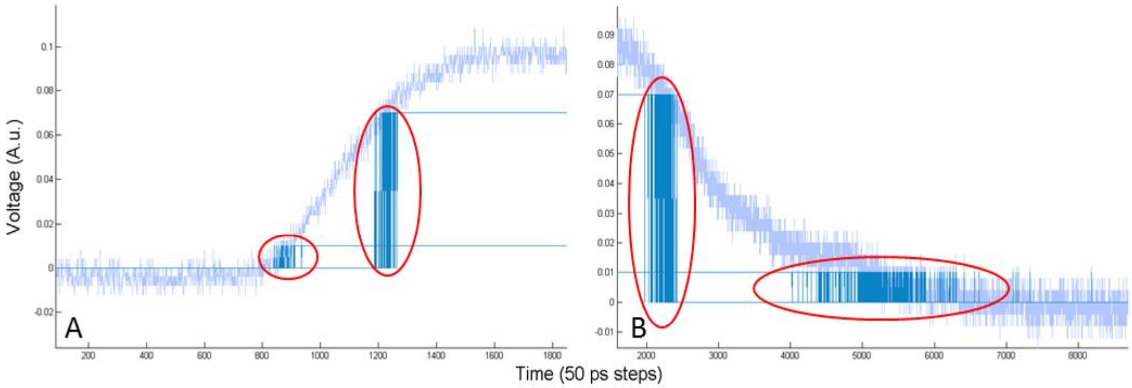

Figure 6. 16 Demonstration of switching areas (red circles) where the pulse crosses the thresholds for rising(A) and falling (B) sides of the pulse

As can be seen in figure 6.11, by using the statistical characteristics of noise it was possible to retrieve as much as 10 points from 2 ToT measurements. Applying this algorithm, the evaluation of energy measurement can be found in figure 6.17. This is visibly better than the previous measurements even though a few outliers, approximately 0.03% of the measurements, related to pile up of pulses or very low energy, can't be correctly measured. By fitting the resulting energy- noise corrected double voltage surrogate curve, it is possible to retrieve the deviation of measurement and quantify it. If then we compare that value with the range of energies, it is possible to retrieve the average deviation σ, normalized to the range of energy values, approximately at 0.0125±0.005. By applying the error propagation function to the CDM equations, the uncertainty of position measurement is less than 1%. Uncertainty of position is very small in this context, demonstrating that a SiPM based detector could be resolved using CDM and MVT ToT with noise correction. In the scenario described before, a 64:4 array with 16x16 pixels of 1.6 mm^2, pixel resolvability (equation 3.3) is expected to deteriorate by only approximately 8%.

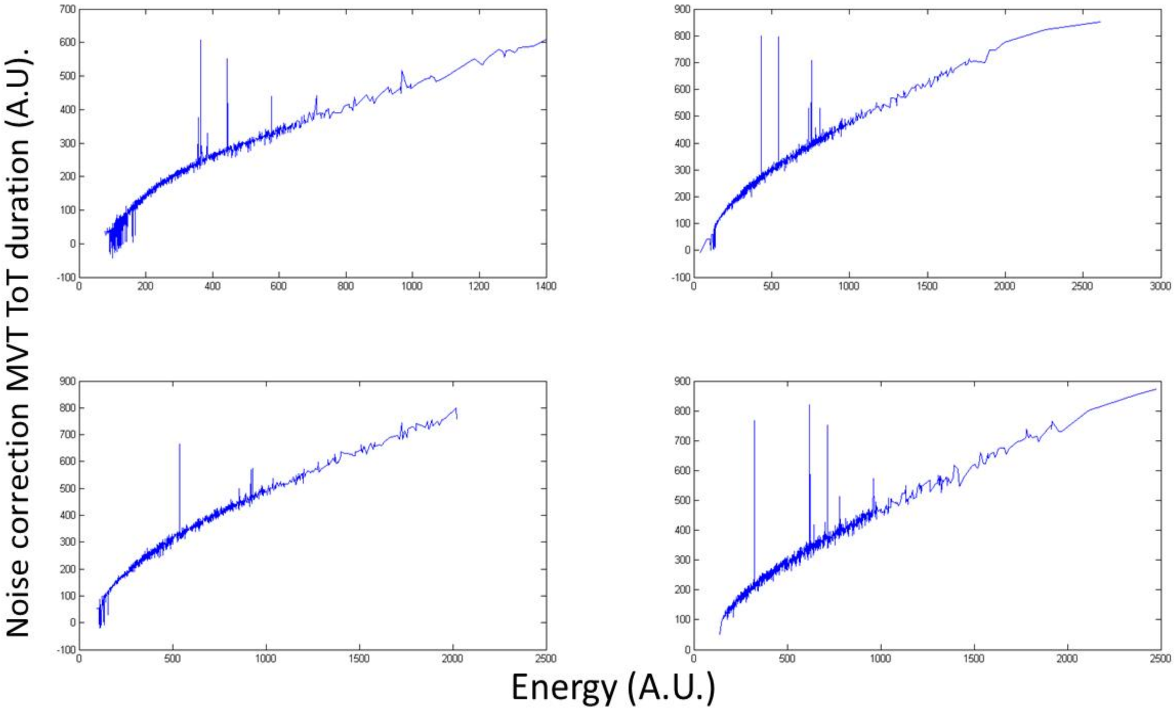

Figure 6. 17 Noise correction MVT ToT estimator as compared to measured energy of pulses for four CDM channels (green+blue+red point scenario).

F. Timing results

A study on quality of timing measurement was also performed. In previous works [25] it has been proposed that fitting a line on the MVT ToT edges can retrieve relatively good timing information. Given that more than two points have been established, it is possible to fit higher order functions. As can be seen in figure 6.18, a fourth order polynomial fit corresponds very well to the biexponential curve, as the four most significant Taylor polynomial factors already fit very well any function comprising of combinations of exponentials.

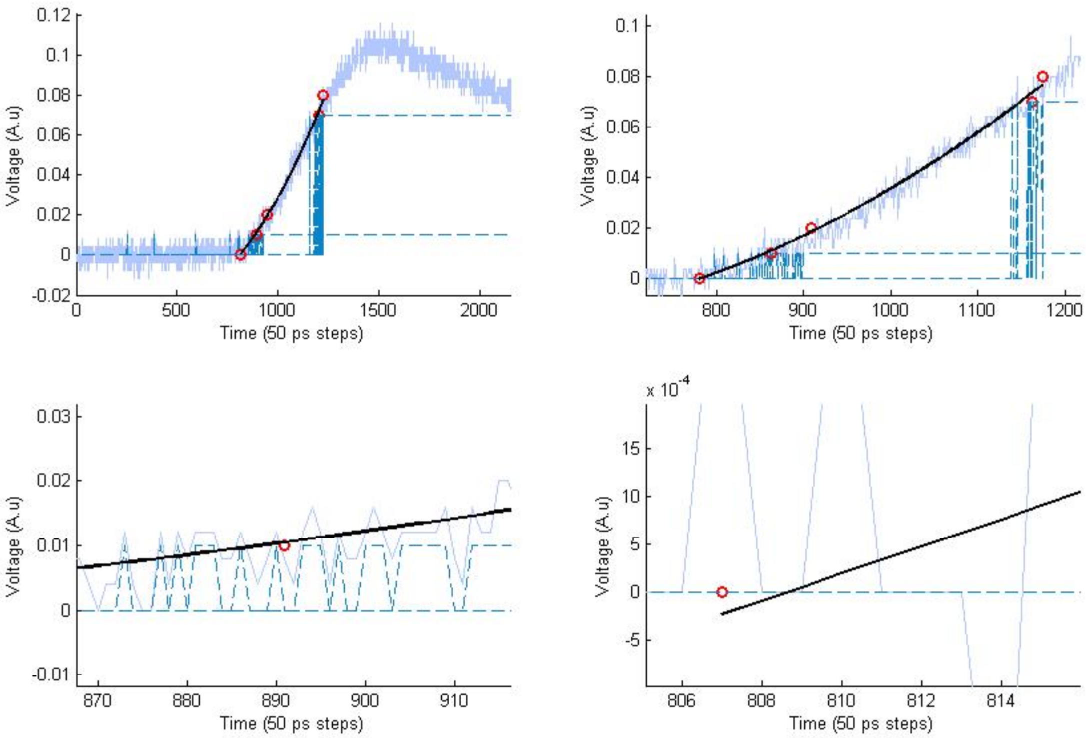

Figure 6.18 Four snapshots of polynomial fitting of the real scintillation pulse demonstrating the fast edge, noise correction estimators and corresponding fitted model along with details on the low threshold and zero crossing of the constructed polynomial model.

By applying this process to the noisy biexponential model that we constructed it was possible to receive some statistics on the distribution of the measured point as compared to the known timing of the simulated scintillation event. The distribution of the histogram can be seen in figure 6.19. Since this can't fitted to a normal function, the mean absolute deviation (MAD) was used. MAD for the polynomial fitting approach corresponds to approximately 200 ps. This of course doesn't mean that the exact timing of the event can be traced to such precision, as the delays and filtering of the circuit and skew of SiPM can't be evaluated. Nevertheless, this technique is improving the retrieved timing as compared to direct thresholding, the MAD of which was measured using the same pulses at around 350 ps.

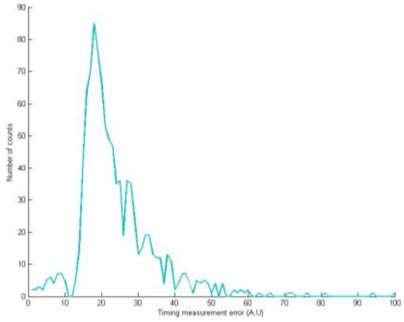

Figure 6. 19 Timing error distribution, as resulting from simulation

However, there is the possibility of applying this study to different SiPMs as for instance, the 4x4 J-series SiPM of SensL [40]. This integrated circuit shows similar characteristics with the MPPC. However, three elements make it favorable for multiplexing approaches for MR compatible designs; the one is its MR compatibility; also, the silicon design of this device allows overvoltage lower than most SiPM of the market, in the order of 30V; while finally, it demonstrates not only one signal output, but two. From each silicon pixel a slow signal is provided, representing the formerly described energy measurement, but furthermore a different output carries a fast signal of duration of few nanoseconds, that demonstrates the time of arrival. These outputs can be directly added and directed to fast electronics for timing characterization, providing a very light-weight alternative for timing that solves the issue of problematic timing characterization due to low-pass filtering and could be applied in ToF scenarios [41].

IV. CONCLUSIONS

By performing a geometrical study, it has been possible to establish what the size limitations for the number of multiplexed channels are. In the light of this result, it has been paramount to demonstrate compatibility between a ToT strategy and CDM. On the other hand, knowing those limits, allows quantification of the uncertainty added by such combination. Calculation of DoI layers is equally important and deterioration of pixel/DoI resolvability can be addressed from this framework.

Nevertheless, this study has demonstrated that the energy content of CDM channels, is correctly converted in noise corrected double voltage (NCDV) ToT surrogates and event location can be accurately reconstructed. The necessary addition of fast discriminator ASICs in the front end is one that doesn’t affect significantly the size, power consumption and MR compatibility of the front end, while acting as driver for the transmission of data to the back-end. The number of transmission channels will have to be studied in detail, but is expected to lower greatly information channel occupation, as compared to transmission of the analog channels. Logic at the receiving side, as for instance with the application of FPGAs, could provide the necessary noise evaluation and calibration routines and facilitate precise threshold setting and NCDV ToT edge synthesis. Furthermore, TDCs could be included in such a design.

The precision of conversion is enough for accurate characterization of the energy and position of events in a scenario of SSLE hexagonal crystals with two layers of DoI. In this context the combined data compression approach studied can be readily applied. On the other hand, if deemed necessary, it could be possible to add more thresholds in order to further enhance the precision of results.

Timing resolution is slightly improved as compared with direct thresholding of the pulses, even if this is set at a very low voltage within noise. However, this is only a simulated estimation and doesn't take into account circuit and SiPM delays. Given the dimensions mentioned in table 6.1, none of these solutions would be good enough for TOF application, due to the small size of the field of view (FOV) that requires sublime timing in the order of few tens of picoseconds. Nevertheless, this obstacle could be anyway overtaken by the application of a SiPM like the J-series of SensL, which provides a fast output pulse with known timing characteristics and wouldn't deteriorate significantly material usage or MR compatibility.

V. REFERENCES

[1] Thompson, C. J., Yamamoto, Y. L., & Meyer, E. (1979). Positome II: A high efficiency positron imaging device for dynamic brain studies. IEEE Transactions on Nuclear Science, 26(1), 583-589.

[2] Hoffman, E. J., Phelps, M. E., Huang, S. C., Plummer, D., & Kuhl, D. E. (1982). Evaluating the performance of multiplane positron tomographs designed for brain imaging. IEEE Transactions on Nuclear Science, 29(1), 469-473.

[3] Yamaya, T., Inaniwa, T., Minohara, S., Yoshida, E., Inadama, N., Nishikido, F., ... & Murayama, H. (2008). A proposal of an open PET geometry. Physics in medicine and biology, 53(3), 757.

[4] España, S., Marcinkowski, R., Keereman, V., Vandenberghe, S., & Van Holen, R. (2014). DigiPET: sub-millimeter spatial resolution small-animal PET imaging using thin monolithic scintillators. Physics in medicine and biology, 59(13), 3405.

[5] Van Der Laan, D. J., Maas, M. C., Schaart, D. R., Bruyndonckx, P., Léonard, S., & van Eijk, C. W. (2006). Using Cramér-Rao theory combined with Monte Carlo simulations for the optimization of monolithic scintillator PET detectors. IEEE transactions on nuclear science, 53(3), 1063-1070.

[6] Wehner, J., Weissler, B., Dueppenbecker, P., Gebhardt, P., Schug, D., Ruetten, W., ... & Schulz, V. (2014). PET/MRI insert using digital SiPMs: Investigation of MR-compatibility. Nuclear Instruments and Methods in Physics Research Section A: Accelerators, Spectrometers, Detectors and Associated Equipment, 734, 116-121.

[7] Weissler, B., Gebhardt, P., Düppenbecker, P., Goldschmidt, B., Salomon, A., Schug, D., ... & Schumacher, K. (2012, October). Design concept of world's first preclinical PET/MR insert with fully digital silicon photomultiplier technology. In Nuclear Science Symposium and Medical Imaging Conference (NSS/MIC), 2012 IEEE (pp. 2113-2116). IEEE.

[8] Vagner, I. D., Lembrikov, B. I., & Wyder, P. R. (2013). Electrodynamics of magnetoactive media (Vol. 135). Springer Science & Business Media.

[9] Saveliev, V. (2010). Silicon photomultiplier-new era of photon detection. INTECH Open Access Publisher.

[10] Sportelli, G., Ahmad, S., Belcari, N., Bisogni, M., Camarlinghi, N., Di Pasquale, A., ... & Del Guerra, A. (2016). The TRIMAGE PET Data Acquisition System: initial results. IEEE Transactions on Nuclear Science.

[11] Anger, H. O. (1958). Scintillation camera. Review of scientific instruments, 29(1), 27-33.

[12] Siegel, S., Silverman, R. W., Shao, Y., & Cherry, S. R. (1996). Simple charge division readouts for imaging scintillator arrays using a multi-channel PMT. IEEE Transactions on Nuclear Science, 43(3), 1634-1641.

[13] Goertzen, A. L., Zhang, X., McClarty, M. M., Berg, E. J., Liu, C. Y., Kozlowski, P., ... & Thompson, C. J. (2013). Design and performance of a resistor multiplexing readout circuit for a SiPM detector. IEEE Transactions on Nuclear Science, 60(3), 1541-1549.

[14] Olcott, P. D., Glover, G., & Levin, C. S. (2013). Cross-strip multiplexed electro-optical coupled scintillation detector for integrated PET/MRI. IEEE Transactions on Nuclear Science, 60(5), 3198-3204.

[15] Tornai, M. P., Germano, G., & Hoffman, E. J. (1994). Positioning and energy response of PET block detectors with different light sharing schemes. IEEE transactions on nuclear science, 41(4), 1458-1463.

[16] Thompson, C. J., & Goertzen, A. L. (2011). Evaluation of a 16: 3 signal multiplexor to acquire signals from a SPM array with dual and single layer LYSO crystal blocks. IEEE Transactions on Nuclear Science, 58(5), 2175-2180.

[17] Chinn, G., Olcott, P. D., & Levin, C. S. (2013). Sparse signal recovery methods for multiplexing PET detector readout. IEEE transactions on medical imaging, 32(5), 932-942.

[18] Candès, E. J., Romberg, J., & Tao, T. (2006). Robust uncertainty principles: Exact signal reconstruction from highly incomplete frequency information. IEEE Transactions on information theory, 52(2), 489-509.

[19] Olcott, P., Kim, E., Hong, K., Lee, B. J., Grant, A. M., Chang, C. M., ... & Levin, C. S. (2015). Prototype positron emission tomography insert with electro-optical signal transmission for simultaneous operation with MRI. Physics in medicine and biology, 60(9), 3459.

[20] Glodo, J., Moses, W. W., Higgins, W. M., Van Loef, E. V. D., Wong, P., Derenzo, S. E., ... & Shah, K. S. (2005). Effects of Ce concentration on scintillation properties of LaBr/sub 3: Ce. IEEE Transactions on Nuclear Science, 52(5), 1805-1808.

[21] Lichard, P., Konstantinou, G., Vilanueva, A. V., & Palladino, V. (2014). Performance evaluation of multiple (32 channels) sub-nanosecond TDC implemented in low-cost FPGA. Journal of Instrumentation, 9(03), C03013.

[22] Kipnis, I., Collins, T., DeWitt, J., Dow, S., Frey, A., Grillo, A., Johnson, R., Kroeger, W., Leona, A., Luo, L. and Mandelli, E. (1997). A time-over-threshold machine: the readout integrated circuit for the BABAR Silicon Vertex Tracker. IEEE Transactions on Nuclear Science, 44(3), pp.289-297.

[23] Jakubek, J. (2011). Precise energy calibration of pixel detector working in time-over-threshold mode. Nuclear Instruments and Methods in Physics Research Section A: Accelerators, Spectrometers, Detectors and Associated Equipment, 633, S262-S266.

[24] Kalisz, J. (2003). Review of methods for time interval measurements with picosecond resolution. Metrologia, 41(1), 17.

[25] Deng, Z., & Xie, Q. (2015). Quadratic Programming Time Pickoff Method for Multivoltage Threshold Digitizer in PET. IEEE Transactions on Nuclear Science, 62(3), 805-813.

[26] Anghinolfi, F., Jarron, P., Martemiyanov, A. N., Usenko, E., Wenninger, H., Williams, M. C. S., & Zichichi, A. (2004). NINO: an ultra-fast and low-power front-end amplifier/discriminator ASIC designed for the multigap resistive plate chamber. Nuclear Instruments and Methods in Physics Research Section A: Accelerators, Spectrometers, Detectors and Associated Equipment, 533(1), 183-187.

[27] Moraes, D., Schmidt, B., Riegler, W., Rivetti, A., Anghinolfi, F., Jarron, P., & Deval, P. (2000). CARIOCA-a fast binary front-end implemented in 0.25$\ mu $ m CMOS using a Novel current-mode technique for the LHCb muon detector (No. LHCb-2000-093). CERN-LHCb-2000-093.

[28] Hamamatsu MPPC TSV reference sheet, http://www.nuclear.gla.ac.uk/~jrma/A2/Tagger/NewFPD/SiPMT/KSX-I50014-E_S12642%20Series%20(3mm%E2%96%A1-TSV%E3%83%BCArray).pdf, retrieved 11.01.2017

[29] Chil, R., Konstantinou, G., Desco, M., & Vaquero, J.J., (2016) Compact, MR Compatible SiPM Small Animal PET DOI Detector, IEEE NSS/MIC proceedings

[30] Popov, V., Majewski, S., & Welch, B. L. (2006). A novel readout concept for multianode photomultiplier tubes with pad matrix anode layout. Nuclear Instruments and Methods in Physics Research Section A: Accelerators, Spectrometers, Detectors and Associated Equipment, 567(1), 319-322.

[31] Gundacker, S., Auffray, E., Frisch, B., Jarron, P., Knapitsch, A., Meyer, T., ... & Lecoq, P. (2013). Time of flight positron emission tomography towards 100ps resolution with L (Y) SO: an experimental and theoretical analysis. Journal of Instrumentation, 8(07), P07014.

[32] Mathar, R. J. (2014). Solid angle of a rectangular plate. Max-Planck Institute of Astronomy, Königstuhl, 17, 69117.

[33] Kaushik, A., Jaimini, A., Tripathi, M., D'Souza, M., Sharma, R., Mishra, A. K., ... & Dwarakanath, B. S. (2013). Estimation of patient dose in 18 F-FDG and 18 F-FDOPA PET/CT examinations. Journal of cancer research and therapeutics, 9(3), 477.

[34] Tashima, H., Ito, H., & Yamaya, T. (2013, October). A proposed helmet-PET with a jaw detector enabling high-sensitivity brain imaging. In Nuclear Science Symposium and Medical Imaging Conference (NSS/MIC), 2013 IEEE (pp. 1-3). IEEE.

[35] Yoshida, E., Yamaya, T., Watanabe, M., Kitamura, K., Kobayashi, A., Hasegawa, T., ... & Murayama, H. (2006). Design and initial evaluation of a 4-layer DOI-PET system: the jPET-D4. Japanese Journal of Medical Physics (Igakubutsuri), 26(3), 131-140.

[36] Jagoda, E. M., Vaquero, J. J., Seidel, J., Green, M. V., & Eckelman, W. C. (2004). Experiment assessment of mass effects in the rat: implications for small animal PET imaging. Nuclear medicine and biology, 31(6), 771-779.

[37] Poston A. (2000). Static adult human physical characteristics of the adult head. Department of Defense Human Factors Engineering Technical Advisory Group (DOD HFE TAG).

[38] Blinkov, S.M. and Glezer, I.I. (1968). The Human Brain in Figures and Tables. A Quantitative Handbook, New York: Plenum Press

[39] Krishnamoorthy, Kalimuthu (2006). Handbook of Statistical Distributions with Applications. Chapman & Hall/CRC. ISBN 1-58488-635-8.

[40] http://sensl.com/downloads/ds/DS-MicroJseries.pdf, retrieved 13.02.2017

[41] Dolinsky, S., Fu, G., & Ivan, A. (2013, October). Timing resolution performance comparison for fast and standard outputs of SensL SiPM. In Nuclear Science Symposium and Medical Imaging Conference (NSS/MIC), 2013 IEEE (pp. 1-6). IEEE.

Chapter 7: Demonstration of optical wireless applicability for a PET/SPECT insert front-end

I. INTRODUCTION

A. Transmission of data

After having finalized the study of detector design, the next goal is to develop a viable alternative for the transmission of data from the detector to a preprocessing unit. While it has been demonstrated that some signal processing can take place using analog ASICs [1], characterized by their low power consumption and enhanced magnetic field immunity, it is expected that eventually digitalization should happen. Optimally, this should happen outside the strong magnetic field, were not only space specifications are not so narrow, but digital data quality is guaranteed, due to the absence of spurious, magnetic field induced, eddy currents [2].

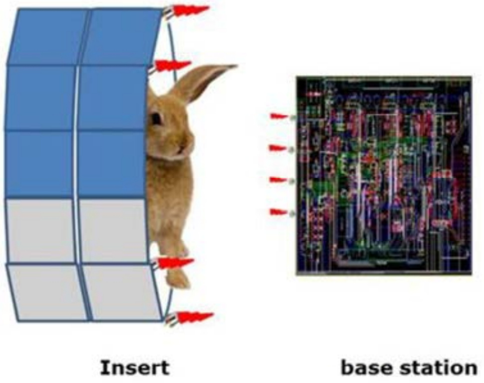

Figure 7. 1 Separation of the PET detector in a front end inserted in the MR bore (left) and a base station away from the magnetic field (right)

Thus, developing an approach for data transmission out of the MR bore (figure 7.1) and away from the magnetic field for the aforementioned reasons, need not be limited to PET inserts. Alternative interconnection techniques exist and are being studied [3], applying optical fibers. This approach has numerous advantages, apart from applying a non-magnetic material for data transmission. An electro-optically coupled insert doesn't share the same ground with the MRI. This means that with a floating ground, it is practically transparent to the field, minimizing the aberrations its existence could cause to the MRI signal.

B. SPECT inserts

Inevitably, such question is not relative only to MR compatibility of PET inserts. While this has been the main focus of the dissertation, by answering this question it is possible to also expand this study to other type of inserts, namely MR compatible SPECT approaches. Those are also possible and currently being researched (figure 7.2.A), with the same motivation of multimodality [4]. For both designs, necessity for cooling due to the high consumption of the insert part and transmission of a big number of channels create difficulties on the design. For both designs, a standard is to use photodetectors coupled to scintillators, even though the range of energies is different for SPECT. Both approaches require the administration of a radiotracer, even though for SPECT it is not β+ decaying atoms, but ones that provide directly γ [5]. The main difference between the two approaches is that while PET requires superior timing measurement to perform coincidence or even time-of-flight, in SPECT lines-of-response (LORs) are attributed by the application of collimators (figure 7.2.B). This feature drives the sensitivity of this technique an order of magnitude lower [6], but also makes it more applicable for scenarios where detector rings are not possible, such as intraoperative ones [7]. Furthermore, since time is not a critical factor, pipelining the data acquisition system, already from the analog pulses, is applicable. Given the similarities between PET and SPECT inserts, this study can include both.

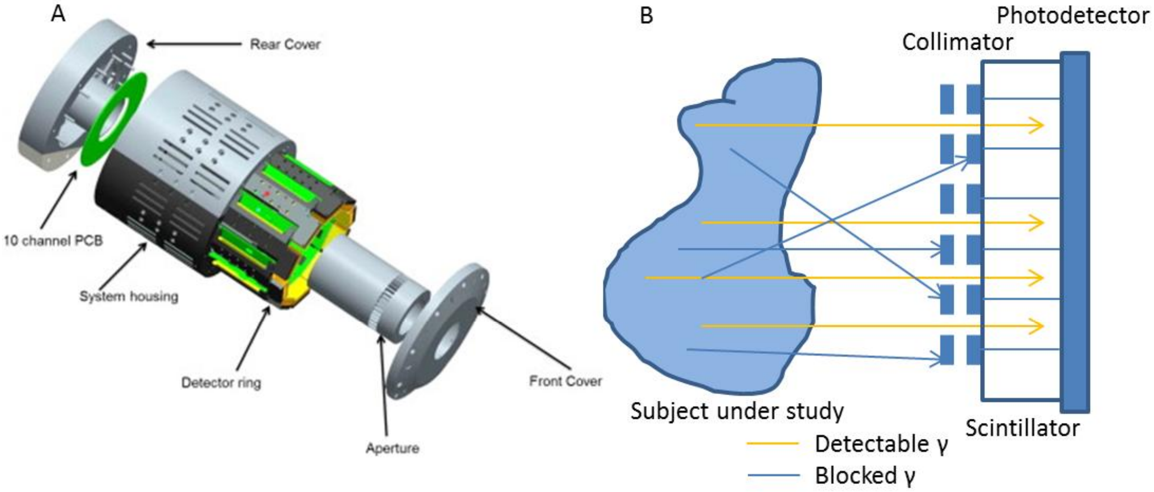

Figure 7.2 (A) Design of an MR compatible SPECT insert [7]; and (B) SPECT detection principle

C. Optical Wireless Communication

However, optical wireless communication (OWC) techniques are yet to be explored. This refers to visible/infrared light transmission of information in a free space medium. Vertical Cavity Surface Emitting Lasers (VCSEL) or light Emitting Diodes (LEDs) connected to the signal source provide fast, reliable and cost effective transmitters, while photodiodes (PDs) act as receivers of the optical signal, taking advantage either of direct, low beam divergence line of sight (LoS) or the diffuse reflection of the transmitted signal. With the widespread application of LED technology for indoors illumination (figure 7.3), OWC can be a non-ionizing alternative for low bandwidth internet of things applications [9].

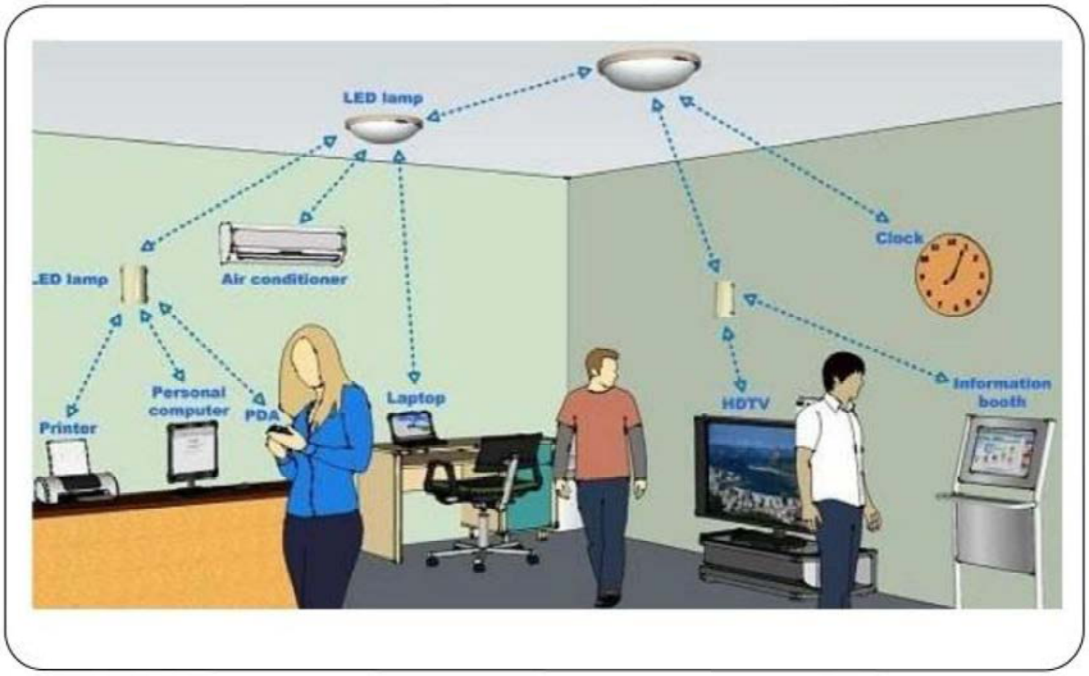

Figure 7.3 OWC application for indoors interconnection, using the illumination sources as wireless transmitters [10]

In the same context, OWC is also getting popular in medical instrumentation because it doesn’t add in electro-magnetic interference (EMI) as compared to RF technology. One such example is the transmission of ECG signal based on OWC link exploiting LED’s [11]. Moreover, low magnetic resistance of optical components [12] is compatible with applications in magnetic field and electrical decoupling due to non-electrical connection makes the device semi-transmissive to the magnetic gradients.

Thus, OWC system allows for a cost-effective solution, reducing the complexity, magnetic incompatibility and space occupation in comparison to a wired transmission system, while maintaining the original signal quality from the detector.

II. MATERIALS AND METHODS

D. Initial testing, study and simulation

While digital alternatives demonstrate very high data throughput, a first step was to evaluate whether standard OWC links could be enough for PET data. Different scenarios, with different sets of electronics inside the MR bore were simulated and data transmission approaches proposed. Nevertheless, if the intension has been to develop an absolutely minimal detector front-end, it would be crucial to establish a methodology to transmit directly the analog output of SiPM. In this manner digitalization inside the magnetic field is avoided, ensuring MR compatibility and greatly lowering the power necessary for the function of the front-end.

In order to evaluate the quality of data transmission for the particular application we simulated a LYSO scintillator pulse by the biexponential model $e^{-t/0.72} - e^{-t/43}$. The technical specifications of the VCSEL used are 680 nm wavelength, 16° FWHM full angle beam divergence, 2.2 mW output power and 5 GHz 3dB bandwidth. An avalanche photodiode (APD) with 2mm active area and 280 MHz 3dB bandwidth (with 50kHz lower cutoff frequency) was used as a receiver. A 4mm ball lens was placed in front of the VCSEL for transmission of collimated beam, while a 1″ bi-convex lens was used at the receiver for better light focusing. For the tested setting, where transmission takes place using VCSEL and ball lens, the LoS has to be direct. The transmitter and receiver where placed at an approximate 2m distance from each other. With this test, we established the efficiency, bandwidth and time jitter of the optical channel.

Jitter is considered the deviation from true periodicity of a presumed periodic signal in electronics and telecommunications, often in relation to a reference clock source. Jitter may be observed in characteristics such as the frequency of successive pulses, the signal amplitude, or phase of periodic signals. Jitter is a significant, and usually undesired, factor in the design of almost all communications links (e.g., USB, PCI-e, SATA, OC-48). In clock recovery applications it is called timing jitter. It can be quantified in the same terms as all time-varying signals, e.g., root mean square (RMS), or peak-to-peak displacement. Also like other time-varying factors, jitter can be expressed in terms of spectral density (frequency content).

For the use of coincidence and time-of-flight, techniques that are essential to PET, the timing of pulses must be very precisely evaluated. Optimally, a jitter of less than 100 ps is favorable. In order to measure the jitter of analog pulses for our application, one needs to measure the jitter of the output of an ideal comparator, between the input waveform and a threshold, in relation with a trigger reference. The threshold favored is optimally just above the noise level; in this experimental setting an approximate 10% of the peak was applied at the trigger threshold for a high bandwidth oscilloscope, (Teledyne Lecroy Wavemaster8 Zi-B, 30 GHz bandwidth, Courtaboeuf, Cedex, France)

E. Testing with SiPM

A next test involved connecting the output of a Hamamatsu S10985 MPPC SiPM to the same OWC topology and transmitting an amplified as well as a non-amplified analog pulse over a distance of 2 m (figure 7.4). Being able to record and analyze these pulses, it was possible to evaluate the noise component. Moreover, by this test we introduced the concept of analog OWC (aOWC), a novel approach not found in literature. This created difficulties, as communication concepts such as multiplexing have not been developed for aOWC.

Figure 7.4 Experimental setting of transmission of PET analog pulses over OWC.

F. Multiplexing techniques

Analog charge division multiplexing (CDM) approaches have been broadly discussed in previous chapters. However, the limitations of such schemes have also been demonstrated. However, it is required to develop a system that would apply as few as possible transmission channels. Further multiplexing the Anger outputs without compromising transmission of information quality can further lower the size, consumption, complexity and data throughput of the detector module. For this reason, a study was necessary, to evaluate already existing multiplexing schemes and possibly develop new ones.

Space division multiplexing (SDM) corresponds to independent transmitter per channel and is the most direct approach that could be adopted to realize a PET insert. This technique might only be suitable for small inserts with small number of detector modules. Other approaches, such as Frequency Division Multiplexing (FDM) [12], where each channel can be transmitted using difference carrier frequencies were also considered. Nevertheless, this approach would require higher bandwidth photodiode and therefore has not been evaluated at this stage.

For the initial prototype, we developed an analog Time Division Multiplexing (aTDM) circuit (figure 7.5 left) that delays three of the four outputs of the resistor network with different analog delays of 200ns steps, showcasing a simple circuit that can take advantage of the signal's non-continuous nature, only slightly deteriorating the dead time of the detector (figure 7.5 right). This approach might not be applicable in a final design, due to the long duration of LYSO pulses and the corresponding sizable and inductive analog delays. However, application of faster scintillators, such as LuAG:Pr [13], or different doping approaches [14], can lead to faster pulses, that can still be transmitted due to the ample bandwidth of the transmitter. In this case, smaller delay components could be applied and render this multiplexing solution compatible with the magnetic field.

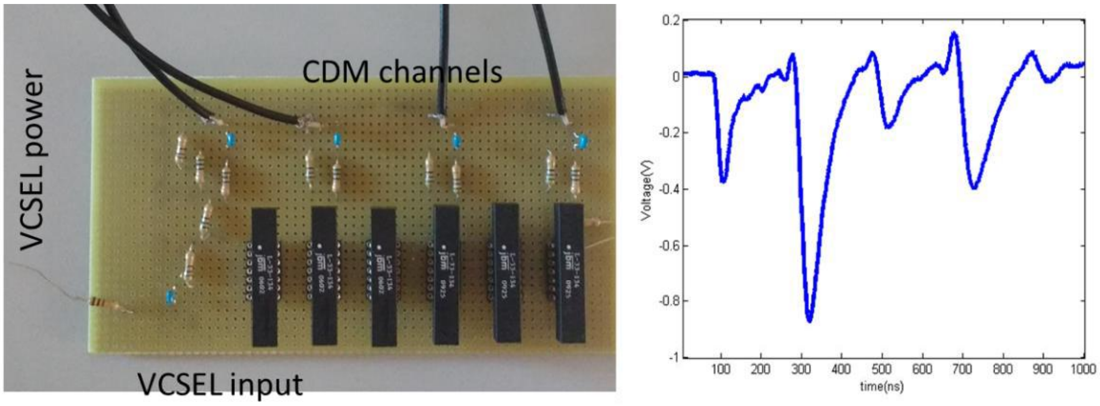

Figure 7.5 (Left) aTDM prototype circuit with pairs of 100 ns delays per channel; and (right) Demonstration of 200ns aTDM of scintillation pixels

In an alternative signal treatment that could have advantages for scaling up to full system scale, the detector pulses can be discriminated and transmitted in a time-over-threshold (ToT) scheme. This is a common approach in detector technology [15] and in this case, more flexibility on the multiplexing alternatives available is provided by the simpler nature of the ToT pulses. Multi-voltage threshold designs, such as the one developed and demonstrated in the previous chapter can easily be adapted for simultaneous transmission (figure 7.6).

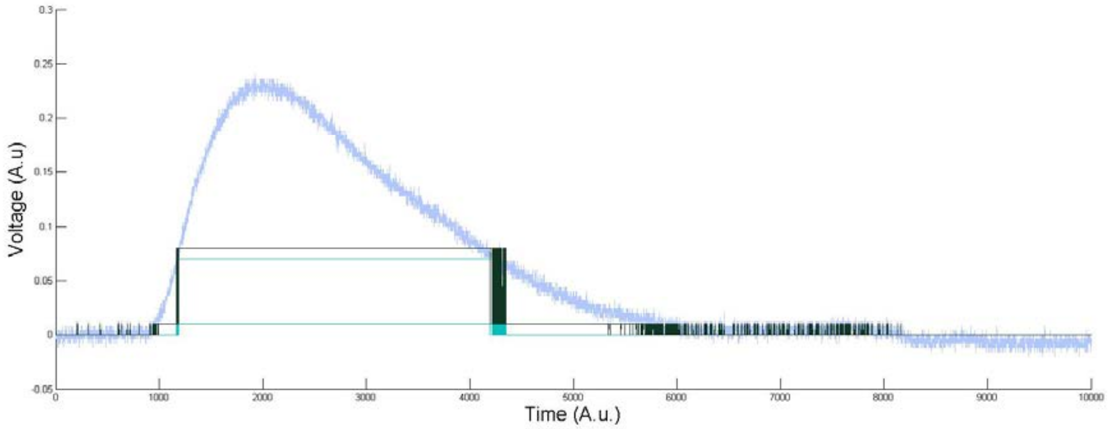

Figure 7.6 Demonstration of creating a single waveform (dark) from two ToT ones (light blue), in a MVT scenario.

G. *Testing with a lightweight PET insert prototype*

Finally, we connected the analog outputs of a prototype developed in our lab, housing four Hamamatsu MPPCs and a CDM network for the 64 channels [16]. The prototype SiPM CDM outputs were connected to an aTDM network (figure 7.7), allowing for the information on scintillation events of the whole detector to be transmitted by one single communication channel, demonstrating in practice a 64:1 multiplexing ratio. Unfortunately, it was not possible to use an external β+ radioactive source, thus the events from the intrinsic LYSO (lutetium) activity were used [17]. This activity is a result of the very slow β- decay of ^{176}Lu and has a very low count. However, it is useful for the characterization of a radiation detector as to a great extent it falls within the energy range of emission of most radiotracers for SPECT [18] while not being far from the 511 keV range for PET.

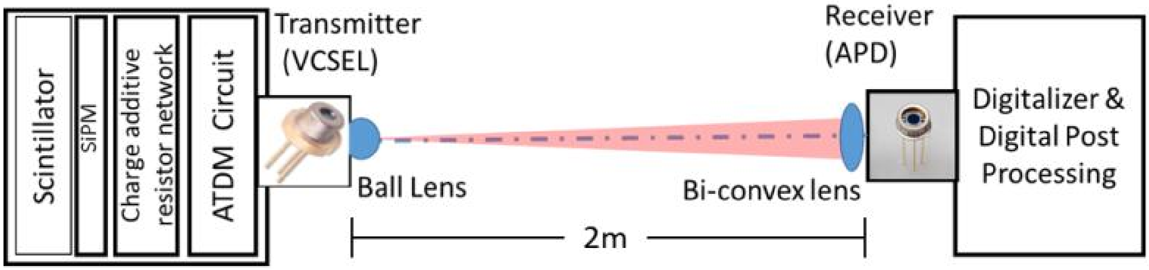

Figure 7.7 Schematic outline of the complete setting of the proof of concept experiment

III. RESULTS

A. *Digital OWC transmission scenarios*

Digital transmission scenarios that were initially evaluated provided interesting insight in the data yield of a PET insert. In the first scenario of OWC application, it was considered that a link could be established between an internal logic unit and an external one. With this approach the electronics-free effort is compromised by placing an initial processing unit (ASIC, FPGA) inside the chamber. Still the advantage of OWC in this architecture is that the RF environment will not affect the communication and the insert will not be electrically coupled to the MRI. From the description of the small animal PET insert specifications of the previous chapter, the data rate is calculated: 16 bytes per event x 250KHz = 32 Mbps per detector => 12.288 Gbps. This means that by 6 OWC channels the whole insert can be served. Alignment studies were performed for this scenario and are demonstrated in figure 7.8.

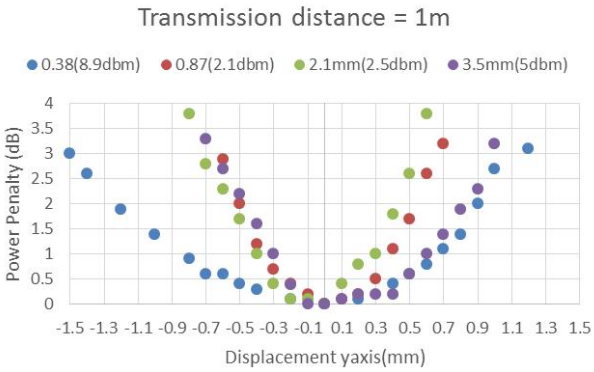

Figure 7.8 Displacement studies for 2.5 Gbps data rate per OWC channel

The misalignment tolerance range of the designed system is ±6mm with 3dB power deterioration. This relation possibly will not be relevant for the application of very fast GaN LEDs, which can take advantage of the diffuse reflections of the transmitted signal without compromising the bandwidth of communication. However, this scenario was not considered satisfactory, given that it compromises the most important goal of this study, to demonstrate viability of an insert without any digital logic inside the MR bore.

B. *Time critical results*

Timing characterization was established by transmission of the biexponential scintillation pulse model. Even through the bandwidth of OWC link is 280MHz, limited by the bandwidth of the receiver, it was possible to retrieve a very sharp rising edge at the receiver (figure 7.9). Baseline distortion observed was corrected by adding a baseline restoration circuit at the back-end. Consequently, it is foreseen that the CDM pulse, which demonstrates low-pass filtering, deteriorating the fast component more than an order of magnitude, as demonstrated in the previous chapter, is transmitted without deterioration.

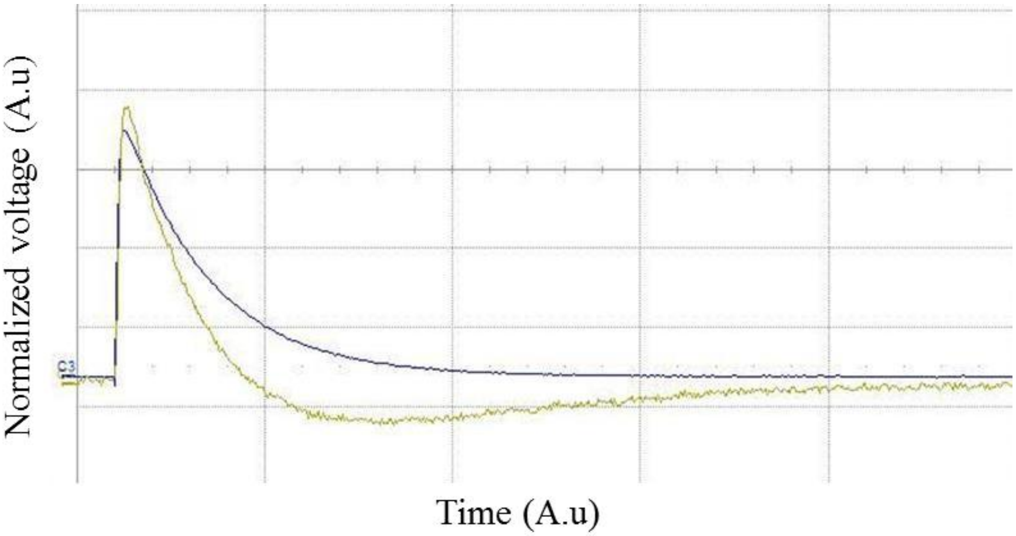

Figure 7.9 Normalized transmitted (black) and received (green) biexponential scintillation pulse model

The jitter of this communication technique has full width at half maximum (FWHM) of 80ps (figure 7.10), rendering this technique not only sufficient for coincidence detection but also compatible with time of flight (TOF) scenarios. This is sufficient for the analog output of SiPM, but for better precision and possibly enhanced timing that would affect greatly the energy resolution in ToT scenarios, higher bandwidth receivers can be applied [16], given that the bandwidth of the VCSEL transmitter is in the GHz range. Such approach would also permit the noise correction MVT approach developed in the previous chapter to be applicable in an OWC insert scenario.

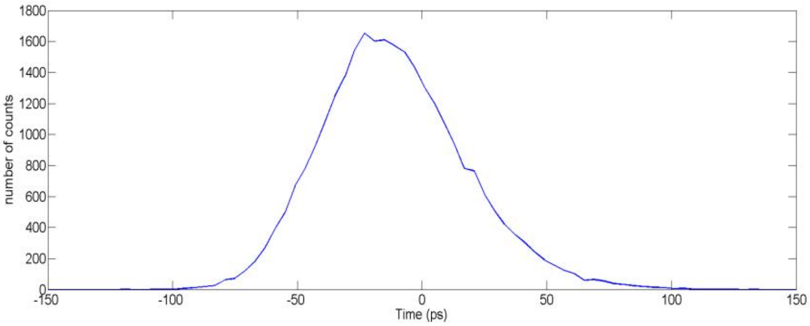

Figure 7.10 Timing jitter measurement for biexponential scintillation model transmission

C. Power consumption

Another element that is important for this application concerns the power consumption of the insert. Figure 7.11.A and 7.11.B presents the normalized amplified and non-amplified signal comparison respectively between the transmitted and received pulses. The main aspect of interest is the similarity of input and output waveforms. We demonstrate that a non-amplified output can also be directly transmitted without significant deterioration of the pulse peak to noise ratio. The total consumption of a single front-end detector module, in this case, is only few milliwatt, largely depending on the consumption of the VCSEL transmitter. This is a very good result that could allow, even at system level, passive cooldown through the shielding, without temperature variations or heating danger for the subject under study or the.

For the same reason, powering such modules can be easier than anticipated and a small MR compatible battery, like the ones used in implantable devices [19] can be applied. Another approach that would require more analysis and experiments can be remote powering the device through uplink optical wireless topologies [20]. This approach could also provide nominal control options.

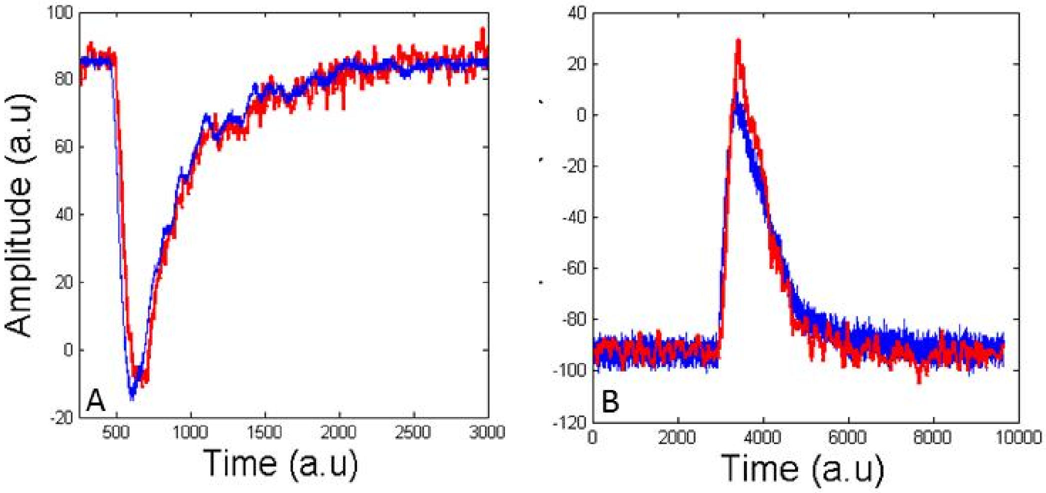

Figure 7.11 (A) Amplified inverted normalized input and output of the OWC setting; and (B) Non-amplified normalized input and output. In both cases blue is transmitted, red is received.

D. Energy resolution and signal quality results

Signal quality is usually expressed in bit-error-rate (BER), corresponding to the number of bits of transmitted information that are not correctly received. BER of values of more than 10^{-11} is satisfactory for most applications. However, as this metric corresponds to digital transmission, it is not applicable in this case. A new quality metric was needed. Since there are two important factors to be retrieved, timing and energy of pulse, to be used for position reconstruction, the focus fell on those. Timing considerations have already been addressed, thus the quality of this transmission is quantified by the signal error average given by equation 7.1, where E_t and E_r are integrals of transmitted and received pulses. These integrals correspond to the energy of individual scintillation pulses used for the reconstruction of energy and position of an event in Anger logic readout. The energies are normalized by a coefficient resulting from the ratio of the average energy of transmitted and received pulses.

$$Error = \langle \frac{\sqrt{{E_t}^2-(C_{norm}\times E_r)^2}}{E_t} \rangle, C_{norm} = \frac{\langle E_t \rangle}{\langle E_r \rangle} \qquad \text{Equation 7.1}$$

By this equation we calculate the average error at approximately 0.01. The integral was used for transmission quality, as it is the quantity used for the reconstruction of energy and position of an event. Position error, by calculating the error propagation function for Anger logic schemes (equation 6.1), was found to be around 7x10^{-3}, comparable to the least significant bit (LSB) of spatial resolution after digitalization of the SiPM prototype channels.

Using the activity from the intrinsic radiation of the LYSO crystal, we evaluated the energy performance, noting the main energy range of the spectrum (figure 7.12). The main characteristics of lutetium spectrum at 202 and 308 keV are visible and delinate the quality of transmission within this energy range. Though there is no definite quality measure for PET, due to the lack of β+ source, it is demonstrated that there is minimum aberation due to OWC on the spectrum at the energy range that is used for SPECT, for which compton scattering is the prevalent scatter process. A big number of very low energy events is retained because due to low count those events were also used for characterisation of the design.

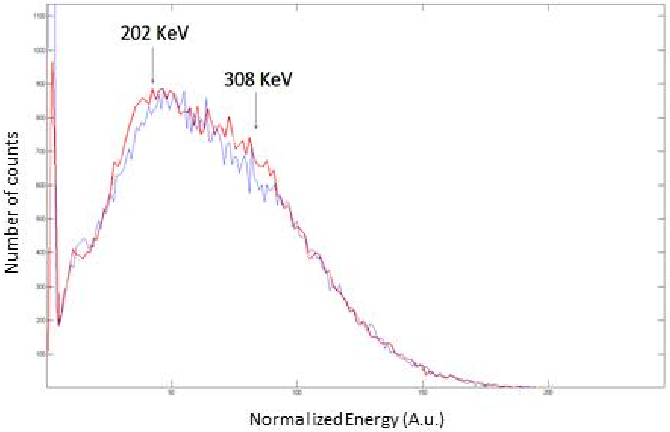

Figure 7.12 Energy spectrum of the intrinsic lutetium activity before (red) and after (blue) analog OWC transmission.

E. Field flood diagram

In order to demonstrate the proof of concept of OWC scintillation detector and the viability of an analog multiplexing scheme such as aTDM, we reconstructed the events of the intrinsic lutetium activity of an 8x11array of 1.6 mm^2 pixels a field-flood diagram (figure 7.13). This initial result has important factors compromising its quality, such as low count, channel crosstalk and difficult thresholding due to low energy. However, it is an important milestone result, demonstrating analog TDM 4:1 of the Anger logic channels, which have already been charge-addition multiplexed in factors such as 36:4 or 64:4. Finally, analog OWC suitability for the transmission of scintillation pulses is proven.

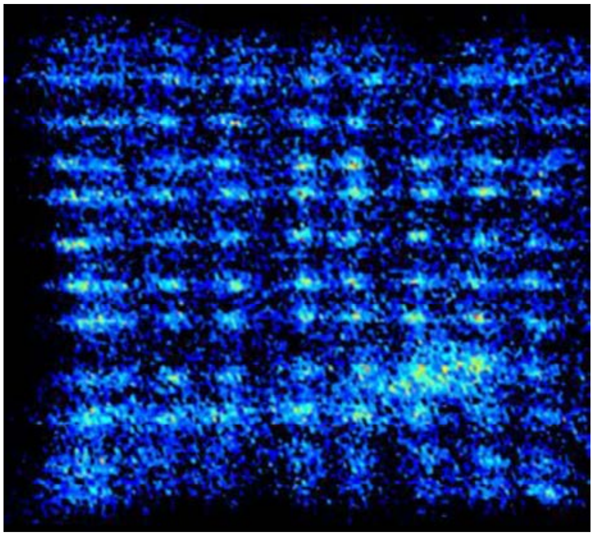

Figure 7.13 Field flood diagram reconstruction from intrinsic LYSO radiation through aTDM and OWC

IV. DISCUSSION-CONCLUSIONS

With this initial, proof of concept experiment, we demonstrate the viability of the application of OWC for the development of optical wireless nuclear medicine detector modules. High fraction multiplexing techniques have been discussed and tested and successful reconstruction of energy and spatial characteristics of the scintillation events has been exhibited. Solutions for powering and scaling up have been proposed and will be attempted.

We are currently developing a prototype of the front end with only passive components, except for the photodetector and VCSEL. Passive approaches on alternative charge multiplexing schemes with higher multiplexing ratio [22] are also being evaluated. ToT solutions and multiplexing, possibly with the application of low consumption high bandwidth ASICs [1] and an MVT ToT approach, will be tried.

Event reconstruction has only been addressed in a generic manner and should be adapted to the chosen multiplexing scheme, something that is enabled by the independent nature of the architecture of the backend. Design specific intelligent FPGA front-ends pose as the most viable solution, facilitating scaling up to a full system.

Nevertheless, the current prototype of the intended design demonstrates the flexibility and potential of the development of a modular PET or SPECT insert with minimal electronics. The analog output of SiPM is transmitted with OWC sets, rendering this solution superior to any wired proposals in terms of space occupied inside the gantry. Here, direct contact or cabling between the front-end and back-end is not required, while signal quality is preserved. This approach facilitates the integration of modular detectors with MR coils and is a solution which will allow case-specific PET or SPECT topologies. Those future designs will be adaptable to the size of the MRI bore (figure 7.14) and the characteristics of desired acquisition, with applications in neuroscience, cardiology, oncology or other field, in clinical or experimental scenarios.

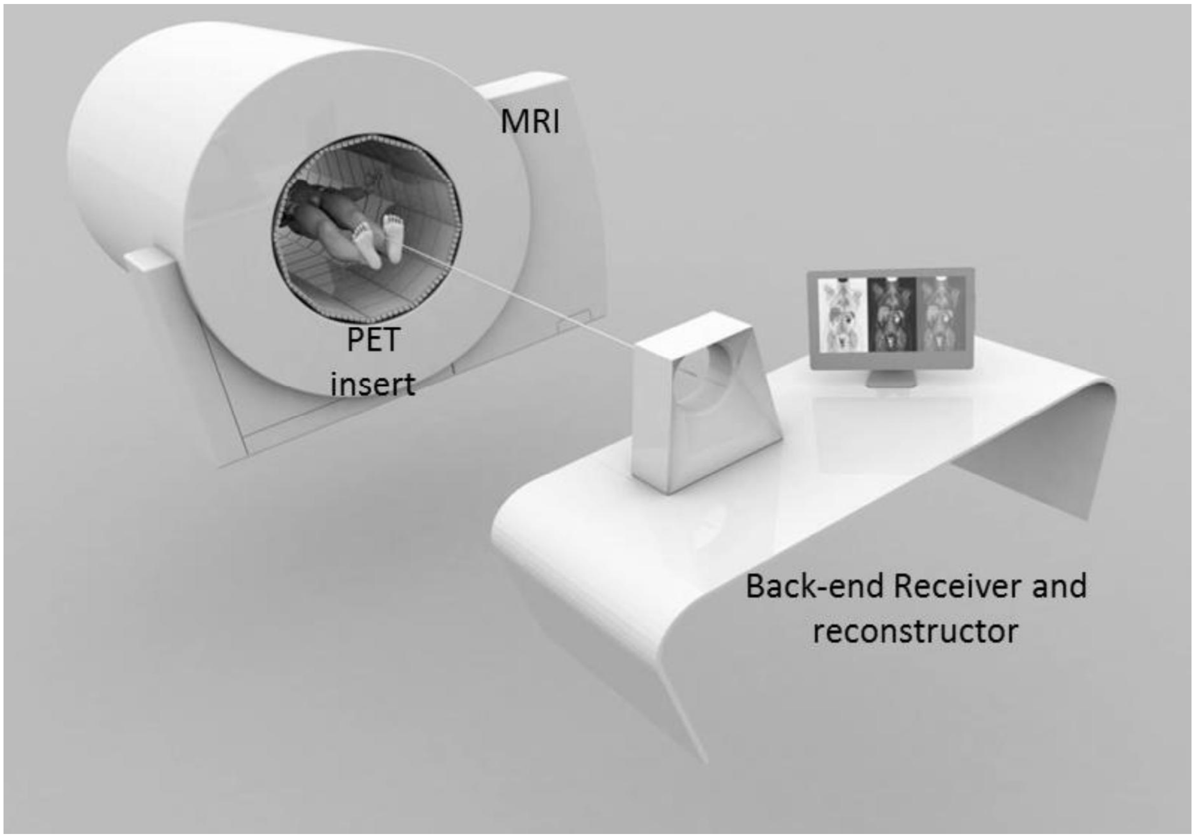

Figure 7. 14 Conceptual design of a whole-body MR compatible OWC PET insert.

V. REFERENCES

[1] Anghinolfi, F., Jarron, P., Martemiyanov, A. N., Usenko, E., Wenninger, H., Williams, M. C. S., & Zichichi, A. (2004). NINO: an ultra-fast and low-power front-end amplifier/discriminator ASIC designed for the multigap resistive plate chamber. Nuclear Instruments and Methods in Physics Research Section A: Accelerators, Spectrometers, Detectors and Associated Equipment, 533(1), 183-187

[2] Vagner, I. D., Lembrikov, B. I., & Wyder, P. R. (2013). Electrodynamics of magnetoactive media (Vol. 135). Springer Science & Business Media

[3] Breton, E., Choquet, P., Goetz, C., Kintz, J., Erbs, P., Rooke, R., & Constantinesco, A. (2007). Dual SPECT/MR imaging in small animal. Nuclear Instruments and Methods in Physics Research Section A: Accelerators, Spectrometers, Detectors and Associated Equipment, 571(1), 446-448.

[4] Kuhl, D. E., & Edwards, R. Q. (1963). Image Separation Radioisotope Scanning 1. *Radiology*, *80*(4), 653-662.

[5] Del Guerra, A., Belcari, N., & Bisogni, M. (2016). Positron Emission Tomography: Its 65 years. RIVISTA DEL NUOVO CIMENTO, 39(4), 155-223.

[6] Heller, S., & Zanzonico, P. (2011, May). Nuclear probes and intraoperative gamma cameras. In *Seminars in nuclear medicine* (Vol. 41, No. 3, pp. 166-181). WB Saunders.

[7] Cai, L., Lai, X., Shen, Z., Chen, C. T., & Meng, L. J. (2014). MRC-SPECT: A sub-500μm resolution MR-compatible SPECT system for simultaneous dual-modality study of small animals. Nuclear Instruments and Methods in Physics Research Section A: Accelerators, Spectrometers, Detectors and Associated Equipment, 734, 147-151.

[8] Olcott, P., Kim, E., Hong, K., Lee, B. J., Grant, A. M., Chang, C. M., ... & Levin, C. S. (2015). Prototype positron emission tomography insert with electro-optical signal transmission for simultaneous operation with MRI. *Physics in medicine and biology*, *60*(9), 3459.

[9] Elgala, H., Mesleh, R., & Haas, H. (2011). Indoor optical wireless communication: potential and state-of-the-art. *IEEE Communications Magazine*, *49*(9).

[10] http://www.w-o-li-fi.tk/2015/06/optical-wireless-communication.html, retrieved 22.02.2017

[11] Dhatchayeny, D. R., Sewaiwar, A., Tiwari, S. V., & Chung, Y. H. (2015). Experimental Biomedical EEG Signal Transmission using VLC. *IEEE Sensors Journal*, *15*(10), 5386-5387.

[12] Ali, W., Corsini, R., Ciaramella, E., Dell'Orso, R., Messineo, A., & Palla, F. (2015). High speed optical wireless data transmission system for particle sensors in high energy physics. *Journal of Instrumentation*, *10*(08), C08003.

[13] Nikl, M., Ogino, H., Krasnikov, A., Beitlerova, A., Yoshikawa, A. and Fukuda, T. (2005), Photo- and radioluminescence of Pr-doped Lu3Al5O12 single crystal. phys. stat. sol. (a), 202: R4–R6. doi:10.1002/pssa.200409079

[14] Spurrier, M. A., Szupryczynski, P., Yang, K., Carey, A. A., & Melcher, C. L. (2008). Effects Ca^{2+} Co-Doping on the Scintillation Properties of LSO:Ce. *IEEE Transactions on Nuclear Science*, *55*(3), 1178-1182.

[15] Shimazoe, K., Wang, Y., Takahashi, H., Kamada, K., Yoshino, M., Kataoka, J., ... & Kumagai, K. (2011, October). Time over Threshold based digital animal PET (TODPET). In *Nuclear Science Symposium and Medical Imaging Conference (NSS/MIC), 2011 IEEE* (pp. 3267-3271). IEEE.

[16] Chil, R., Konstantinou, G., Desco, M., & Vaquero, J.J., (2016) Compact, MR Compatible SiPM Small Animal PET DOI Detector, IEEE NSS/MIC proceedings

[17] Wei, Q. (2015). Intrinsic Radiation in Lutetium Based PET Detector: Advantages and Disadvantages. arXiv preprint arXiv:1501.05372.

[18] Ritt, P., Vija, H., Hornegger, J., & Kuwert, T. (2011). Absolute quantification in SPECT. European journal of nuclear medicine and molecular imaging, 38(1), 69-77.

[19] Wollmann, C. G., Steiner, E., Vock, P., Ndikung, B., & Mayr, H. (2012). Monocenter feasibility study of the MRI compatibility of the Evia pacemaker in combination with Safio S pacemaker lead. *Journal of Cardiovascular Magnetic Resonance*, *14*(1), 1.

[20] Wang, N., Zhu, Y., Wei, W., Chen, J., Liu, S., Li, P., & Wen, Y. (2012). One-to-multipoint laser remote power supply system for wireless sensor networks. IEEE Sensors Journal, 12(2), 389-396.

[21] Proakis J., Saleh M. (2007) Digital Communications, McGraw-Hill Education

[22] Thompson, C. J., & Goertzen, A. L. (2011). Evaluation of a 16: 3 signal multiplexor to acquire signals from a SPM array with dual and single layer LYSO crystal blocks. *IEEE Transactions on Nuclear Science*, *58*(5), 2175-2180.

Chapter 8: A time-over-threshold based front-end FPGA architecture for the readout of OWC PET/SPECT

I. INTRODUCTION

A. General

Along the previous chapters, novel solutions in the direction of constructing a light-weight, cost-effective, miniaturized and detached MR compatible PET insert have been proposed. On one hand, with SSLE, the packing fraction and sensitivity of the detector is much higher due to the lack of non-scintillating reflectors. This leads to the possibility of using shorter crystals and choosing the desired form without any limitation of shape, while furthermore depth of interaction designs have been successfully tried. On the other hand, simulations and preliminary results have shown that pixel maps have particular “zones” where an event can’t be clearly attributed to a particular pixel (p), especially for multi-layer DoI crystal assemblies, where also the DoI layer (l) has to be identified, and for Anger logic read out schemes. To optimize the read out, we characterize an “elemental detector” as a node (p, l). Each position of the x, y transverse plane where a scintillation event might be detected can correspond to more than one nodes, acquiring probabilities to belong to any (p, l) nodes, as an expansion of the approach in [1], [2].

On the OWC study, results from a proof of concept prototype demonstrate that it is possible to read out the charge division multiplexed (CDM) analog pulses of a position sensitive SiPM by directly connecting them to a VCSEL transmitter, without transimpendance or any other amplification means. With this method, together with other optical multiplexing techniques, we loosened the power consumption and spatial constraints on the PET front-end, thus providing a promising detached front-end solution. However, the prototype is limited on the number of available channels and the early digitalization requires more power resources and further improvements on the digital system architecture for operating in a high magnetic field. Research on alternative multiplexing schemes is ongoing. However, the application of time-over-threshold (ToT) designs, using the algorithm developed for reconstruction and application-specific integrated circuits (ASICs) [3] on the front end seems that could facilitate it greatly. It is noteworthy that developing an OWC system provides very important insight on electronic design for a fiber optic front end, the merits of which have already been demonstrated [4]. Furthermore, the ToT and multiplexing combination can lead to a highly integrated and extremely low consumption front-end prototype, which can be adapted in different architectures and demonstrate supreme magnetic field compatibility as compared to existing designs [5].

B. Pre-processing

All these solutions, however, face a slight limitation: High intelligence, that has been developed and proven in offline analyses, should be possible to function at very high rate, pipelining incoming information. Such requirement could be possible for singular detectors, but would be a realistic goal only if scaling-up considerations can be included. Fortunately, drawing from experience in the field of detector instrumentation technologies, such solutions exist and find usage in all relative applications; they correspond either to ASICs, that take care of both analog and analog to digital conversion signal treatment and functions (for instance [6, 7]); digital data can then be processed by microprocessors that also perform the connection to a computing system. For pipelined designs with timing specifications like described application, these microprocessors are widely chips, called field-programmable-gate arrays (FPGAs-figure 8.1) [8], generic configurable integrated circuits.

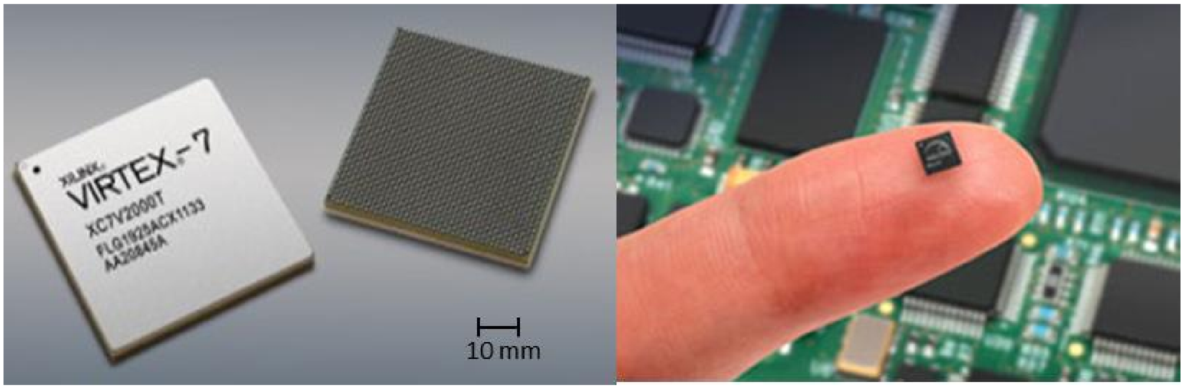

Figure 8.1 Two extremes of the FPGA device family, demonstrating different physical and structural characteristics [9,10]

The FPGA technology was invented in 1985 and provided a novel silicon space where the user could easily program the interconnection architecture between pre-existing gates. In modern tiles these pre-existing cells comprise of sets of inverters, logic gates and look-up tables, while higher functions such as phase-locked loops for clocking and big blocks of memories are often found.

Providing direct access to the hardware architecture is very beneficial, mainly by allowing direct access to information flow and consequent case-specific logic that can be implemented. The way to administer this logic is by specific hardware description languages, most common of which are VHDL [11] and Verilog [12]. These languages in principle provide the utilities necessary for programming designs directly on hardware in a scheme termed firmware [13]. Current development trends intend to bridge the gap between software and firmware, either by utilities that allow higher level programming tools to be directly applied on FPGAs, such as System-C [14], or by including programmable gate arrays within next generation computer processing units [15] and vice versa [16] (figure 8.2).

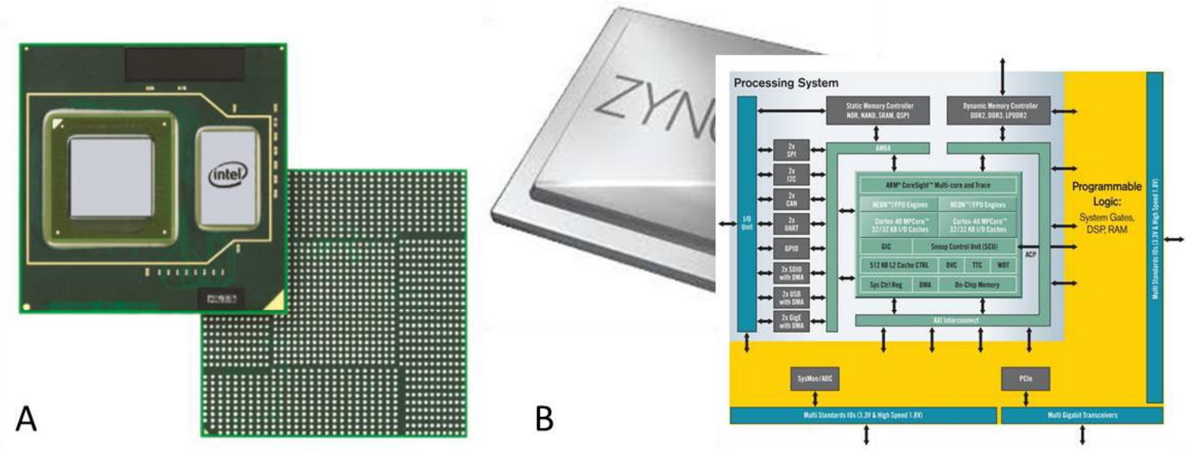

Figure 8.2 (A) FPGA integrated in CPU [15]; and (B) FPGA integrating microprocessors [16].

FPGA clocking can reach hundreds of MHz and each clock cycle corresponds to massively parallelized logic functions. As can be derived, verification of functionality in material is a lot more laborious, requiring furthermore high-end laboratory equipment, such as very fast oscilloscopes, and access to the datastream that is often impossible; this is why the workflow with FPGAs is based on simulation of the intended architecture (figure 8.3). Simulations include the development of a simulating test-bench, where realistic inputs are provided and the range of output results, along with timing, power consumption and material utilization information become available. This process leads the development of firmware in a recursive loop, until specifications are met and complete debugging has been performed. Once the FPGA has been loaded, it can be equally easily reloaded with different firmware, as long as important limitations, such as interconnection to hardware, are respected.

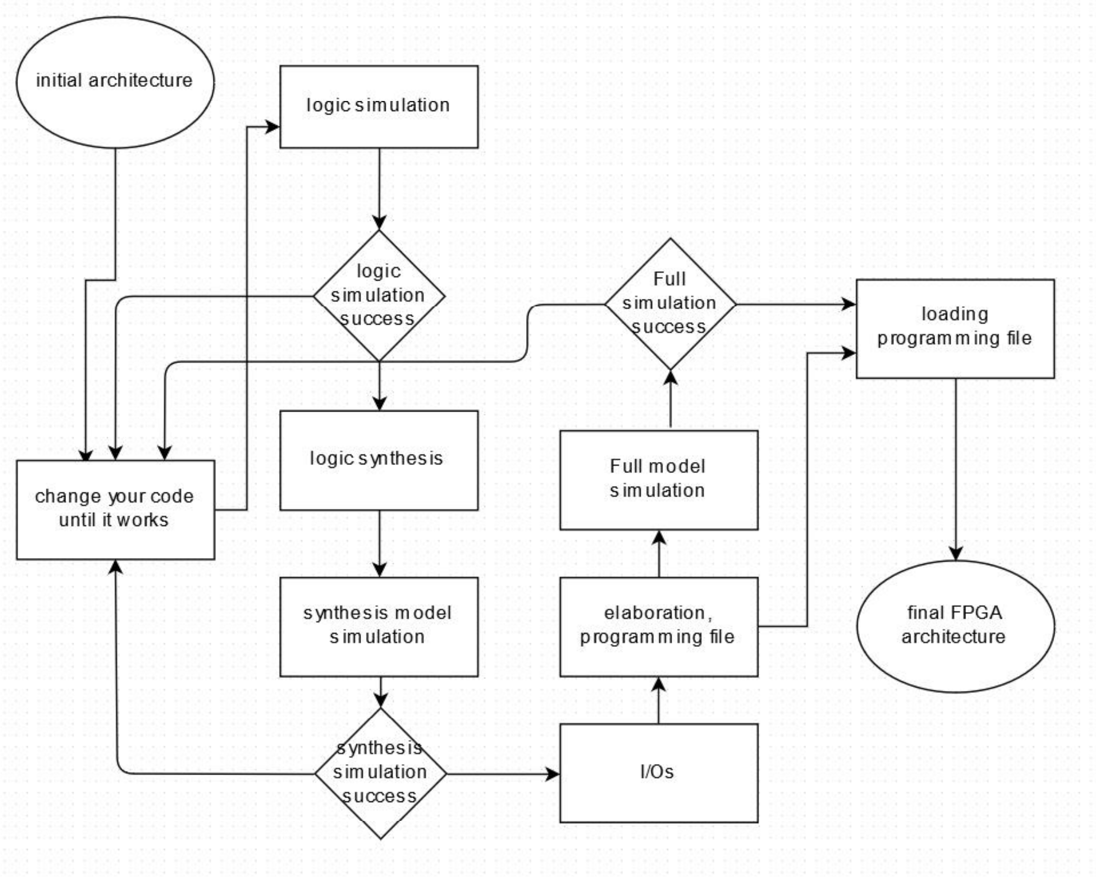

Figure 8. 3 FPGA simulation based workflow

In order to take full advantage of the abilities of an FPGA, vendor specific training and feature understanding is necessary; however, the general outline is usually the same. Advanced input treatment provides nominal analog to digital (ADC) [17] and extended time to digital [18] (TDC) conversion attributes; addition of higher functionalities is possible even when no dedicated material has been foreseen [19]; FPGAs can thus provide the raw material for the development of case specific Systems-on-Chip (SoC), greatly accelerating, facilitating and slashing the cost for detector applications, like the intended design of MR compatible PET inserts, and making the use of converters or ASICs redundant.

C. Design features

Developing a firmware concept architecture can be an interesting, as well as achievable, research goal to demonstrate system integration characteristics for the back-end part of the prototype. In this manner we can create a data acquisition backbone that would support the electronic design and, most importantly, demonstrate whether the whole idea is possible, or if a totally different approach (e.g., developing a specific ASIC for back-end reception) should be pursued.

The initial step is to perceive and outline the architecture intended. For the described novelties to be implemented, it would be necessary to include several features: there should be an input stage which, as will correspond to ToT pulse conditioning, must definitely include TDCs. This means developing a firmware design, that takes advantage of FPGA hardware elements and is able to count the duration of pulses with fine-time resolution of few picoseconds, compatible to the study performed in previous chapters and the hardware limitations of both the FPGA and available fast discriminators.

Furthermore, implementing intelligence in pre-processing corresponds to feature characterization and pipelined extraction of the values necessary from the incoming pulses. As has been discussed, noise corrected multi-voltage threshold (NCMVT) ToT leads to accurate calculation of time of arrival (ToA), energy and position of independent events. Demonstrated non-linearity of the NCMVT ToT scheme can be directly compensated by the application of hardware logic, such as extensive look-up tables (LuT). In the same manner, position calculation, even for the fuzzy logic approaches discussed previously, can be achieved.

In order to retrieve the information necessary for fine-tuning such algorithms, such as noise characteristics for threshold setting, pulse sets for energy histograms and field-flood diagrams (FFD) and even raw pulses for debugging, it would be equally necessary to provide the possibility to have different run options, which would provide different sets of information. Finally, the architecture should perform data treatment and transmission to a back-end, with lower timing specifications, where all data are gathered for coincidence detection, line-of-response attribution and finally image reconstruction. This back-end can be a powerful computer, or other FPGAs that could perform data routing, compression and acceleration for bigger machines. All of the above correspond to a feasible firmware design.

II. MATERIALS AND METHODS

A. *Input ToT signal and TDC*

To have realistic inputs for the initial development and evaluation of the firmware architecture, a set of prerecorded pulses from an Hamamatsu R8520-00-C12 PS-PMT based detector element, applying charge division multiplexing (CDM), digitized at 1 GHz, were discriminated and the ToT equivalent (figure 8.4) was provided at the input of the architecture. While the firmware design is intended for use with SiPM based detectors, the scintillation signal is in principle the same. Afterpulsing with this lower sampling rate and amplified analog pulse is significantly less that the scenario investigated in previous chapters. However, these pulses are sufficient for test benching and verification of an input TDC architecture (figure 8.4).

This approach refers to real world possible scenarios. In one, a front-end ASIC would discriminate and thus create the ToT pulse, the signal would then be transmitted optically, limiting its switching time according to the optical link and receiver, wireless or fiber, characteristics, before being input on the FPGA, where it would finally be converted to digital according to the TDC resolution. Another scenario refers to analog pulse being transmitted in its raw form and ToT discrimination to be made directly at the back-end, even using the very fast FPGA differential input discriminators [20]. Both these scenarios can be adapted to NCMVT ToT. The energy calculation logic changes, however the front end is the same and corresponds to a TDC setup.

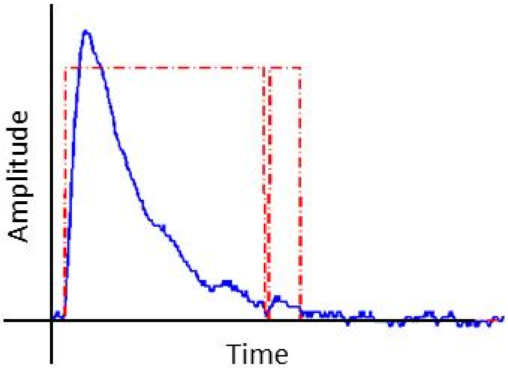

Figure 8. 4 Example of pulse from the repository (blue) and the corresponding ToT pulse (red). A secondary region can be observed after the principal region over threshold

There are various types of TDC, that correspond to different hardware algorithms for the measurement of duration [18]. TDCs have been used in the past for similar applications and there are plenty of examples in literature [20, 21]. Among the various possibilities, a tapped delay chain TDC (figure 8.5) was considered the most straightforward approach. In this design, the delay of a particular FPGA primitive gives an estimation of the minimum TDC resolution. For this to be achieved, careful placement and routing of the design primitives must be made, a process that is not only vendor-dependent, but also changes for different FPGA models.

For initial firmware development, a black-box delay element was applied, as a generic theoretical delay of 100 ps. This is a value that corresponds to the ones found in literature, while being close to the fast discrimination rise time. However, it is possible not only to confirm it, but to fine tune and lower it, in relation to particular models.

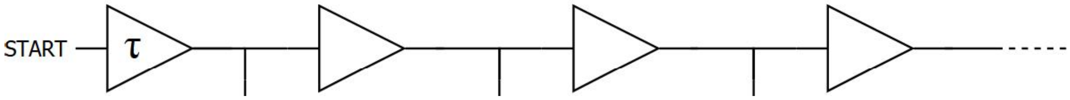

Figure 8. 5 Example of tapped delay line TDC. A serial vector is retrieved at the outputs of the delay elements and fine timing is retrieved through look up tables for rising and falling events

For testing of the tapped delay line TDC principle, a Spartan 3 FPGA from Xilinx, used for the development of PiPET [22] was used. It's architecture was slightly modified to directly address the tapped delay line proposal. The documentation on the model and primitives was inspected. There, a number of alternatives was found, that could serve as candidates. The preferred one will be chosen by having delay in the order of magnitude desired, being available in big numbers in the FPGA for scaling up possibility and to not block the utilization of other primitives, because in this case a big part of the FPGA would be occupied for no reason.

A similar study has been performed on the same FPGA where an optimal 45 ps was achieved [23]. In this study non inverting buffers and D flip flops where used, along with a number of tricks to shorten the length of delay line for more linear result. Linearity of such a system is greatly influenced by the number of delay elements. It is possible to replicate this measurement by building a similar code. The initial step, however, corresponds to assessing the linearity of delay, as a quality measure of the whole TDC. In this context, a high clock frequency design is favorable. For instance, for delay around 100 ps, a 312.5 MHz frequency (3.2 ns period) clock allows the TDC delay chain to be constructed with only 32 delay elements. The structure of the FPGA, which is organized in «slices» of two function generators (F and G), two storage elements, arithmetic logic gates, large multiplexers, wide function capability, and two fast carry look-ahead chains is found in literature [24] (figure 8.6). Timing information, however, need to be confirmed.

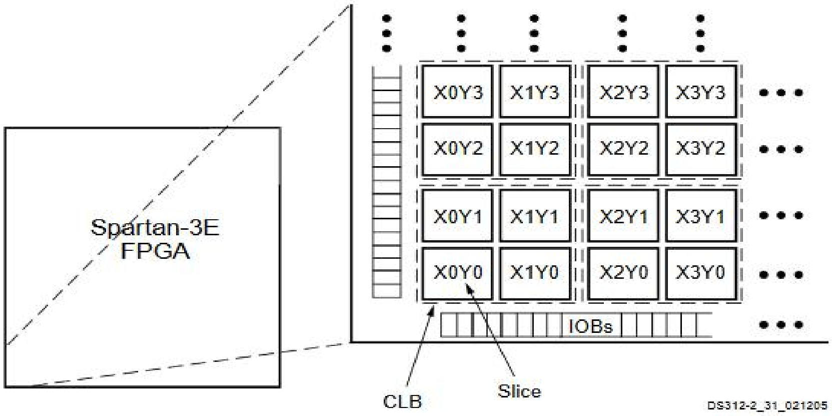

Figure 8. 6 Overview of the internal architecture of a common FPGA. This was exploited in the process of constructing a tapped delay line TDC

B. Position and energy

Individual channel energy calculation corresponds to the evaluation of pulse duration surrogate. This is an easy task initially, however addition of more complicated algorithms such as the NCMVT ToT approach might require more advanced logic to be implemented. A common approach in these cases is the application of big look up tables (LuTs). In that case, a particular input value directly points at a digital address where the corresponding output value is. LuTs occupy extensive space in FPGAs, depending on the size of input and output vectors and this is the reason why combinatory logic is in general preferred, except from particular cases.

An alternative, more elegant method can be directly correcting the input value by applying the equation constructed through fitting a set of experimental data. This can be done by either constructing an automatic correction routine in the FPGA, or by a set-up run, in which raw data from an acquisition, for instance with a ^{22}Na source is received and matched offline with the known energy distribution. A number of polynomial factors can then be uploaded back in the firmware.

Once the individual channel energy has been reconstructed and corrected for alinearities, it is possible to calculate the total energy and position of an event. Energy calculation in CDM logic corresponds to the addition of the energy of the four independent channels. In ToT this is served by a ToT duration surrogate. The same principle applies for any MVT approach, where the corresponding durations are multiplied with the threshold value, to provide a realistic number, like demonstrated in previous chapters. Furthermore, energy regions of interest can be set by the user. Bidimentional impact position estimation follows the standard CDM encoding demonstrated in equation 8.1, where X_1, X_2, Y_1, Y_2 are respectively the 1 to 4 input channels.

$$X = \frac{X_1 - X_2}{X_1 + X_2},\ Y = \frac{Y_1 - Y_2}{Y_1 + Y_2} \qquad \text{equation 8.1}$$

Straight-forward calculation of this measure is not possible, because division on FPGA is a complicated function whose implementation is typically vendor and device specific. Furthermore, embedded dividers require delays of several clock cycles and occupy wide areas on silicon. Higher level architectures are provided from the vendors (for instance megafunctions for XILINX, ip cores for ALTERA). Among these, it is possible to find implementable division alternatives. However, those are model specific, add significant delays and are not optimised for small FPGAs like the ones foreseen [24]. Furthermore, FPGA division often uses LuTs. For these reasons, it is not possible to avoid using a precalculated LuT on truncated inputs. As long as it can be possible to limit the range of inputs, knowing that there are particular characteristics in the inputs, developing a non-vendor-specific design can be a viable alternative.

In detector development, experimental runs demonstrate the quality of the detector and established pixel resolvability and corresponding spatial resolution [25]. Then, it is common place that a map is constructed, based on the FFD, with the areas that correspond to individual pixels (figure 8.7). It would accelerate the acquisition process if such a map could be loaded in the FPGA and events get assigned to pixels directly when their X and Y position coeficients are calculated.

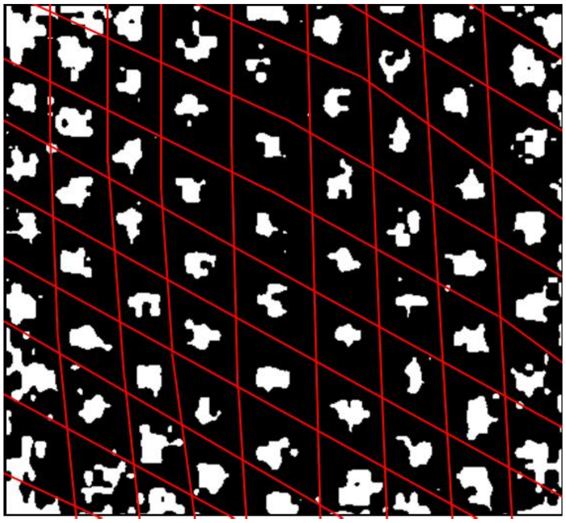

Figure 8. 7 Pixel geometry map resulting from color-saturated FFD, for automatic assignment of events to pixels

C. Run modes and general architecture characteristics

For any complete firmware architecture, apart from the core logic and input parts, connecting logic, data management and transmission, along with back-to-front control communication infrastructure must be implemented. Furthermore, given the specific characteristics of this design, it is important to implement a series of configuration and set-up run modes that would allow important information on the acquisition environment to be retrieved.

Initially, it would be important to be able to evaluate the behavior of noise, for threshold setting. This means that not only there can be an automatic process that evaluates the switching activity for different thresholds and chooses one that is within noise and that could most clearly provide ToT and ToA information, but also that constant noise monitoring should be in place. This information is also necessary in the case of NCMVT ToT.

As mentioned before, it is also important to be able to retrieve raw pulses in order to establish ToT alinearity, correct it and evaluate the energy content of individual channels, as well as that of the whole pulse. Optimally, it should be possible to retrieve raw, unprocessed [X_1, X_2, Y_1, Y_2] sets instead of [t, X,Y,E] tuples. Even more, it could be possible to retrieve raw TDC measurements for configuration and synchronization reasons.

With such acquisitions it should be possible to gain significant insight on detector characteristics and offline software callibration routines can be developed. On the other hand, availability of runtime alarms is a very useful feature with broad applications. In this context signals associated with too much noise, according to preset user limits, pile up events, delineated through user defined duration thresholds, and regions of baseline or ground disruption can be implemented [26]. This information, along with statistics on event rate and energy can be gathered and sent periodically to the back-end.

Communication can either be taken care of by direct serial connections, or, for more flexibility and portability, a UDP node can be constructed on FPGA either by directly coding in HDL or by setting up a nominal microprocessor unit, such as the microblaze [27].

III. RESULTS

A. ToT and timing results

On the hardware design part, the intention is to apply a very low voltage threshold, to capture the rising edge for timing and the length of the pulse for energy evaluation with the lowest jitter as possible. This could create a complication, as increased switching activities due to noise captures at the TDC input could compromise the timing measurement. Yet, noise counts can be used for automatic set-up of ToT threshold [25]. Nevertheless for initial experimentation an arbitary threshold was set for the ToT construction. In a similar manner, empirical duration thresholds were applied, on the one hand to make sure that no noise is recorded as events, and on the other to provide pile-up detection. Thus, pulses shorter than 51.2 ns and longer than 409.6 ns are automatically rejected. In figure 8.8 the whole input process functionality can be observed, from the analog pulse converted to ToT offline and used as a test-bench level input to the waveform results. The measured duration offline and on firmware match. ToT and ToA information, necessary for timing measurement, propagate towards the back end of the architecture.

Using this initial building block, it is possible to create combinatory designs and thresholds for better discrimination against noise and optimal timing and energy. To demonstrate that possibility, a simple design was attempted, where four TDCs were used for the four expected ToT channels received from the CDM of the PMT-based front-end.

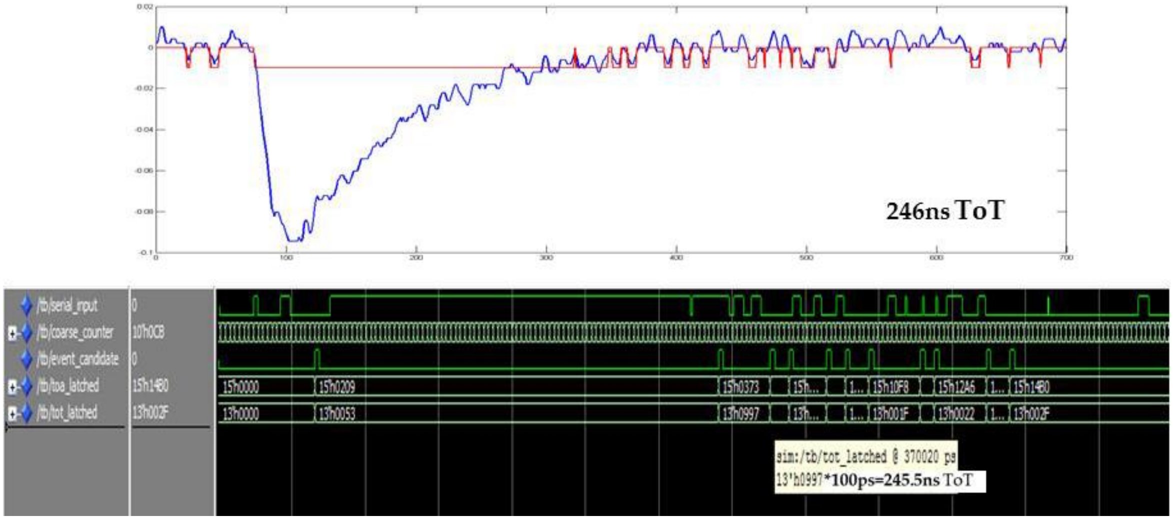

Figure 8. 8 (Top) an analog pulse and the generated ToT; and (bottom) firmware analysis and retrieval of ToT and ToA

The four inputs are sending an event candidate when a pulse of proper duration has been received, and an event trigger is created from the coincidence of these four candidates. In case no such condition is met within the 409.6ns window, the event is discarded (figure 8.9). From this condition the bit length of ToT words can be calculated, as 409.6ns correspond to a 13-bit digital word, with a least-significant bit (LSB) of 100ps.

In the case of MVT ToT, more TDCs for signals of different voltage thresholds will be implemented and a more complex triggering scheme will be designed and fine-tuned, drawing from offline analysis. A LuT can be implemented based on experimental data, to match known event times to NCMVT rising edge points.

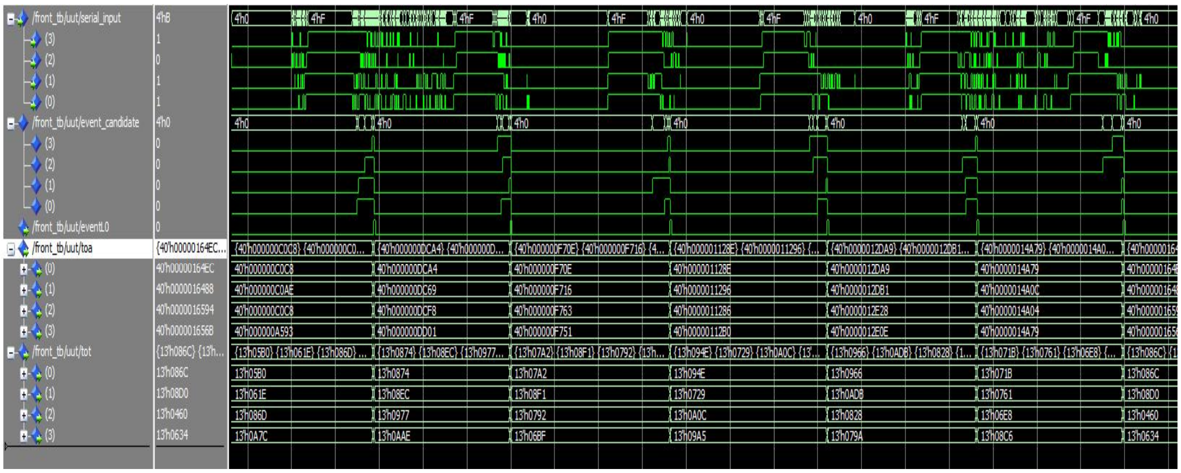

Figure 8. 9 Demonstration of candidate matching for events from the repository based testbench of ToT pulses

B. TDC laboratory experiment

Three different primitives were tried, corresponding to particular bulding blocks of the aforementioned slices: a two-bit LuT, single bit LuT and a buffer. The order at which the delay elements were placed was also verified and two different incrementations where attempted for the buffer case (figure 8.10).

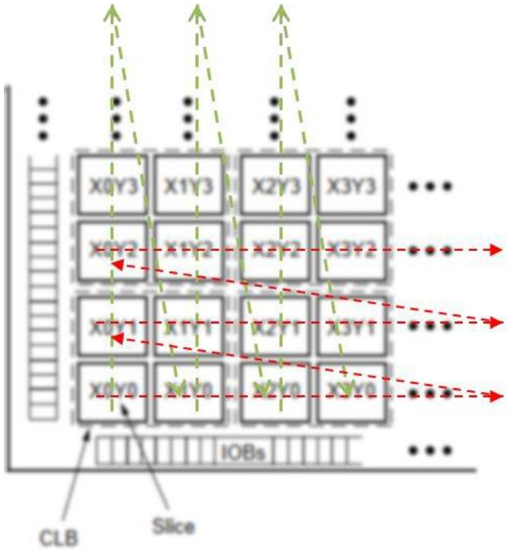

Figure 8. 10 Two (red and green) alternative sequences of delay elements for tapped delay line TDC on FPGA

As can be seen in figure 8.11 and table 8.1, no particular case is clearly advantageous towards the rest. Linearity of measurement is satisfactory, however TDC resolution is far from the literature standard, around 0.5 ns. The reason for this discrepancy comes from the fact that in our test firmware, clocked buffers of the outputs of the delay line were placed together, instead of being placed as close as possible to each delay element. In principle, the results acquired correspond to a statistic signal delay between slices in an area of the FPGA and a buffer vector in another area, something that can be understood by the significant discrepancy on average delay due to address incrementation sequence. Nevertheless, understanding of this problem led to deep understanding of details of the FPGA hardware architecture, necessary for next attempts.

Table 8.1 Results of delay for different primitives of a Spartan-3 FPGA

Primitive	Mean delay
LUT1	0.550 ns
LUT2	0.545 ns
BUFG vertical incrementation	0.772 ns
BUFG standard incrementation	0.584 ns

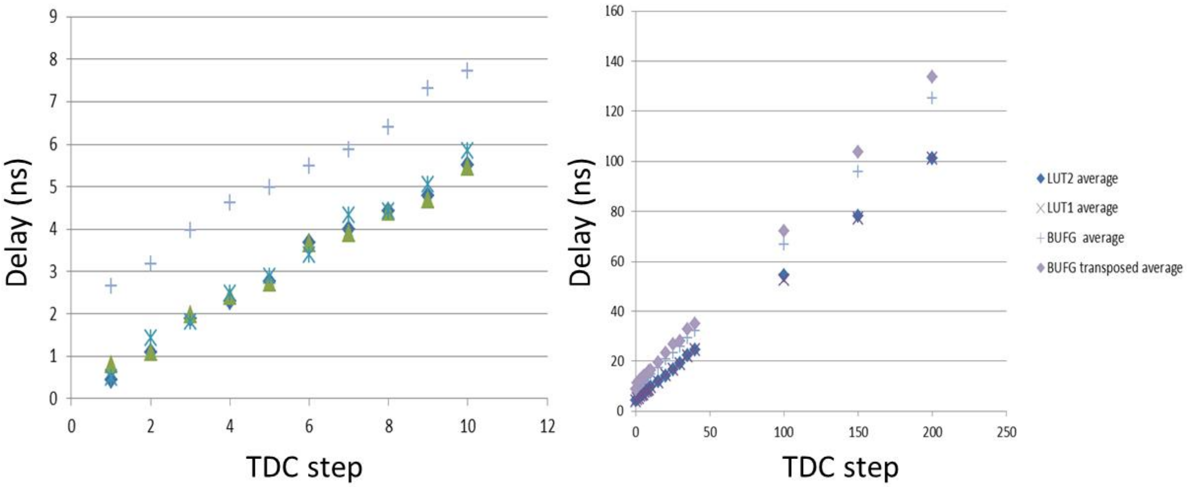

Figure 8. 11 Results of measurement of relative and absolute delay of different primitives –single-bit buffer (BUFG), two-bit buffer (BUFG2), single-bit look-up table for two placement processions (LUT1 and LUT2)– for a Spartan-3 FPGA

C. Position calculation algorithm

For the calculation of event position it was necessary to conduct an offline study, not only with the purpose of creating the aforementioned corresponding LuT, but also to estimate the truncation possibility such scheme has. Individual channels correspond to 13 bits each, as much as the subtraction of two; the addition would have 14 bits; the resulting division resolution corresponds to the dividend, thus the result should also have 13 bits. This theoretical approach doesn't apply to a design of integer values, as has been this one, while furthermore such resolution doesn't correspond to the precision of measurement. In this context, fewer bits at the output will be used and are chosen by the known space and precision limitations of the detector. For a 16x16 pixel scenario, 10 bits correspond to an average of 64x64 position values for each pixel, enough for detailed characterization of the FFD.

Initially, the possibility of using directly the X_1 and X_2 as inputs of the LuT was assesed. However, error propagation function for equation 8.1 demonstrates a smaller error if the addition is performed using full vectors. On the other hand, it can be deduced that the relation from the equation 8.2 is injective, thus the subtraction element is not necessary:

$$X = \frac{X_1 - X_2}{X_1 + X_2} \Rightarrow X_{estimator} = \frac{X_1}{X_1 + X_2} \qquad \text{(eq. 2)}$$

Knowing the characteristics and nature of these numbers allows constructing a smaller input space, by applying numeric limitations. Firstly, as demonstrated in figure 8.11, there is complete symmetry, in the case that instead of X_1, the bigger among X_1 and X_2 (X_{max}) is used; this choice is better than using the smaller, being the one having more significant bits, thus providing better precision after truncation.

By such application, only half of the position space needs to be covered by the LUT, lowering twofold the FPGA space required. Using the bigger number also adds the condition $X_1 + X_2 = X_{sum} > X_{max} \geq {X_{sum}}/{2}$, further lowering the material necessary for the LUT.

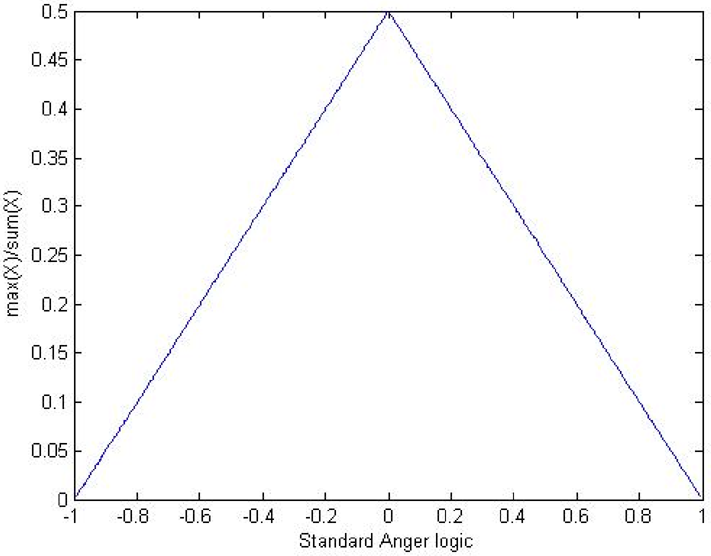

Figure 8. 12 Demonstration of the symmetry observed if only max or min is used for CDM logic

After limiting the LuT input space a study on the behavior of variable truncation lengths for X_{max} and $X_{sum}=X_1+X_2$ was performed. Results are shown in figure 8.12. Using 7 and 8 bits respectively was considered optimal, as a tradeoff between precision and material usage. The output was chosen to be 10 bits long, 9 of which provided by the LUT and the most significant one by the symmetry demonstrated in figure 8.11.

In this manner, the total of 26 bits in full resolution scenario, that would be applied in a straightforward approach and require a LUT of $2^{26}x2^{10}$ single bit memory elements were lowered to 15 bits by truncation, requiring $2^{15}x2^{10}$ elements. Furthermore, with the conditions and folding applied, plus the minimum duration of pulses due to thresholding, the developed LUT uses 39800 elements, demonstrating a compression factor close to 0.00006.

The algorithm described was implemented in firmware through a state machine, to make sure that the same LuT and adder are used for the calculation of both X and Y, with the delay of one clock cycle.

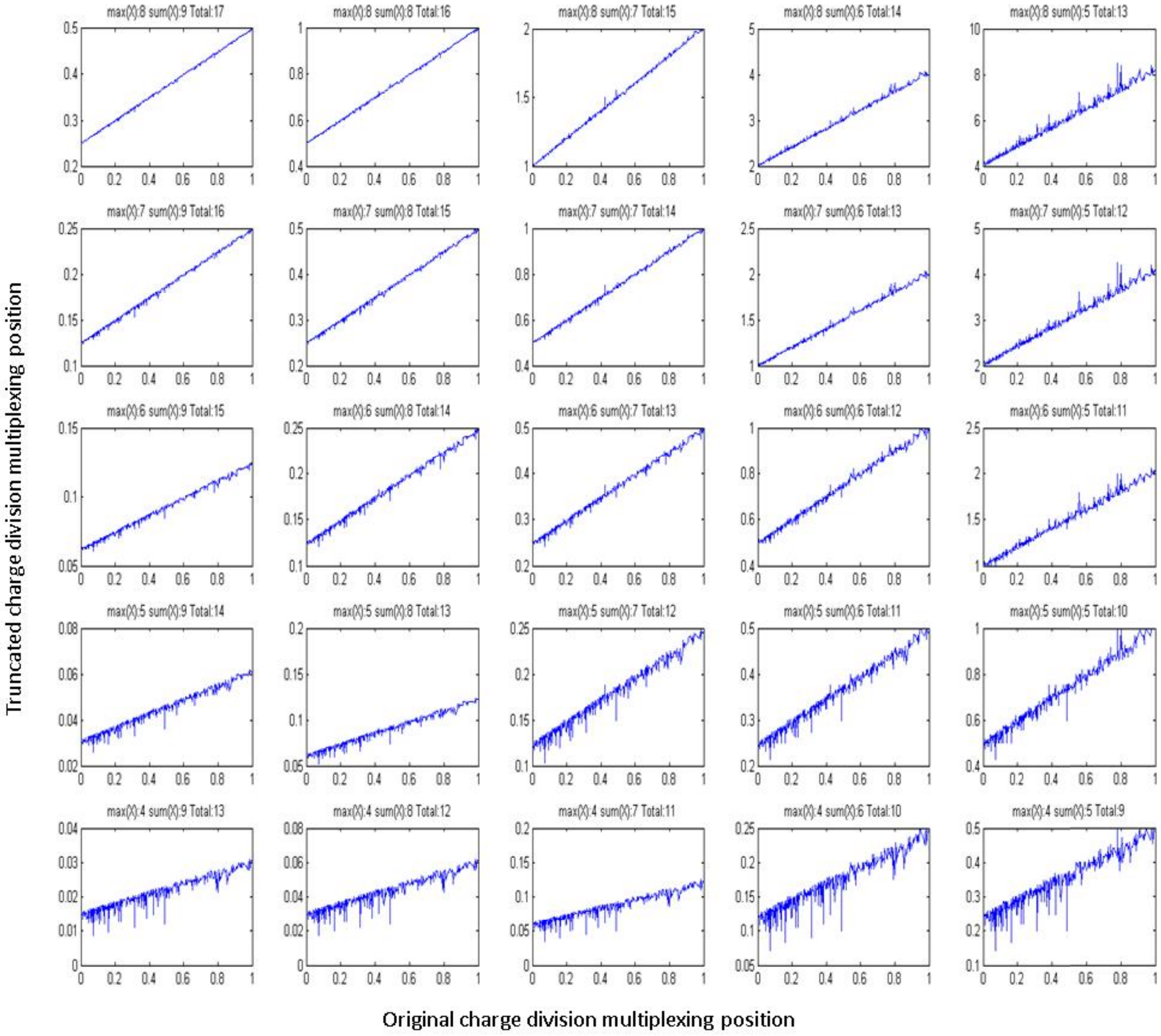

Figure 8. 13 Truncation and quality of signal study for different cases of trunc(X_{max})/trunc(X_1+X_2).

Such treatment has good possibilities to be better placed and fitted in hardware than general purpose dividers provided by the vendors. Moreover, this LUT can be directly connected with a higher-level LuT concerning direct characterisation of the location of an event to respective pixel and depth-of-interaction level. In this manner, once an event has been discriminated for belonging to the appropriate energy window, its position will be directly attributed. A set acquisition to create an FFD and pixel map offline is necessary, while implementing such a functionality in firmware is complicated and unecessary, as this calibration should not happen often but only when a new crystal is being placed on the photomultiplier.

D. Back-end communication

As it has been described in the previous paragraphs, the communication towards the backend will be duplex. Towards the front-end there are two types of control necessary; slow, referring to threshold setting and acquisition mode, and fast, referring to detector synchronization. These commands will be encoded at computer level using a syntax that will have a reference both in the VHDL as well as the computer environment (e.g., Python). They will be sent to a control module of the firmware architecture and decoded there, before being propagated to the rest of the FPGA design.

From the front-end there are also two types of data acquired; event data and statistics. The syntax of event data can be described in detail, now that the analysis of corresponding precision and trade-off choices have been made (table 8.2). The final length of word, multiplied by the maximum rate expected, calculated in previous chapters, gives the total digital data throughput rate per detector, and is calculated at an approximate maximum of 24.21 Mbps.

Table 8.2. Output data syntax

#	Quantity	bits
1	Acquisition type serving as Header	2
2	Coarse time: 0.859 seconds cycle, to allow next level timestamping	27
3	Fine time	5
4	Energy: 13 bits (409.6 ns max) for single channel, 15 bits for sum of four channels, can be truncated according to the known precision of measurement	10
5	Location: X:10 bits +Y:10 bits or case study: 5x5 cm^2/1.2x1.2 mm^2= 1764 pixels, 3528 if a stacked version of DoI is used. This corresponds to 12 bits	20 or 12
6	Detector ID: Case study for a small animal PET insert, less than 256 detectors are used	8
	Sum	**72 or 64**

Packets of data, sharing the same most-significant bits can be sent at a regular rate, to compress data throughput and facilitate back-end communication, without compromising data quality, taking into advantage the less time-critical nature of data acquisition at this stage. The actual back-end communication, however, will be implemented at a later stage and might include connection to a second, data management dedicated FPGA for designs with more detectors, instead of a computer.

IV. CONCLUSION

A conceptual design of the architecture developed can be seen in Appendix, along with conceptual designs for possible future architectures, either using NCMVT or more detector inputs served by the same FPGA. The developed VHDL codes can be found online.

This approach introduces some innovative elements, such as the implementation of ToT on Anger logic, which on the one hand allows minimizing the size, power consumption and complexity of the front-end, while facilitating the application of various multiplexing schemes. Such a front-end can be a ground-breaking design due to its foreseen superb MR compatibility, lacking digital and active components and using a floating ground and small, miniaturized electronics [4,5]. On the other hand, the data throughput is also minimum due to multiplexing and ToT conditioning. In this manner the FPGA design is also cost effective, while one low-end FPGA could host more than one detector readouts, further minimizing the cost.

During the study for the development of this firmware, several interesting aspects have emerged, such as the compressing effort for the location LUT, considerations for the synchronization of the design and discriminator threshold setting through calculation of noise switching activity. More testing, to evaluate an optimal solution for the front-end TDC primitive and add timing information, as well as adaptation logic to support the optimal scenario of NCMVT are foreseen.

Such aspects as the one developed create an intelligent, fast, interconnected and efficient front-end alternative for frontier exploitation in research and industry. Nevertheless, it is mainly expected to use this firmware as a tool guiding the development and prototyping of an OWC nuclear medicine detector. At a later stage it can be the backbone for a versatile front-end system on chip design including TDC and triggering intelligence on FPGA allowing scaling up to a fully functional, light-weight, miniaturized, cost-effective MR compatible PET/SPECT insert.

V. APPENDIX SYSTEM ARCHITECTURE CONCEPTS

A. Architecture developed

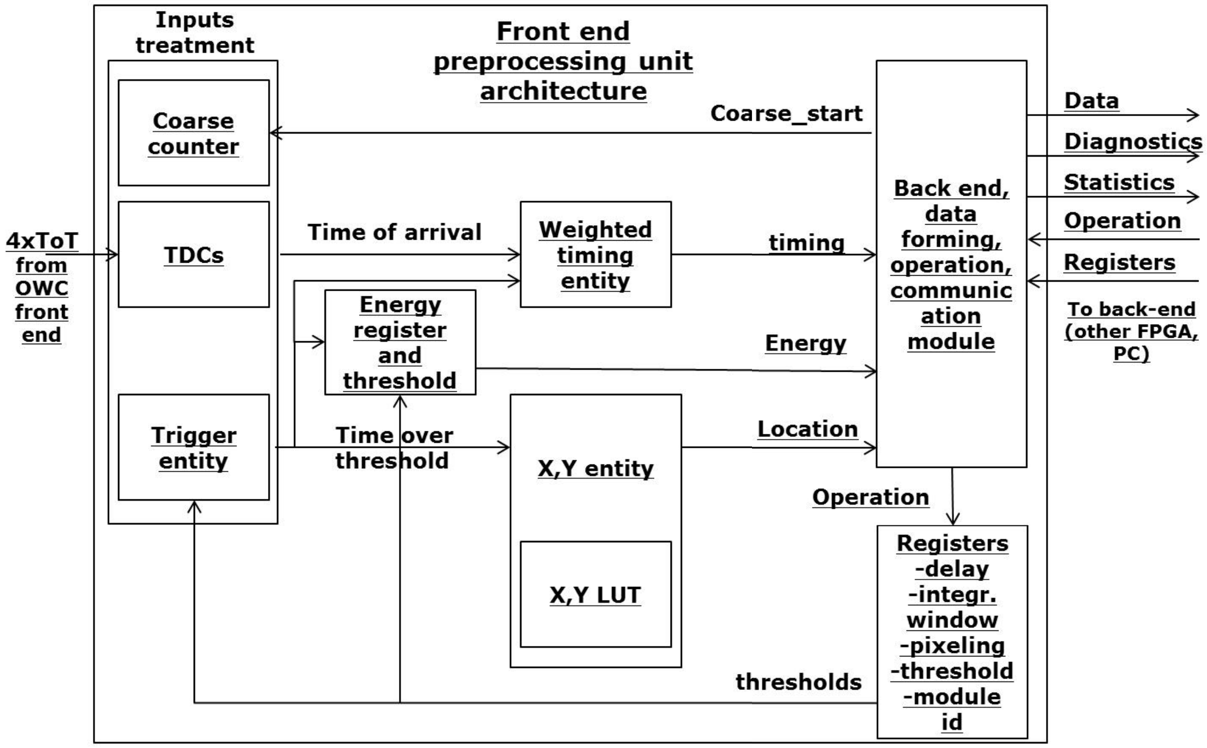

B. ToT MVT

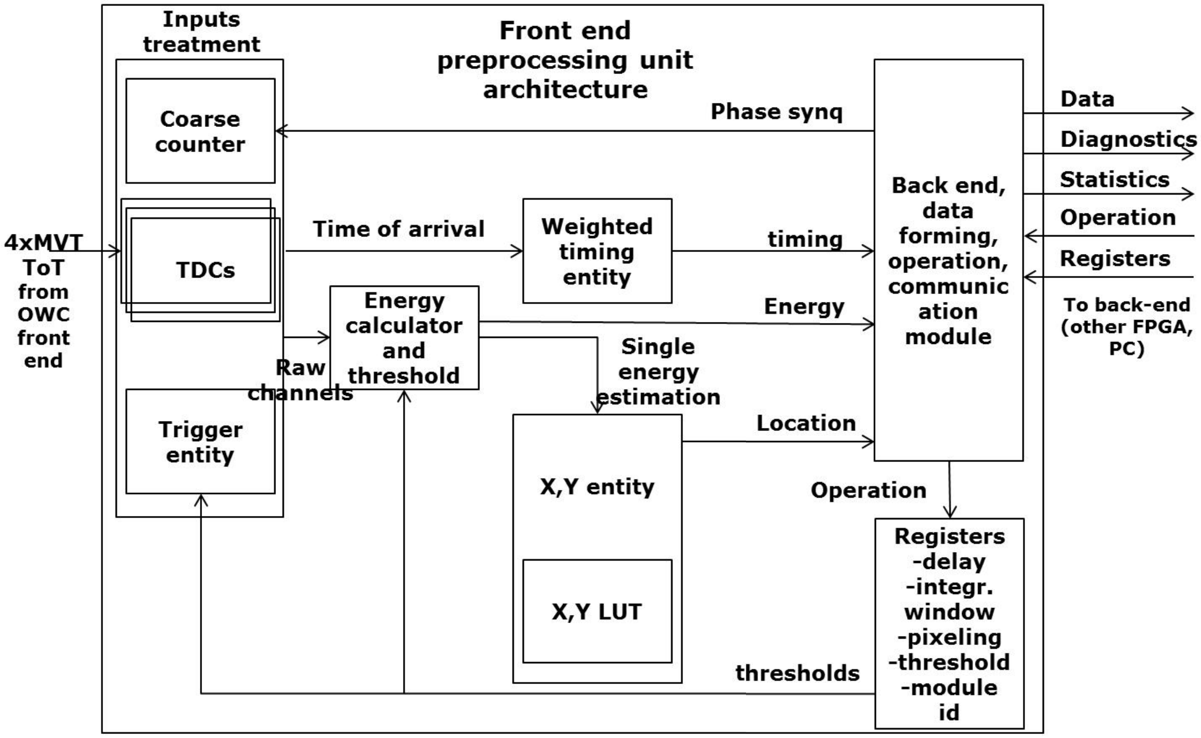

C. More detectors served by single FPGA

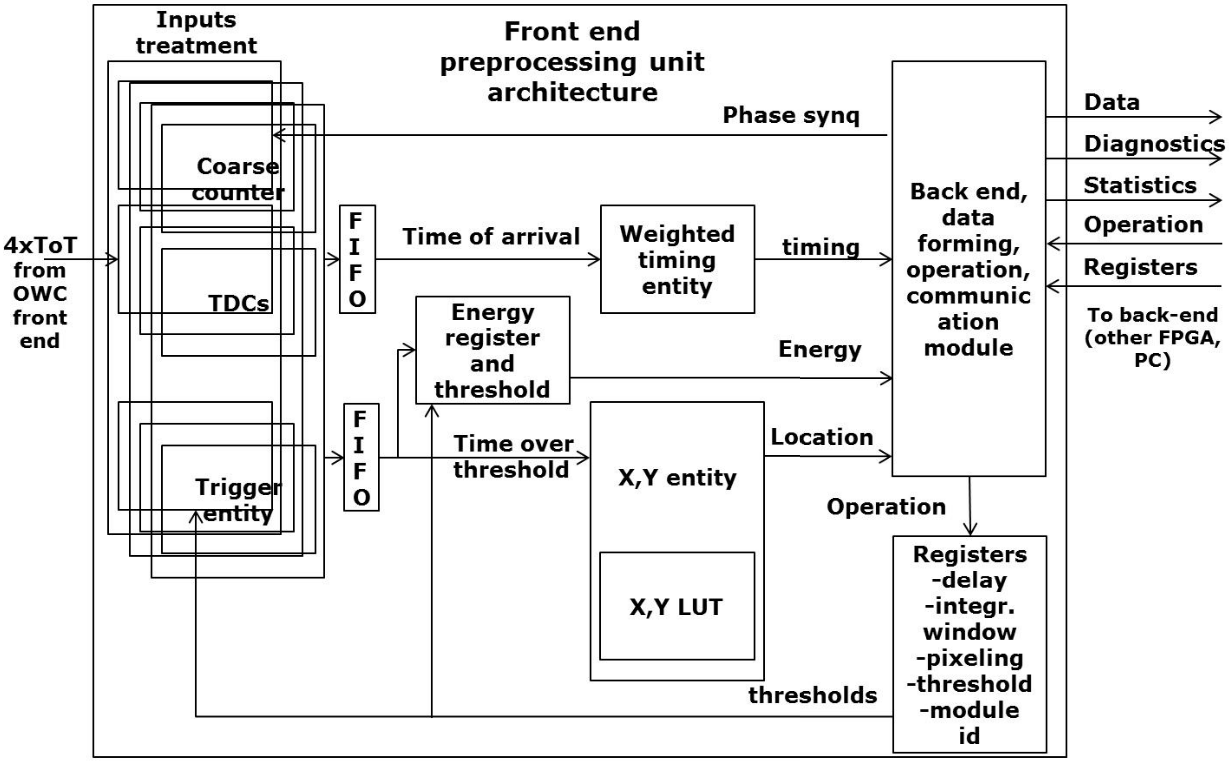

VI. REFERENCES

[1] España, S., Herraiz, J. L., Vicente, E., Herranz, E., Vaquero, J. J., Desco, M., & Udías, J. M. (2007, October). Improved image reconstruction in small animal PET using a priori estimates of single-pixel events. IEEE Nuclear Science Symposium Conference Record (Vol. 5, pp. 3876-3880). IEEE.

[2] Seidel, J., Vaquero, J. J., Siegel, S., Gandler, W. R., & Green, M. V. (1999). Depth identification accuracy of a three layer phoswich PET detector module. IEEE Transactions on Nuclear Science, 46(3), 485-490.

[3] Anghinolfi, F., Jarron, P., Martemiyanov, A. N., Usenko, E., Wenninger, H., Williams, M. C. S., & Zichichi, A. (2004). NINO: an ultra-fast and low-power front-end amplifier/discriminator ASIC designed for the multigap resistive plate chamber. Nuclear Instruments and Methods in Physics Research Section A: Accelerators, Spectrometers, Detectors and Associated Equipment, 533(1), 183-187.

[4] Olcott, P., Kim, E., Hong, K., Lee, B. J., Grant, A. M., Chang, C. M., ... & Levin, C. S. (2015). Prototype positron emission tomography insert with electro-optical signal transmission for simultaneous operation with MRI. *Physics in medicine and biology*, *60*(9), 3459.

[5] Weissler, B., Gebhardt, P., Lerche, C. W., Wehner, J., Solf, T., Goldschmidt, B., ... & Heberling, D. (2014). MR compatibility aspects of a silicon photomultiplier-based PET/RF insert with integrated digitisation. *Physics in medicine and biology*, *59*(17), 511

[6] Castilla, J., Cela, J. M., Comerma, A., Fernandez-Varea, J. M., Freixas, L., Garrido, L., ... & Rato-Mendes, P. (2013, October). Evaluation of the FlexToT ASIC on the readout of SiPM matrices and scintillators for PET. In Nuclear Science Symposium and Medical Imaging Conference (NSS/MIC), 2013 IEEE (pp. 1-4). IEEE.

[7] Fleury, J., Callier, S., de La Taille, C., Seguin, N., Thienpont, D., Dulucq, F., ... & Martin, G. (2014). Petiroc and Citiroc: front-end ASICs for SiPM read-out and ToF applications. Journal of Instrumentation, 9(01), C01049.

[8] Maxfield, C. (2011). FPGAs: instant access. Newnes.

[9] http://www.eetimes.com/document.asp?doc_id=1316816, retrieved 6.3.2017

[10] https://www.microsemi.com/products/fpga-soc/fpga/igloo-nano, retrieved 6.3.2017

[11] Ashenden, P. J. (2010). The designer's guide to VHDL (Vol. 3). Morgan Kaufmann.

[12] Smith, D. J., & Foreword By-Zamfirescu, A. (1998). HDL Chip Design: A practical guide for designing, synthesizing and simulating ASICs and FPGAs using VHDL or Verilog. Doone Publications.

[13] Opler, Ascher (January 1967). "Fourth-Generation Software". Datamation. 13 (1): 22–24.

[14] Bhasker, J. (2002). A SystemCTM Primer (Vol. 125, p. 126). Star Galaxy Publishing.

[15] http://www.embeddedintel.com/commentary.php?article=2143, retrieved 6.3.2017

[16] Crockett, L. H., Elliot, R. A., Enderwitz, M. A., & Stewart, R. W. (2014). The Zynq Book: Embedded Processing with the Arm Cortex-A9 on the Xilinx Zynq-7000 All Programmable Soc. Strathclyde Academic Media.

[17] Homulle, H., Regazzoni, F., & Charbon, E. (2015, February). 200 MS/s ADC implemented in a FPGA employing TDCs. In Proceedings of the 2015 ACM/SIGDA International Symposium on Field-Programmable Gate Arrays (pp. 228-235). ACM.

[18] Kalisz, J. (2003). Review of methods for time interval measurements with picosecond resolution. Metrologia, 41(1), 17.

[19] MicroBlaze Processor Reference Guide. by: Xilinx. No. 4.0. (2004) Key: citeulike:2582847

[20] Moskal, P., Bednarski, T., Białas, P., Czerwiński, E., Kapłon, Ł., Kochanowski, A., ... & Krzemień, W. (2014). A novel method based solely on field programmable gate array (FPGA) units enabling measurement of time and charge of analog signals in positron emission tomography (PET). Bio-Algorithms and Med-Systems, 10(1), 41-45.

[21] Fishburn, M., Menninga, L. H., Favi, C., & Charbon, E. (2013). A 19.6 ps, FPGA-based TDC with multiple channels for open source applications. IEEE Transactions on Nuclear Science, 60(3), 2203-2208.

[22] Laboratory of Medical Physics, Master degree in Physics, Dept. of Physics "E. Fermi", University of Pisa, 2016.

[23] Szplet, R., Kalisz, J., & Jachna, Z. (2009). A 45 ps time digitizer with a two-phase clock and dual-edge two-stage interpolation in a field programmable gate array device. Measurement Science and Technology, 20(2), 025108.

[24] Xilinx 7 Series FPGAs CLB User guide, https://www.xilinx.com/support/documentation/user_guides/ug474_7Series_CLB.pdf, retrieved 8.3.2017

[25] Vaquero, J. J., Seidel, J., Siegel, S., Gandler, W. R., & Green, M. V. (1998). Performance characteristics of a compact position-sensitive LSO detector module. *IEEE transactions on medical imaging*, *17*(6), 967-978.

[26] Lichard, P., Konstantinou, G., Vilanueva, A. V., & Palladino, V. (2014). Performance evaluation of multiple (32 channels) sub-nanosecond TDC implemented in low-cost FPGA. Journal of Instrumentation, 9(03), C03013.

[27] Jurgensen, N., Arpin, L., Bouziri, H., Njejimana, L., Koua, K., Gaudin, E., ... & Fontaine, R. (2015, October). Initial results for automatic calibration of the LabPET II front-end detector module. In Nuclear Science Symposium and Medical Imaging Conference (NSS/MIC), 2015 IEEE (pp. 1-3). IEEE.

Chapter 9: Discussion and Conclusions

A. Discussion

Reaching the end of this manuscript, it is deemed necessary to provide a disclaimer. It is considered, sometimes, that the work of a researcher is either referring to fundamental science, or to the development of applicable solutions. The first case is when the big questions of humankind are being debated; theories corresponding to the nature of science are put under scrutiny and novel approaches are proposed. On the other hand, it is a common misconception that when research is not fundamental, it should serve towards creation of applications or appliances that are ready to be used in industry and create disruptive economic or scientific results.

The place of research on applied science doesn’t fall within the limits of neither of the aforementioned categories, corresponding more precisely to the empty space between them and with the intention of bridging them. It is applied science, whether on high energy physics, astronomy and astrophysics, medical and life sciences that can shape the fundamental novelties of the one side to the applicable ones of the other. This is a not obvious, but very important realization that liberates this field from the responsibility it very often is cumbered with.

The place of a doctorate dissertation, furthermore, within the narrow framework that modern scientific development allows, timewise and resource-wise, is even direr. One can freely revere the groundbreaking breakthroughs and smooth formalization found in some of the theses of the supreme scientists of the previous century, as for instance Dirac [1] and Higgs [2]. However, the scientific space allowed in today’s doctorates, when research funding is often based on them is gradually smaller, while the growing multitude of candidates suppresses it further. In this context, the fact that the number of doctoral hopefuls at the moment has swollen to such extent that there are currently almost one million doctorate candidates only in European Union [3] doesn’t mean that an equally amplified amount of scientific breakthroughs are to be foreseen; it merely corresponds to the post-capitalistic form work environments take, where highly trained and specialized individuals provide the insight, while the machine provides the muscle; this novel situation has yet to demonstrate its social effects, apart from within the narrow point of view of the forming caste of doctors-to-be. Under the spotlight of this context and back in the environment of the scientific concourse, the question of the hypothesis is brought back to the front stage to be evaluated.

PET/MR, even though fundamentally beneficial as a revolutionary tool of multimodal imaging with broad applications in experimental and clinical scenarios, has yet to gain the momentum expected. Our approach intends to contribute finding an answer to this antinomy based on detailed study of the prior knowledge and insight the related scientists, researchers and industrialists provide (table 1.1). In this context we accept the MR compatible PET insert as the vessel within which our efforts will be developed. And with this in mind, we propose a set of answers to the open related objectives that were presented in table 1.2.

B. Contributions

Through the course of this process, we first intended to follow-up on the research performed [4] over the last decade, on sub-surface laser engraving (SSLE) for scintillator crystals. We have established the limitations and tradeoffs related with the quality and resolution of the SSLE setting, demonstrating that these limitations, for instance on light isolation, can be contained by careful design and be beneficial for controlled light-sharing. In the same study, we demonstrated that partial light sharing can be resolved by the deterministic character the vast statistics of big numbers of photons provide and corrected for reconstruction purposes.

Furthermore, it was possible to show that SSLE technique, until now only attempted on LYSO, is also possible for GSO but not openly available for any type of scintillator. With more information on knowledge from laser manufacturing research, we provided metrics on how the settings of a SSLE system can be adapted in order to replicate the process using different raw material. In the light of novel scintillators, such as GAGG and LuAG, being increasingly made available, we believe that this knowledge can be useful for future researchers.

By getting experience with the SSLE setting, we were able to provide, for the first time, pixels on scintillators of not traditional rectangular prism form. Some advantages of this novelty have been calculated, as for instance the optimal bidimensional packaging of hexagonal prisms that improves pixel resolvability by as much as 8%. Another undisputable advantage is the supreme packing ratio, which was measured through experimental processes and quantified through analysis of the results and simulation. Other, as for instance the foreseen optimization of light guiding that could assist the timing characterization of scintillating events, remain to be proven.

Furthermore, a broad study on depth-of-interaction (DoI) designs was conducted. This study not only demonstrates the viability of SSLE design within most of the available DoI techniques, but also paves the way for their expansion into novel ones. The mathematic approach constructed is intended to form the backbone of automatic characterization routines. All of the aforementioned SSLE breakthroughs can find application in design of novel PET inserts; however, particularly the ease with which DoI patterns can be constructed, along with the higher sensitivity available through SSLE, can liberate the geometry of inserts; a claim that was explored through the geometrical study of two possible candidates: a small animal PET insert and a dedicated brain PET insert.

Drawing away from the laser manufacturing space, we focused on data transmission, compression and preprocessing. This has been a broadly interdisciplinary effort, requiring collaborations with optical communication and firmware engineers, broadening the detector development process in a second multidisciplinary dimension. First, we attempted to quantify a standing question, whether signals from analog charge-division multiplexing (CDM) designs can be further compressed through the non-linear conversion to time-over-threshold (ToT) discrimination.

Through careful study of how this approach can materialize, as for instance by the application of ASICs, we applied the limitations and intended to provide a viable alternative to existing multi-voltage-threshold (MVT) ToT. This was done through developing a noise statistical correction technique. Measured spatial resolution deterioration falls within limits, responding positively to the debatable hypothesis of extreme data compression through both CDM and noise-corrected (NC) MVT ToT, with the application of only two discriminators per channel. Timing resolution can be improved through the application of fitting techniques; however, such application can be made redundant through usage of novel silicon.

By the extreme compressing, it has been made possible to study and construct an optically connected prototype detector. This was not only made possible for optical fiber designs, but furthermore for the first time in literature through the application of analog optical wireless communication (aOWC) techniques. Raw compressed data can be transmitted with sufficient fidelity through open space to a receiving back-end, providing a novel answer to the stand-off of requiring the placement of digital electronics inside the magnetic field of an MRI.

Finally, we demonstrate the viability of development of a system-on-chip (SoC) on low cost FPGA that can receive the formed NCMVT ToT scintillation pulses and measure the duration through the application of time-to-digital converters (TDC) on board. Studies for fast and low-material-use transformation of the TDC vectors to pulse energy content and position estimators were made and simulated on the same hardware design. Furthermore, debugging, data management and back-end communication aspects were addressed, forming the backbone of a fast and intelligent pre-processing system.

The design goals were also evaluated against SPECT insert considerations and specifications. In principle, the bulk of the breakthroughs described in the previous paragraphs apply and can also potentially benefit the design of novel MR compatible SPECT inserts. This, however, remained a theoretical study and will not be considered as belonging to the scope of this thesis. In table 9.1, published results of the aforementioned studies are outlined.

Table 9.1 Published results

Result	Title
Peer reviewed publication	**"Sub-surface laser engraving techniques for scintillator crystals: methods, applications and advantages"**, G. Konstantinou et al., IEEE Transactions on Radiation and Plasma Medical Sciences, 2017, In review
Peer reviewed publication	**"Noise corrected double voltage time-over-threshold method and FPGA read-out design for PET applications"**, G. Konstantinou et al., IEEE Transactions on Radiation and Plasma Medical Sciences, 2017, In preparation
Patent	**"Sistema de detección de radiación gamma y sistema de resonancia magnética"**, G. Konstantinou, J. J. Vaquero López, R. Chil Pérez, W. Ali, G. Cossu, E. Ciaramella, ES, P201631388, 28/10/2016
Patent	**"Celda centelleadora"**, G. Konstantinou, J.J. Vaquero López, R. Chil Pérez, M. Desco, ES P201631258, 28/09/2016
Conference presentation	**"Applications of Sub-Surface Laser Engraving on Monolithic Scintillator Crystals: Novel Pixel Geometries and Depth of Interaction"**, G. Konstantinou et al., IEEE NSS/MIC, 2016
Conference presentation	**"Experimental demonstration of an optical wireless MRI compatible PET/SPECT insert front-end"**, G. Konstantinou et al., IEEE NSS/MIC, 2016
Conference presentation	**"Simulation, development and testing of a PET detector prototype using monolithic scintillator crystals treated with the sub-surface engraving technique"**, G. Konstantinou et al., 2015 IEEE Nuclear Science Symposium and Medical Imaging Conference (NSS/MIC), 2015, DOI: 10.1109/NSSMIC.2015.7581826, 1st student poster award
Conference presentation	**"Simulations, testing and results for the pixelation of LYSO crystals for gamma detectors using SSLE techniques"**, G. Konstantinou et al., Conference: 2014 IEEE Nuclear Science Symposium and Medical Imaging Conference (NSS/MIC), 2014, DOI: 10.1109/NSSMIC.2014.7430866

C. Thesis

By the application of transdisciplinary knowledge, I have developed novel techniques that expand the MR compatible PET insert design. SSLE for scintillation crystals liberates novel detector design while enhancing its characteristics, while aOWC and smart processing detach and miniaturize it greatly. With this range of breakthroughs, I esteem that it will be possible to address the barriers to clinical adoption of PET/MR, facilitating and thus contributing to fundamental and applied scientific research, adding another brick of knowledge and experience to enrich the marvelous wonder of human intellect.

REFERENCES

[1] Dirac, P.A.M.(1926). Quantum mechanics (Doctoral dissertation, Trinity college, Cambridge university)

[2] Higgs, P. W. (1954). Some problems in the theory of molecular vibrations (Doctoral dissertation, King's College London, University of London).

[3] Eurostat, statistics explained, R&D personnel, http://ec.europa.eu/eurostat/statistics-explained/index.php/R_%26_D_personnel, retrieved 13/3/2017

[4] Moriya, T., Fukumitsu, K., Sakai, T., Ohsuka, S., Okamoto, T., Takahashi, H., ... & Yamashita, T. (2010). Development of PET detectors using monolithic scintillation crystals processed with sub-surface laser engraving technique. *IEEE Transactions on Nuclear Science*, *57*(5), 2455-2459.